

A Comprehensive Study on Top Quark FCNC Interactions in SMEFT Framework

Subhajit Kala^a Soumitra Nandi^a

Department of Physics, Indian Institute of Technology Guwahati, North Guwahati, Assam-781039, India.

E-mail: s.kala@iitg.ac.in, soumitra.nandi@iitg.ac.in

ABSTRACT: We present a comprehensive, model-independent analysis of rare flavour-changing neutral current (FCNC) interactions of the top quark within an effective field theory framework. Beginning with a general parametrisation of top-FCNC couplings, we match these interactions onto the Standard Model Effective Field Theory (SMEFT) operator basis at the top-quark scale. We then perform a global study that incorporates constraints from low-energy flavour observables, electroweak precision data, Higgs and gauge-boson measurements, and electric dipole moment (EDM) bounds. By treating the dipole operators as complex, we derive stringent limits on both the real and imaginary components of left- and right-handed FCNC couplings. In particular, we show that constraints from the neutron EDM impose especially strong bounds on products of FCNC couplings involving the transition $t \rightarrow u$. Translating these results into the SMEFT framework, we obtain robust constraints on several products of the corresponding SMEFT Wilson coefficients. Finally, we provide predictions for branching ratios and CP asymmetries in rare top-quark FCNC decays. We identify well-motivated benchmark scenarios for future collider searches and emphasise the crucial role of CP-violating effects in probing the flavour structure of the top quark.

KEYWORDS: Rare top-FCNC, Standard Model Effective Field Theory

Contents

1	Introduction	2
2	Effective Framework	3
3	Methodology	8
4	Impact on various observables	11
4.1	Low Energy Observables	11
4.1.1	Observables related to FCNC Processes	11
4.1.2	Observables related to FCCC Processes	18
4.2	Electroweak Precision Observables	21
4.3	Other relevant Observables	26
4.3.1	Observables related to Higgs Physics	26
4.3.2	Trilinear Gauge Couplings	29
4.3.3	Top Chromo-magnetic dipole moment	30
5	Analysis and Results	31
5.1	Constraints from collider searches	32
5.2	Constraints on top-FCNC Effective couplings from the combined analyses	33
5.2.1	SMEFT Correspondence	37
5.3	Predictions for branching ratios	41
5.4	Predictions of a few CP asymmetries	44
5.5	Electric dipole moment of light quark	47
6	Summary	53
A	RGEs: beta functions	55
B	Loop Contributions	56
C	EDM and CEDM Contributions	61
D	Correlation Matrices	63
E	SMEFT Couplings	64

1 Introduction

The top quark, the heaviest particle in the Standard Model (SM), plays a crucial role in probing the dynamics of electroweak symmetry breaking and potential physics beyond the SM. Its large mass, close to the electroweak scale, suggests that the top quark may serve as a sensitive probe of new physics interactions. The top quark, being a cornerstone of particle physics, has decay and production modes that have been extensively studied at the Large Hadron Collider (LHC). Despite extensive studies, many of its characteristic properties remain unexplored, particularly in FCNC processes, such as $t \rightarrow c(u)$ decays. In the SM, such processes are forbidden at tree level and highly suppressed at higher orders due to the Glashow–Iliopoulos–Maiani (GIM) mechanism, leading to branching fractions of the order of $10^{-12} - 10^{-14}$ [1] for top decays such as $t \rightarrow u_j X$ with $X \in \{g, \gamma, Z, H\}$ and $u_j = u, c$, several orders of magnitude below the current experimental limits [2]. Consequently, any observable signal of top FCNC interactions at present or future colliders would provide an unambiguous indication of new physics. If the new physics (NP) lies at an energy too heavy to be directly produced on-shell, its effects can still manifest indirectly through virtual contributions. These imprints can be systematically captured within the effective field theory (EFT) framework. In this context, top decay processes have been extensively studied within EFT approaches [3–12], and further explored in recent work on top-quark flavour dynamics [13–15]. In addition, several ultraviolet (UV) complete models, such as two-Higgs-doublet models (2HDMs), supersymmetric scenarios, the Alternative Left Right model, and frameworks with vector-like quarks or extended gauge sectors, predict significant enhancements of these top-FCNC decays [16–22]. Simplified models [23–27] have also been constructed to parametrise such effects in a model-independent fashion, potentially bringing their branching ratios within experimental reach.

From an experimental perspective, searches for rare top decays and anomalous single-top production and top pair production modes have been carried out extensively at the LHC by the ATLAS [28–31] and CMS [32, 33] collaborations, placing stringent bounds on a wide range of top FCNC channels. These searches are expected to improve significantly with the increased luminosity of the High-Luminosity LHC (HL-LHC), thereby providing even better sensitivity to rare top-quark interactions.

This work aims to investigate how various observables, such as low-energy flavour-changing charged-current (FCCC) and FCNC processes, electroweak precision observables (EWPOs), and other relevant high-energy measurements, individually and collectively constrain the effective couplings associated with rare top-quark decays, $t \rightarrow c(u) X$. Furthermore, we derive constraints on the corresponding dimension-six operators within the SMEFT, which contribute to the effective operators for $t \rightarrow c(u) X$ through tree-level matching conditions. We perform a global study incorporating a wide range of observables sensitive to these couplings at different energy scales. To determine the dependence of these observables on the SMEFT Wilson coefficients (WCs) or top-quark FCNC couplings, we evolve the WCs from the new-physics scale Λ_{NP} down to the relevant low-energy scales for each observable. This evolution is carried out using renormalisation group equations (RGEs) within the SMEFT framework. At the electroweak scale, we perform one-loop

matching between SMEFT and the low-energy effective field theory (LEFT). Subsequently, the WCs are evolved further within LEFT to the scales relevant for low-energy processes. Finally, we construct a global likelihood function incorporating all observables and perform a statistical fit to constrain the SMEFT WCs.

Previous studies have primarily focused on placing indirect constraints on the couplings of four-fermion SMEFT operators relevant to $(t \rightarrow c\ell\ell)$ transitions [3, 13, 14, 34], with some analyses incorporating bounds from low-energy FCNC processes $b \rightarrow s\ell^+\ell^-$ decays [13, 14]. In contrast, our work focuses on a distinct class of SMEFT operators which contribute to $t \rightarrow u_j, X$ interactions (where $u_j = u, c$ and $X = g, \gamma, Z, H$) after tree-level matching, and systematically investigates a substantially broader set of observables spanning multiple energy scales. We estimate the contributions of these operators to all relevant observables in the sectors mentioned above and perform both independent and global analyses. By leveraging a diverse array of observables, our goal is to establish significantly more robust constraints on the corresponding WCs. To the best of our knowledge, a comprehensive approach employing this specific set of operators is absent from the existing literature. From a technical perspective, the SMEFT operators relevant to our study may mix with the SMEFT four-fermion operators associated with $t \rightarrow c\ell\ell$ transitions during the running of their WCs. However, these effects are negligibly small. We will discuss this later in the appropriate section. Moreover, we explicitly account for the complex nature of SMEFT WCs, which is essential for uncovering the proper structure and CP properties of potential new physics. This comprehensive and multi-faceted analysis represents a decisive step forward in constraining SMEFT operators in the top-quark sector. This expanded framework not only enhances sensitivity but also provides a more complete picture of the underlying NP parameter space.

The paper is organised as follows. In section 2, we introduce the effective couplings for top-FCNC interactions and their corresponding SMEFT WCs. In section 4, we outline the methodology adopted for our analysis. Section 4 provides a detailed list of all the observables considered, classified into subsections: subsection 4.1 covers low-energy flavour observables; subsection 4.2 presents different EWPOs; subsection 4.3 summarises other relevant high-energy observables sensitive to top effective couplings. In section 5, we present our results, highlighting the different fitting scenarios and discussing the impact of incorporating direct collider bounds into the analysis. Finally, in section 6, we summarise our findings.

2 Effective Framework

In the absence of direct evidence for new particles at current collider energies, an effective field theory (EFT) approach provides a robust and model-independent framework to study potential new physics effects. Our analysis is based on an effective Lagrangian that systematically captures possible new physics (NP) contributions to top FCNC vertices, like $t \rightarrow u_j g$, $t \rightarrow u_j \gamma$, $t \rightarrow u_j Z$, and $t \rightarrow u_j H$, where $u_j = u, c$. The most general effective

Lagrangian encompassing all these processes can be written as:

$$\begin{aligned}
-\mathcal{L}_{\text{eff}} = & \sum_{u_j=u,c} \bar{u}_j \left[\frac{g_s}{2m_t} T^A \sigma^{\mu\nu} \left(\xi_L^{u_j t} P_L + \xi_R^{u_j t} P_R \right) G_{\mu\nu}^A + \frac{e}{2m_t} \sigma^{\mu\nu} \left(\lambda_L^{u_j t} P_L + \lambda_R^{u_j t} P_R \right) F_{\mu\nu} \right. \\
& + \frac{g_W}{2c_W m_t} \sigma^{\mu\nu} \left(\kappa_L^{u_j t} P_L + \kappa_R^{u_j t} P_R \right) Z_{\mu\nu} - \frac{g_W}{2c_W} \gamma^\mu \left(X_L^{u_j t} P_L + X_R^{u_j t} P_R \right) Z_\mu \quad (2.1) \\
& \left. - \frac{1}{\sqrt{2}} \left(\eta_L^{u_j t} P_L + \eta_R^{u_j t} P_R \right) H \right] t + \text{H.C.}
\end{aligned}$$

Here $\sigma^{\mu\nu} = \frac{i}{2} [\gamma^\mu, \gamma^\nu]$, and $G_{\mu\nu}$, $F_{\mu\nu}$, and $Z_{\mu\nu}$ denote the field strength tensors of the gluon, photon, and Z boson, respectively and $P_{L(R)} = (1 \mp \gamma^5)/2$ corresponds to the chirality projection operators. Since FCNC processes are forbidden at tree level in the SM, all the couplings in eq. (2.1) vanish at leading order. However, such couplings can be generated at the one-loop level within the SM, or they may arise at tree level or one-loop in various beyond-the-Standard-Model (BSM) scenarios [35, 36]. In this analysis, our objective is to constrain the strengths of the couplings associated with the operators introduced in the effective Lagrangian, considering a wide variety of observables to which these operators may contribute. Furthermore, we take this opportunity to place bounds on the WCs of the SMEFT operators that can induce these FCNC interactions through tree-level matching, thereby effectively capturing the flavour structure of potential new physics effects. In the following paragraph, we discuss the SMEFT correspondence of the top-FCNC operators defined in the above Lagrangian.

SMEFT Correspondence: The SMEFT framework is constructed by extending the SM Lagrangian with higher-dimensional operators ($d \geq 4$), built solely from SM fields and invariant under the full SM gauge symmetries. The general SMEFT Lagrangian takes the form:

$$\mathcal{L}_{\text{SMEFT}} = \mathcal{L}_{\text{SM}}^{(4)} + \sum_{d>4} \frac{\mathcal{C}_i^{(d)}}{\Lambda^{d-4}} \mathcal{O}_i^{(d)} \quad (2.2)$$

where $\mathcal{O}_i^{(d)}$ are the d -dimensional operators constructed from SM fields, and $\mathcal{C}_i^{(d)}$ are the corresponding dimensionless WCs. It is worth mentioning that for each i -th operator, there will be another summation over the generation indices p and r , so the dimension-six SMEFT Lagrangian can be rewritten as:

$$\mathcal{L}_{\text{SMEFT}}^{i(6)} = \sum_{p,r} \left(\frac{\mathcal{C}_{pr}^i}{\Lambda^2} \mathcal{O}_{pr}^i + \text{h.c.} \right) \quad (2.3)$$

We choose a few dimension-six top quark flavour-violating SMEFT operators in the representation of the Warsaw basis [37] to match the effective couplings in eq. (2.1) at tree level. We have listed these operators in table 1. In these operators, one of the up-type quarks is from the third generation (top quark), while the other is taken from the first or second generation only. We assume that NP arises solely from this subset of SMEFT operators, with all other operators set to zero. For the rest of our analysis, we redefine the

Top dipole		Top Higgs	
\mathcal{O}_{pr}^{uG}	$(\bar{q}_p \sigma^{\mu\nu} T^A u_r) \tilde{\phi} G_{\mu\nu}^A$	$\mathcal{O}_{pr}^{\phi q(1)}$	$(\phi^\dagger i \overleftrightarrow{D}_\mu \phi) (\bar{q}_p \gamma^\mu q_r)$
\mathcal{O}_{pr}^{uB}	$(\bar{q}_p \sigma^{\mu\nu} u_r) \tilde{\phi} B_{\mu\nu}$	$\mathcal{O}_{pr}^{\phi q(3)}$	$(\phi^\dagger i \overleftrightarrow{D}_\mu^I \phi) (\bar{q}_p \tau^I \gamma^\mu q_r)$
\mathcal{O}_{pr}^{uW}	$(\bar{q}_p \sigma^{\mu\nu} u_r) \tau^I \tilde{\phi} W_{\mu\nu}^I$	$\mathcal{O}_{pr}^{\phi u}$	$(\phi^\dagger i \overleftrightarrow{D}_\mu \phi) (\bar{u}_p \gamma^\mu u_r)$
		$\mathcal{O}_{pr}^{u\phi}$	$(\phi^\dagger \phi) (\bar{q}_p u_r \tilde{\phi})$

Table 1. List of dimension-six SMEFT operators that contribute to top quark FCNC interactions ($t \rightarrow u_j X$), where $X = g, \gamma, Z, H$, at tree level. Here, τ^I and T^A denote the generators of the $SU(2)_L$ and $SU(3)_C$ gauge groups, respectively. The indices p and r are generation indices; in our analysis, we fix $p = 3$, while r is allowed to take values 1 or 2, and vice versa through Hermitian conjugation.

Wilson coefficients as $\mathcal{C}_i \equiv \mathcal{C}_i / \Lambda^2$, where Λ is the NP scale. These rescaled coefficients have mass dimension [GeV^{-2}].

It is worth mentioning that, in order to match the general effective Lagrangian eq. (2.1) expressed in the mass basis with the SMEFT operator basis eq. (2.2) defined in the flavour basis at the scale (Λ). Hence, a flavour rotation of the relevant fields is required to find out the matching conditions. Since we are assuming that NP is mostly coupled to the top quark, it is logical to perform the analysis in *up-aligned* basis, where we define all the right-handed fields in the mass basis, and the left-handed lepton doublet in the mass basis of charged leptons, while the left-handed quark doublet is initially defined in an arbitrary flavour basis. In this basis, quark Yukawa matrices can be expressed as

$$\Gamma_u = U_u \Gamma_u^{\text{diag}}, \quad \Gamma_d = U_d \Gamma_d^{\text{diag}}, \quad q = \begin{pmatrix} U_{u_L}^\dagger u_L \\ U_{d_L}^\dagger d_L \end{pmatrix} \quad (2.4)$$

where U_{u_L} and U_{d_L} are unitary matrices, Γ_u^{diag} and Γ_d^{diag} are the diagonal Yukawa matrices, and u_L , d_L are the mass eigenstates of the quark doublet q . After performing a flavour rotation ($q \rightarrow U_{u_L} q$), which diagonalises the up-type Yukawa matrix, the quark doublet takes the form:

$$\Gamma_u = \Gamma_u^{\text{diag}}, \quad \Gamma_d = V_{\text{CKM}} \Gamma_d^{\text{diag}}, \quad q = \begin{pmatrix} u_L \\ V_{\text{CKM}} d_L \end{pmatrix} \quad (2.5)$$

where $V_{\text{CKM}} = (U_{d_L}^\dagger U_{u_L})$, and V_{CKM} is the Cabibbo-Kobayashi-Maskawa (CKM) matrix. Following this basis rotation, we obtain the tree-level matching condition of the SMEFT

operators with the effective Lagrangian in eq. (2.1), which are as given below

$$\begin{aligned}
(\xi_L)_{pr} &= \sqrt{2}v \frac{m_t}{g_s} \left(\mathcal{C}_{rp}^{uG} \right)^*, \quad (\xi_R)_{pr} = \sqrt{2}v \frac{m_t}{g_s} \mathcal{C}_{pr}^{uG}, \\
(\lambda_L)_{pr} &= \sqrt{2}v \frac{m_t}{e} \left(s_W \left(\mathcal{C}_{rp}^{uW} \right)^* + c_W \left(\mathcal{C}_{rp}^{uB} \right)^* \right), \quad (\lambda_R)_{pr} = \sqrt{2}v \frac{m_t}{e} \left(s_W \mathcal{C}_{pr}^{uW} + c_W \mathcal{C}_{pr}^{uB} \right), \\
(\kappa_L)_{pr} &= \sqrt{2}v \frac{c_W m_t}{g_W} \left(c_W \left(\mathcal{C}_{rp}^{uW} \right)^* - s_W \left(\mathcal{C}_{rp}^{uB} \right)^* \right), \quad (\kappa_R)_{pr} = \sqrt{2}v \frac{c_W m_t}{g_W} \left(c_W \mathcal{C}_{pr}^{uW} - s_W \mathcal{C}_{pr}^{uB} \right), \\
(X_L)_{pr} &= v^2 \left(\mathcal{C}_{pr}^{\phi q(1)} - \mathcal{C}_{pr}^{\phi q(3)} \right) \equiv v^2 \mathcal{C}_{pr}^{\phi q(-)}, \quad (X_R)_{pr} = v^2 \mathcal{C}_{pr}^{\phi u}, \\
(\eta_L)_{pr} &= \frac{3}{2}v^2 \left(\mathcal{C}_{rp}^{u\phi} \right)^*, \quad (\eta_R)_{pr} = \frac{3}{2}v^2 \mathcal{C}_{pr}^{u\phi}.
\end{aligned} \tag{2.6}$$

In eq. (2.6), the flavour indices p and r correspond to the quark generation labels. The matching conditions for the left- and right-handed *top – charm* effective couplings, as presented in eq. (2.1), require the inclusion of both index configurations $(p, r) = (2, 3)$ and $(3, 2)$. Similarly, for the *top – up* effective couplings in the left- and right-handed sectors, it is necessary to consider both $(p, r) = (1, 3)$ and $(3, 1)$ combinations.

This requirement arises because the effective operators describing FCNC interactions are constructed to respect the hermiticity of the Lagrangian. Consequently, for any off-diagonal flavour structure involving two distinct generations, both orderings of the flavour indices must be included to account for the operator and its Hermitian conjugate. Neglecting one of the two configurations would lead to an incomplete description of the interaction and violate the symmetry properties of the effective theory [3]. Eq. (2.6) represents the tree-level matching between the SMEFT operators and the effective Lagrangian given in eq. (2.1), where a total 10 effective couplings, together with 10 Hermitian conjugate effective couplings (not shown explicitly), are matched with a set of SMEFT WCs mentioned in table 1. Since vector-type SMEFT operators are Hermitian by construction, we take the corresponding top-FCNC vector couplings to be real, i.e., $X_L^* = X_L$ and $X_R^* = X_R$, while for the tensor $(\xi_{L(R)}, \lambda_{L(R)}, \kappa_{L(R)})$ and scalar $(\eta_{L(R)})$ type couplings, we retain their complex nature. Furthermore, this matching is performed at the top quark mass scale, μ_t . The parameters c_W and s_W denote the cosine and sine of the weak mixing angle, respectively, and v is the vacuum expectation value of the Higgs field, with $v \simeq 246$ GeV.

In this work, we assume that NP effects arise exclusively from FCNC interactions involving up-type quarks, particularly the top quark. We want to emphasise that our primary goal is to constrain rare top FCNC couplings using low-energy flavour observables and electroweak precision data. To this end, we map the effective operators in eq. (2.1) onto SMEFT operators that match at tree level. This SMEFT basis is chosen because its anomalous dimension matrix is known, enabling renormalisation group evolution (RGE) of WCs from the NP scale to the electroweak scale, μ_{EW} . Below μ_{EW} , the running to μ_b involves only QED and QCD corrections to low-energy operators, where SMEFT operators have no role. Therefore, even without SMEFT matching, constraints on top FCNC couplings can still be derived at both μ_{EW} and μ_b .

The SMEFT operators $\mathcal{O}_{pr}^{\phi q(1)}$ and $\mathcal{O}_{pr}^{\phi q(3)}$ can also generate down-type FCNCs through the same WCs. These contributions occur at tree level and impact rare low-energy processes,

which are subject to stringent experimental constraints. We analyse these effects separately. Although the WCs associated with $\mathcal{O}_{pr}^{\phi q,(1)}$ and $\mathcal{O}_{pr}^{\phi q,(3)}$ represent both up and down type FCNC interactions by single parameters in the SMEFT framework, their phenomenological implications vary across processes depending on the quark flavours involved. This variation arises from the decomposition of the $SU(2)_L$ gauge currents into up-type and down-type components, leading to distinct observable signatures even when the underlying couplings are identical.

In a model-independent EFT approach, constraints on WCs are extracted directly from experimental data and subsequently matched to NP scenarios, enabling bounds on WCs to be translated into limits on fundamental model parameters. Therefore, the bounds obtained on the up-type and down-type couplings are highly process-dependent and requires careful consideration when translating them into parameters of NP models. Conversely, model-dependent analyses may predict different patterns of FCNC contributions for up-type and down-type quarks. For example, as highlighted in refs. [21, 38–40], certain NP frameworks induce FCNC effects exclusively in rare top-quark processes without generating $b \rightarrow s$ transitions. Numerous such models exist, and further constructions are possible. Moreover, in scenarios where FCNC vertices arise only at the loop level, the effective couplings can deviate significantly from tree-level expectations. Accounting for these distinctions is essential for precision SMEFT fits and for the robust interpretation of experimental constraints across different processes.

Most of the SMEFT operators we consider, such as dipole and vector-like operators, can, in principle, mix with certain four-fermion operators under renormalisation group evolution (RGE). Examples include $\mathcal{O}_{prst}^{\ell equ(3)}$, $\mathcal{O}_{prst}^{\ell q(1)}$, $\mathcal{O}_{prst}^{\ell q(3)}$, $\mathcal{O}_{prst}^{\ell u}$, and \mathcal{O}_{prst}^{eu} , whose definitions and mixing patterns are detailed in refs. [41–43]. These operators typically involve combinations of leptons and quarks in different chiral structures and can mix through loop effects, thereby inducing corrections to the WCs of other operators (some of the operators from our chosen basis).

We have explicitly checked the size of these mixing contributions in the RGE running and find them to be extremely small, typically in the range of 10^{-3} to 10^{-5} , depending on the specific scenario and energy scale. For instance, the mixing of dipole operators into four-fermion operators is suppressed by loop factors and small Yukawa couplings. In contrast, the reverse mixing is similarly suppressed by gauge couplings and flavour structure. As a concrete example, the operator $\mathcal{O}_{prst}^{\ell equ(3)}$, which involves scalar-type interactions between leptons and quarks, can mix into dipole operators through diagrams involving Higgs and gauge bosons; however, the resulting contribution is proportional to the corresponding Yukawa coupling and is therefore negligible for all but the top quark.

Furthermore, these two classes of operators (dipole type and 4-fermion type operators) impact different sets of observables. Dipole operators primarily affect processes such as radiative decays, magnetic moments, FCCC processes and certain electroweak precision observables. In contrast, four-fermion operators contribute dominantly to contact interactions, scattering cross sections, and FCNC semileptonic rare decays like $b \rightarrow s\ell\ell$. Even in cases where both classes influence the same observable (e.g., semileptonic rare decays), their contributions enter with different Lorentz structures and kinematic dependencies, making

interference effects negligible. Consequently, the contribution of one class does not meaningfully alter the phenomenology of the other. Therefore, the mixing-induced effects are numerically negligible and can be safely ignored in our analysis without loss of accuracy or physical insight.

3 Methodology

As discussed earlier, a wide range of observables, including low-energy flavour observables, high-energy EWPOs, and key measurements related to the Higgs boson, W boson, and the top quark, are impacted at one loop by the top FCNC effective vertices defined in eq. 2.1. Our goal is to derive constraints on these effective couplings by performing an independent and global analysis of this broad class of observables. These constraints can then be translated into bounds on the corresponding SMEFT WCs.

In the effective theory framework, different operator bases are defined at different energy scales, with the appropriate degrees of freedom relevant to that scale. For example, to describe anomalous tbW couplings, we define the corresponding effective operators and compute the one-loop contributions from the top FCNC operators. The resulting anomalous couplings are obtained through a matching procedure at the top-quark scale, μ_t . Similarly, we extract effective couplings for processes such as $H \rightarrow b\bar{b}$, $H \rightarrow \gamma\gamma$, $H \rightarrow Z\gamma$, $gg \rightarrow H$, trilinear gauge couplings, top chromo-magnetic dipole moments, and W - and Z -pole observables by calculating the one-loop contributions of the top FCNC operators and applying the appropriate matching conditions. These effective couplings are need to be defined at the electroweak scale, μ_{EW} . In addition, we estimate the one-loop contributions of these operators to the oblique parameters and express the S , T , and U observables in terms of the top FCNC couplings. Also, in this case, we need to define these couplings at μ_{EW} .

For low-energy flavour observables, the relevant operator basis is the low-energy effective theory (LEFT) or weak effective theory (WET) basis, which we will specify later. Accordingly, we compute the one-loop contributions of the top FCNC operators to various low-energy observables and obtain the corresponding WCs of the LEFT operators through an appropriate matching procedure. Here, the matching will be obtained at μ_{EW} . However, to apply the low energy bounds we need to obtain the respective couplings at the scale $\mu_b = m_b$.

The impact of the operators defined at a high energy scale on the low energy processes/observables can be extracted by following appropriate matching calculations and RGE to relate the coefficients at different scales. The EFT approach provides a suitable framework to accomplish this task. Within the framework of EFT, RGEs allow us to consistently track the evolution of the couplings across different energy scales, while matching procedures enable us to connect two EFTs (in our analysis, SMEFT to Low Energy Effective Field Theory (LEFT)) by integrating out heavy degrees of freedom, within the range of validity of the EFT. To account for this, we have performed running followed by a one-loop matching between the SMEFT operator basis and the observables at different energy scales. We have followed the one-loop matching formalism formulated in the ref. [44].

We closely follow the methodology developed in our previous work [15], where a detailed

flowchart illustrating the full procedure is also provided. After defining our chosen sets of top-quark FCNC SMEFT operators at the NP scale (Λ), the matching to the observables at different energies is performed via the following steps.

- Running from $\Lambda \rightarrow \mu_t \rightarrow \mu_{\text{EW}}$: We evolve the SMEFT WCs \mathcal{C}_i from the new physics scale (Λ) down to the top quark mass scale ($\mu_t = m_t \simeq 172$ GeV), and subsequently to the electroweak scale ($\mu_{\text{EW}} = m_Z \simeq 91.2$ GeV). We perform this running at leading-logarithmic (LL) approximation using the anomalous dimension matrix (ADM) of the SMEFT operators, taken from the literature [41, 42, 45]. Since the effective top FCNC interactions are defined at the top quark mass scale, a tree-level matching between the SMEFT WCs and the effective top-quark couplings is essential at μ_t . Furthermore, we have performed one-loop matching with the LEFT operator basis and all the EWPOs, as well as other observables related to the Higgs boson, W boson, and top quark at the μ_{EW} scale, in order to effectively incorporate the constraints from these measurements. It is important to note that, since the scale separation between μ_{EW} , μ_W , μ_H , and μ_t is not significant and the effect of RG evolution is negligible over this range, we have encountered the EWPOs and the observables related to the top quark, Higgs boson, and W boson at the common scale μ_{EW} in our global analysis. The underlying running equations connecting two different energy scales in LL approximation can be written as:

$$\mathcal{C}_i(\mu) = \left(1 + \frac{\gamma_{ii}}{16\pi^2} \log\left(\frac{\mu}{\Lambda}\right)\right) \mathcal{C}_i(\Lambda) + \sum_{i \neq j} \frac{\gamma_{ij}}{16\pi^2} \log\left(\frac{\mu}{\Lambda}\right) \mathcal{C}_j(\Lambda). \quad (3.1)$$

Again, taking the reference NP scale as $\Lambda = 1$ TeV, the SMEFT Wilson coefficients at two different scales can be expressed as:

$$\begin{pmatrix} \mathcal{C}_{23}^{uB} \\ \mathcal{C}_{23}^{uW} \\ \mathcal{C}_{23}^{uG} \\ \mathcal{C}_{23}^{\phi u} \\ \mathcal{C}_{23}^{\phi q(1)} \\ \mathcal{C}_{23}^{\phi q(3)} \\ \mathcal{C}_{23}^{u\phi} \end{pmatrix}_{\mu_{\text{EW}}} = \begin{pmatrix} 0.888659 & 0.001755 & -0.025980 & 0 & 0 & 0 & 0 \\ 0.000585 & 0.921365 & -0.027466 & 0 & 0 & 0 & 0 \\ -0.019485 & -0.061798 & 1.04996 & 0 & 0 & 0 & 0 \\ 0 & 0 & 0 & 0.886147 & 0.000081 & 0 & 0 \\ 0 & 0 & 0 & 0 & 0.908814 & 0.050908 & 0 \\ 0 & 0 & 0 & 0 & 0.016969 & 0.955807 & 0 \\ 0.017356 & 0.007568 & -0.368257 & -0.010302 & 0 & -0.000030 & 0.977383 \end{pmatrix} \begin{pmatrix} \mathcal{C}_{23}^{uB} \\ \mathcal{C}_{23}^{uW} \\ \mathcal{C}_{23}^{uG} \\ \mathcal{C}_{23}^{\phi u} \\ \mathcal{C}_{23}^{\phi q(1)} \\ \mathcal{C}_{23}^{\phi q(3)} \\ \mathcal{C}_{23}^{u\phi} \end{pmatrix}_{\mu_1 \text{ TeV}} \quad (3.2)$$

The RGE evolution of the Wilson coefficient \mathcal{C}_{13} is similar to that of \mathcal{C}_{23} ; the only differences arise from the Yukawa-sector contributions, while the gauge-sector evolution is identical for both cases. The explicit expressions for the beta functions are provided in Appendix A. It is worth mentioning that these sets of SMEFT WCs can, in general, mix into other operators via renormalisation group running, which are not explicitly shown here but can be found in refs [41, 42, 45]. However, we have not accounted for their effects, as we have already stated earlier that the NP contribution in our analysis originates solely from tree-level top-quark FCNC interaction. These are the only sets of SMEFT operators that induce top-quark FCNC interactions at tree level.

- Running from $\mu_{\text{EW}} \rightarrow \mu_b$: The LEFT coefficients, which represent the low-energy observables, are further evolved from the electroweak scale (μ_{EW}) down to the $\mu_b \simeq 4.2 \text{ GeV}$ scale relevant for B -decay processes. We perform this running using ADM matrices provided in the refs [43, 46]. This running is particularly important, as QCD corrections play a crucial role in the renormalisation of the LEFT operators. The underlying running equation responsible for the evolution of LEFT couplings can be written as

$$\frac{d\vec{L}_i}{d \log \mu} = \frac{1}{16\pi^2} \sum_j \beta_{ij} \vec{L}_j = \frac{\alpha_s}{4\pi} \sum_j \beta_{ij}^s \vec{L}_j + \frac{\alpha_e}{4\pi} \sum_j \beta_{ij}^e \vec{L}_j. \quad (3.3)$$

Here, \vec{L}_i represents the set of LEFT WCs associated with various low-energy processes, while α_s and α_e denote the strong and electromagnetic couplings, respectively. The matrices β^s and β^e are the ADMs arising from QCD and QED corrections to the LEFT operators. Considering only linear-order corrections from QED and QCD, the RGE takes a simplified form that connects the LEFT WCs at two different energy scales.

$$\vec{L}_i(\mu) = U_{ij}(\mu, \mu_0) \vec{L}_j = \left[U_{ij}^s(\mu, \mu_0) + U_{ij}^e(\mu, \mu_0) \right] \vec{L}_j(\mu_0). \quad (3.4)$$

Here, U_{ij}^s and U_{ij}^e denote the evolution matrices arising from QCD and QED corrections, respectively. The values of these evolution matrices are taken from refs [46–49]. We will introduce the relevant LEFT operator basis and corresponding WCs when discussing the low-energy processes. Furthermore, the numerical solutions of the RGEs for these WCs, obtained by running them from the electroweak scale (μ_{EW}) down to the low-energy scale (μ_b), will be presented in the appropriate sections.

Once the low-energy observables, EWPOs, and other observables related to the Higgs boson, W boson, and top quark are expressed in terms of the SMEFT WCs $\mathcal{C}_i(\mu_{\text{EW}})$, we can perform a global χ^2 fit by constructing the log-likelihood function:

$$\begin{aligned} -2 \log \mathcal{L}(\mathcal{C}_i(\mu_{\text{EW}})) &= \chi^2(\mathcal{C}_i(\mu_{\text{EW}})) = \chi_{\text{Low}}^2(\mathcal{C}_i(\mu_{\text{EW}})) + \chi_{\text{EWPOs}}^2(\mathcal{C}_i(\mu_{\text{EW}})) + \chi_{\text{others}}^2(\mathcal{C}_i(\mu_{\text{EW}})), \\ &= \sum_{ij} \left(\mathcal{O}_i^{\text{theo}}(\mathcal{C}_i) - \mathcal{O}_i^{\text{exp}} \right) \left(\sigma^2 \right)_{ij}^{-1} \left(\mathcal{O}_j^{\text{theo}}(\mathcal{C}_j) - \mathcal{O}_j^{\text{exp}} \right). \end{aligned} \quad (3.5)$$

where $\mathcal{O}_i^{\text{theo}}$ denote the theoretical predictions of the observables, $\mathcal{O}_i^{\text{exp}}$ represent their corresponding experimental values, and \mathcal{C}_i are the SMEFT WCs defined at the scale μ_{EW} . The matrix $\left(\sigma^2 \right)_{ij}^{-1}$ corresponds to the inverse of the covariance matrix, incorporating both experimental and theoretical uncertainties and their correlations. We perform global fits of the WCs under different scenarios: one-parameter, two-parameter, and multi-parameter fits. Finally, we present our results in sec. 5, showing all effective couplings and SMEFT WCs at different energy scales (Λ_i), obtained by numerically solving the complete set of RGEs. All results are quoted at the 1σ confidence level (CL).

4 Impact on various observables

In the previous section, we outlined the methodology and theoretical framework of our analysis. Building upon that foundation, in this section, we present the complete set of observables from various energy sectors that are sensitive to the top-FCNC effective couplings. These include low-energy flavour observables, EWPOs, and high-energy collider measurements, ensuring that the NP effects are probed across a broad range of processes and scales.

4.1 Low Energy Observables

Low-energy observables associated with FCNC processes, such as radiative decays, semileptonic decays like $b \rightarrow d_j \ell^+ \ell^-$, rare and invisible decay modes, and FCCC processes, like $b \rightarrow c(u) \ell \nu$, are sensitive to the presence of top-quark FCNC interactions at the one-loop level. Since FCNC processes are rare and highly suppressed in the SM, they serve as excellent probes for new physics, providing stringent bounds on the corresponding NP couplings. Similarly, the FCCC processes are also useful in constraining the new physics information, given the wealth of improved measurements and the precision extractions of the observables associated with these processes.

We define all the LEFT couplings relevant to low-energy observables as L_i , following the operator basis notation of ref. [43]. Furthermore, for clarity and consistency with the existing literature, we also provide the correspondence between this LEFT basis and most commonly used operator bases for the study of low-energy observables.

4.1.1 Observables related to FCNC Processes

In the SM, FCNC processes are loop suppressed, making them highly sensitive to the new physics. In this subsection, we study observables associated with decays of B and K mesons and use their experimental measurements to constrain the top FCNC effective couplings.

Radiative decays: Radiative decays, such as $b \rightarrow s(d)\gamma$, are loop-induced processes in the SM and proceed via electromagnetic penguin diagrams. In the SM, these decays predominantly occur via loops involving heavy virtual particles, especially the top quark, along with W bosons. In our analysis, alongside the SM penguin loop contributions, we also obtain additional NP effects from top FCNC operators, as shown in figs. 1a and 1b. We can match the contributions of these diagrams to the most general Hamiltonian describing radiative decays ($b \rightarrow d_i \gamma$) which can be written as (in WET basis):

$$\mathcal{H}_{\text{eff}}^{b \rightarrow d_i \gamma} = -\frac{4G_F}{\sqrt{2}} V_{tb} V_{td_i}^* \sum_{i=7,8} (C_i(\mu) O_i + C'_i(\mu) O'_i), \quad (4.1)$$

Here, $d_i = b, s$ are the down-type quarks involved in the radiative transition, and the explicit expressions for the operators appearing in eq. (4.1) are given below:

$$O_7 = \frac{e}{16\pi^2} m_b (\bar{d}_j \sigma_{\mu\nu} P_R b) F^{\mu\nu}, \quad O'_7 = \frac{e}{16\pi^2} m_b (\bar{d}_j \sigma_{\mu\nu} P_L b) F^{\mu\nu}, \quad (4.2a)$$

$$O_8 = \frac{g_s}{16\pi^2} m_b (\bar{d}_j \sigma_{\mu\nu} T^a P_R b) G^{\mu\nu a}, \quad O'_8 = \frac{g_s}{16\pi^2} m_b (\bar{d}_j \sigma_{\mu\nu} T^a P_L b) G^{\mu\nu a}. \quad (4.2b)$$

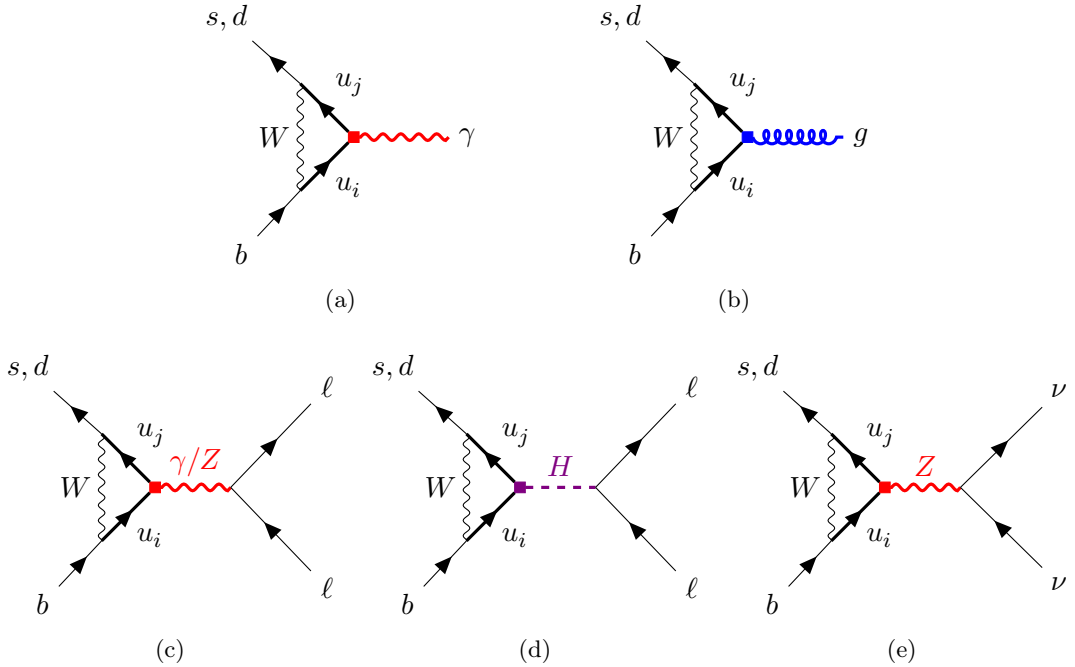


Figure 1. Feynman diagrams for various FCNC processes receiving contributions from top FCNC interactions. Here, u_i and u_j represent up-type quarks, where one is the top quark (t) and the other can be either an up (u) or charm (c) quark.

In the SM, both the coefficients C_7 and C_8 contribute to the radiative decay $b \rightarrow s(d)\gamma$. In addition to the SM contributions, the WCs defined above may include NP contributions. To disentangle the NP effects from the SM ones, we redefine the low-energy WCs as

$$C_i(\mu) = C_i^{\text{SM}}(\mu) + C_i^{\text{NP}}(\mu). \quad (4.3)$$

The SM predictions for the WCs $C_i^{\text{SM}}(\mu_b)$, incorporating both QED and QCD corrections, are available in the literature [50].

In our analysis, we obtain NP contributions to the operators O_7 and O_8 . It is important to note that the contribution from O_8 to the $b \rightarrow d_i\gamma$ process arises through RGE mixing with the O_7 operator [47, 48], and

$$\begin{pmatrix} C_7 \\ C_8 \end{pmatrix}_{\mu_b} = \begin{pmatrix} 0.66301 & 0.09259 \\ 0.00326 & 0.69877 \end{pmatrix} \begin{pmatrix} C_7 \\ C_8 \end{pmatrix}_{\mu_{\text{EW}}}. \quad (4.4)$$

After computing the one-loop diagrams and applying the appropriate matching conditions, we express the C_i^{NP} in terms of the top-quark FCNC couplings and the relevant mass scales. These matching relations are obtained at the electroweak scale. It is important to note that the WET basis defined above is not identical to the LEFT basis; the mapping between these two sets of couplings can be found in ref [44]. Using these relations, we rewrite the NP

contributions to the $C_{7,8}^{\text{NP}}(\mu)$ in terms of the corresponding LEFT coefficients as follows:

$$C_7^{\text{NP}}(\mu) = N_{d_i b}^{\text{rad}} \frac{e}{m_b} L_{d_i b}^{d\gamma}(\mu), \quad C_8^{\text{NP}}(\mu) = N_{d_i b}^{\text{rad}} \frac{e^2}{g_s m_b} L_{d_i b}^{dG}(\mu). \quad (4.5)$$

The detail mathematical expressions for $L_{d_i b}^{d\gamma}(\mu)$ and $L_{d_i b}^{dG}(\mu)$ are given in eqs. (B.1a-B.1b) in the Appendix B. Here, the prefactor $(N_{d_i b}^{\text{rad}})^{-1} = \frac{4G_F}{\sqrt{2}} \frac{\alpha_{\text{em}}}{4\pi} V_{ts}^* V_{tb}$, where α_{em} denotes the fine-structure constant, approximately equal to 1/127. Finally, we obtain $C_{7,8}^{\text{NP}}(\mu_b)$ by evolving these expressions using the RGEs defined in eq. 4.4.

In our numerical analysis, we include measurements of both inclusive and exclusive radiative decays provided by various experimental collaborations [51–54]. A list of different radiative processes, along with their corresponding SM predictions and experimental values, is tabulated in one of our previous works [15]. The branching ratio of the inclusive radiative decay $B \rightarrow X_s \gamma$, in the presence of NP WCs, can be expressed as [55]:

$$\mathcal{B}(B \rightarrow X_s \gamma) \times 10^4 = (3.40 \pm 0.17) - 8.25 C_7^{\text{NP}}(\mu_{\text{EW}}) - 2.10 C_8^{\text{NP}}(\mu_{\text{EW}}). \quad (4.6)$$

On the other hand, the branching ratios for exclusive decays into a vector meson can be written as [56, 57]:

$$\mathcal{B}(B_q \rightarrow V\gamma) = \tau_{B_q} \frac{G_F^2 \alpha_{\text{em}} m_{B_q}^3 m_b^2}{32\pi^3} \left(1 - \frac{m_V^2}{m_{B_q}^2}\right)^3 |\lambda_t|^2 \left(|C_7(\mu_b)|^2 + |C'_7(\mu_b)|^2\right) T_1(0), \quad (4.7)$$

where $\lambda_t = V_{tq}^* V_{tb}$, and $T_1(0)$ is the tensor form factor, whose values can be found in [58].

Semileptonic $b \rightarrow d_i \ell \ell$ decays: The general Low-energy Lagrangian describing the $b \rightarrow d_i \ell^+ \ell^-$ transition is expressed as:

$$\mathcal{H}_{\text{eff}}^{b \rightarrow d_i \ell \ell} = -\frac{4G_F}{\sqrt{2}} V_{tb} V_{td_j}^* \left[\sum_{i=1}^6 C_i(\mu) O_i(\mu) + \sum_{i=7,8,9,10,P,S} \left(C_i(\mu) O_i + C'_i(\mu) O'_i \right) \right], \quad (4.8)$$

Among this large set of operators, in our analysis, the dipole-type operators O_7 , O_8 , the vector-type operators O_9 , O_{10} and the scalar-type operator O_S receive additional contributions to their couplings from top-quark FCNC interactions, as illustrated in the diagrams shown in fig. 1c, 1d. We are using the notation for O_i from refs. [59–61], where operator structure of O_7 and O_8 are already mentioned in eq. (4.2a).

$$O_9 = \frac{e^2}{16\pi^2} (\bar{d}_j \gamma_\mu P_L b) (\bar{\ell} \gamma^\mu \ell), \quad O'_9 = \frac{e^2}{16\pi^2} (\bar{d}_j \gamma_\mu P_R b) (\bar{\ell} \gamma^\mu \ell), \quad (4.9a)$$

$$O_{10} = \frac{e^2}{16\pi^2} (\bar{d}_j \gamma_\mu P_L b) (\bar{\ell} \gamma^\mu \gamma_5 \ell), \quad O'_{10} = \frac{e^2}{16\pi^2} (\bar{d}_j \gamma_\mu P_R b) (\bar{\ell} \gamma^\mu \gamma_5 \ell), \quad (4.9b)$$

$$O_S = \frac{e^2}{16\pi^2} m_b (\bar{d}_j P_R b) (\bar{\ell} \ell), \quad O'_S = \frac{e^2}{16\pi^2} m_b (\bar{d}_j P_L b) (\bar{\ell} \ell). \quad (4.9c)$$

where $\ell = e, \mu, \tau$, but we restrict our analysis to $\ell = \mu$, as only upper bounds exist for other lepton flavors. Similar to the radiative case, we follow the same procedure to incorporate

NP effects within the low-energy WCs. Specifically, we split the contributions to the WCs into two parts: one arising solely from SM corrections (QCD and QED), and the other from NP effects. Again, one can find the SM contribution (C_i^{SM}) from the ref. [50]. Like the SM, NP contributions also arise via penguin diagrams shown in fig. 1. Among the possible NP diagrams, the one proportional to $V_{tb}V_{cs}^*$ provides the dominant contribution. We have performed the NP loop calculation and subsequently obtained the low-energy WCs in terms of top FCNC couplings at the electroweak scale following the appropriate matching conditions.

Like the radiative decay, we draw a connection between LEFT WCs and low-energy WCs $C_9^{\text{NP}}, C_{10}^{\text{NP}}$ and C_S^{NP} [43],

$$C_9^{\text{NP}}(\mu) = \lambda_1 \left(L_{\mu\mu d_i b}^{V,LL} + L_{d_i b\mu\mu}^{V,LR} \right), \quad C_9'^{\text{NP}}(\mu) = \lambda_1 \left(L_{\mu\mu d_i b}^{V,LR} + L_{\mu\mu d_i b}^{V,RR} \right), \quad (4.10\text{a})$$

$$C_{10}^{\text{NP}}(\mu) = \lambda_1 \left(-L_{\mu\mu d_i b}^{V,LL} + L_{d_i b\mu\mu}^{V,LR} \right), \quad C_{10}'^{\text{NP}}(\mu) = \lambda_1 \left(-L_{\mu\mu d_i b}^{V,LR} + L_{\mu\mu d_i b}^{V,RR} \right), \quad (4.10\text{b})$$

$$C_S^{\text{NP}}(\mu) = \frac{\lambda_1}{m_b} \left(L_{\mu\mu d_i b}^{S,RR} + L_{\mu\mu b d_i}^{S,RL*} \right), \quad C_S'^{\text{NP}}(\mu) = \frac{\lambda_1}{m_b} \left(L_{\mu\mu d_i b}^{S,RL} + L_{\mu\mu b d_i}^{S,RR*} \right), \quad (4.10\text{c})$$

$$(\lambda_1)^{-1} = -\frac{4G_F}{\sqrt{2}} V_{tb} V_{ts}^* \frac{e^2}{16\pi^2}. \quad (4.10\text{d})$$

where L_i are the different LEFT Wilson coefficients. We present the expressions of all these LEFT WCs in eqs. (B.1c-B.1e) in the Appendix B¹.

Furthermore, we have to run down our low-energy WCs to the scale of μ_b to utilise the experimental inputs related to $b \rightarrow d_i \ell \ell$ observables, and the governing RGEs connecting low-energy WCs at the scale μ_b are given by:

$$\begin{pmatrix} C_9 \\ C_{10} \\ C_S \end{pmatrix}_{\mu_b} = \begin{pmatrix} 0.99522 & 0.00716 & 0 \\ 0.00716 & 1.0 & 0 \\ 0 & 0 & 1.37433 \end{pmatrix} \begin{pmatrix} C_9 \\ C_{10} \\ C_S \end{pmatrix}_{\mu_{\text{EW}}}. \quad (4.11)$$

In our analysis, we consider a comprehensive set of observables associated with both leptonic decays ($B_s^0 \rightarrow \ell^+ \ell^-$, $B^0 \rightarrow \ell^+ \ell^-$) and semileptonic decays ($B \rightarrow K^{(*)} \mu^+ \mu^-$, $B \rightarrow \phi \mu^+ \mu^-$). A substantial amount of experimental data is available for these channels, including measurements of differential branching fractions, CP asymmetries, and various angular observables. These measurements have been performed by several experimental collaborations, notably LHCb[63–69], Belle[70], CDF [71], ATLAS[72], and CMS[73]. We also accounted for precise measurements of the lepton flavour universality (LFU) ratios R_K and R_{K^*} , which, after recent updates by LHCb [69], are consistent with the SM within the 1σ confidence interval. Nevertheless, these observables remain highly sensitive to NP coupled

¹A discussion on one-loop SMEFT and LEFT matching for a subset of our chosen SMEFT operator sets relevant to the $b \rightarrow s \ell \ell$ process is already available in the literature [62]. We have verified our results against these existing studies.

to light leptons, thereby providing stringent bounds. A detailed discussion of the observables related to the $b \rightarrow s\mu^+\mu^-$ channels can be found in one of our previous works [74], which we closely follow in our analysis.

Leptonic rare decays: Dileptonic decays of neutral mesons are another important class of decay channels for probing NP, as they are rare and highly suppressed within the SM. In our analysis, we have accounted for the following processes: $B_s^0 \rightarrow \ell^+\ell^-$, $B^0 \rightarrow \ell^+\ell^-$, $K_{L,S} \rightarrow \ell^+\ell^-$. For the B meson decays, we consider only $\ell = \mu$, as for other lepton flavours, only upper bounds on the branching fractions are currently available. Rare leptonic decays can also be described using the effective Hamiltonian given in eq. (4.8). For K -meson decays, the same effective Hamiltonian applies with the replacements $b \leftrightarrow s$ and $s \leftrightarrow d$.

Based on the Hamiltonian mentioned above the expressions for the branching fraction for the rare dileptonic decays can be written as

$$\mathcal{B}(B_q \rightarrow \mu^+\mu^-) = \tau_{B_q} f_{B_q}^2 m_{B_q}^3 \frac{G_F^2 \alpha^2}{64\pi^3} |V_{tq}^* V_{tb}|^2 \beta_\mu(m_{B_q}^2) \left[\frac{m_{B_q}^2}{m_b^2} |C_s - C'_s|^2 \left(1 - \frac{4m_\mu^2}{m_{B_q}^2} \right) + \left| \frac{m_{B_q}}{m_b} (C_p - C'_p) + 2 \frac{m_\mu}{m_{B_q}} (C_{10} - C'_{10}) \right|^2 \right], \quad (4.12)$$

where $\beta_\mu(q^2) = \sqrt{1 - \frac{4m_\mu^2}{q^2}}$, and the B_q meson decay constant is defined via the matrix element

$$\langle 0 | \bar{s} \gamma_\mu P_L b | B_q(p) \rangle = \frac{i}{2} f_{B_q} p_\mu, \quad (4.13)$$

where $q = (d, s)$. We have used the values of the decay constants: $f_B = (190.0 \pm 1.3)$ MeV and $f_{B_s} = (230.3 \pm 1.3)$ MeV [75], whereas for other input we have used the values from PDG24 [76]. In the SM, the branching ratio for $B_q \rightarrow \ell^+\ell^-$ receives contributions solely from the coupling C_{10} . However, in the presence of physics beyond the SM, additional contributions can arise from the other WCs C_S, C'_S, C_P, C'_P , and C'_{10} . In our analysis, the NP contributions enter through C_S^{NP} and C_{10}^{NP} WCs.

The most recent experimental measurement [77, 78] provides

$$\mathcal{B}(B^0 \rightarrow \mu^+\mu^-)^{\text{Exp}} = (1.2_{-0.7}^{+0.8} \pm 0.1) \times 10^{-10}, \quad \mathcal{B}(B_s^0 \rightarrow \mu^+\mu^-)^{\text{Exp}} = (3.83_{-0.36}^{+0.38} \pm 0.24) \times 10^{-9}.$$

The corresponding SM predictions for the branching ratios are given in ref. [79]:

$$\mathcal{B}(B^0 \rightarrow \mu^+\mu^-)^{\text{SM}} = (1.03 \pm 0.05) \times 10^{-10}, \quad \mathcal{B}(B_s^0 \rightarrow \mu^+\mu^-)^{\text{SM}} = (3.66 \pm 0.14) \times 10^{-9}.$$

$K_L \rightarrow \mu^+\mu^-$ decays: For the $K_L \rightarrow \mu^+\mu^-$ decays, there will be the short and the complex long-distance contributions in the decay amplitude. Only the short-distance (SD) contributions can be reliably calculated, as they arise from perturbative electroweak loops. For conservative bounds on the long-distance contribution, the readers may look at the

refs. [80, 81] which suffer from significant hadronic uncertainties. The short-distance contribution in this dileptonic kaon decay can be written as [82]:

$$\begin{aligned} \mathcal{B}(K_L \rightarrow \mu^+ \mu^-)_{\text{SD}} = & \tau_{K_L} f_K^2 m_K \frac{G_F^2 \alpha^2}{8\pi^3} m_\mu^2 \beta_\mu(m_K^2) \\ & \times \left\{ \left[\Re(V_{ts}^* V_{td} \hat{P}) \right]^2 + \left[\Im(V_{ts}^* V_{td} \hat{S}) \right]^2 \right\} \end{aligned} \quad (4.14)$$

with

$$\begin{aligned} \hat{P}(K) &\equiv (C_{10} - C'_{10}) + \frac{m_K^2}{2m_\mu} \frac{m_s}{m_d + m_s} (C_P - C'_P) \\ \hat{S}(K) &\equiv \beta_\mu(m_K^2) \frac{m_K^2}{2m_\mu} \frac{m_s}{m_d + m_s} (C_s - C'_s) \end{aligned}$$

The experimental measurement reported by the Particle Data Group (PDG) gives

$$\mathcal{B}(K_L \rightarrow \mu^+ \mu^-)_{\text{Exp}}^{\text{Exp}} = (6.84 \pm 0.11) \times 10^{-9}, \quad (4.15)$$

while the SM prediction for the SD contribution is significantly smaller [82]:

$$\mathcal{B}(K_L \rightarrow \mu^+ \mu^-)_{\text{SD}}^{\text{SM}} = (0.79 \pm 0.12) \times 10^{-9}. \quad (4.16)$$

A conservative upper bound on the short-distance component has been derived in the literature (see, e.g., ref. [81]):

$$(K_L \rightarrow \mu^+ \mu^-)_{\text{SD}} < 2.5 \times 10^{-9}. \quad (4.17)$$

This limit is obtained using the experimental constraint on the branching ratio of $K_L \rightarrow \gamma\gamma$ decays, which dominate the long-distance contribution to $K_L \rightarrow \mu^+ \mu^-$, for the details see the ref. [81]. In our analysis, we adopt this upper bound to restrict the parameter space of possible NP scenarios.

Invisible decays: Invisible decays constitute another important class of channels for probing new physics. In this analysis, we have studied the effects on various $P \rightarrow P' \nu \bar{\nu}$ channels, where P denotes a pseudoscalar meson and P' denotes either a pseudoscalar or a vector meson. For the decay of B mesons (both charged and neutral), the underlying quark-level transition is $b \rightarrow s(d) \nu \bar{\nu}$, while for K meson decays, it is governed by the transition $s \rightarrow d \nu \bar{\nu}$. Recently, the Belle collaboration [83] has reported the measurement of the di-neutrino channel $B^+ \rightarrow K^+ \nu \bar{\nu}$, for the first time. In our analysis, we have included the available data on the branching fractions $\mathcal{B}(B^+ \rightarrow K^+ \nu \bar{\nu})$, $\mathcal{B}(B^0 \rightarrow K^{*0} \nu \bar{\nu})$ and $\mathcal{B}(K^+ \rightarrow \pi^+ \nu \bar{\nu})$ which we have presented in table. 2, where the statistical uncertainties are also quoted.

With the assumptions that the right-handed neutrinos are absent and the neutrinos are Dirac types, the most general effective Hamiltonian for $b \rightarrow d_i \nu \bar{\nu}$ can be written as

$$\mathcal{H}^{b \rightarrow d_i \nu \bar{\nu}} = \frac{4G_F}{\sqrt{2}} V_{tb} V_{td_i}^* (\mathcal{C}_L^\nu \mathcal{O}_L^\nu + \mathcal{C}_R^\nu \mathcal{O}_R^\nu) \quad (4.18)$$

Branching Ratio	SM values	Experimental values
$\mathcal{B}(B^+ \rightarrow K^+ \nu \bar{\nu})$	$(5.22 \pm 0.15 \pm 0.28) \times 10^{-6}$ [84]	$(2.3 \pm 0.5^{+0.5}_{-0.4}) \times 10^{-5}$ [83]
$\mathcal{B}(B^0 \rightarrow K^{*0} \nu \bar{\nu})$	$(9.47 \pm 1.28 \pm 0.57) \times 10^{-6}$ [84]	$(3.8^{+2.9}_{-2.6}) \times 10^{-5}$ [85] $< 1.8 \times 10^{-5}$ [86]
$\mathcal{B}(K^+ \rightarrow \pi^+ \nu \bar{\nu})$	$(8.60 \pm 0.42) \times 10^{-11}$ [87]	$(1.06^{+0.40}_{-0.34} \pm 0.09) \times 10^{-10}$ [88]

Table 2. Updated SM predictions and experimental measurements of the branching ratios for invisible decays of B and K mesons.

where

$$\mathcal{O}_L^\nu = \frac{e^2}{16\pi^2} (\bar{d}_j \gamma_\mu P_L b) (\bar{\nu} \gamma^\mu P_L \nu), \quad \mathcal{O}_R^\nu = \frac{e^2}{16\pi^2} (\bar{d}_j \gamma_\mu P_R b) (\bar{\nu} \gamma^\mu P_L \nu), \quad (4.19)$$

Using the above Hamiltonian, we obtain the differential decay rates of various B meson decay channels, which are given by [84, 89]:

$$\frac{d\mathcal{B}(B^+ \rightarrow K^+ \nu \bar{\nu})}{dq^2} = \tau_B \frac{G_F^2 \alpha^2}{256\pi^5} \frac{\lambda(q^2, m_B^2, m_K^2)^{3/2}}{m_B^3} |V_{tb} V_{ts}^*|^2 \left[f_+(q^2) \right]^2 |C_L^\nu + C_R^\nu|^2, \quad (4.20)$$

where λ is the Källén function, defined as $\lambda(a^2, b^2, c^2) = (a^2 - (b - c)^2)(a^2 - (b + c)^2)$, q^2 is the dineutrino invariant mass squared ranging over $0 < q^2 \leq (m_B - m_K)^2$, and $f_+(q^2)$ denotes the $B \rightarrow K$ transition form factor. For $B \rightarrow K^* \nu \bar{\nu}$ decay, the differential decay rate distribution is given by

$$\begin{aligned} \frac{d\mathcal{B}(B \rightarrow K^* \nu \bar{\nu})}{dq^2} = & \tau_B \frac{G_F^2 \alpha^2}{128\pi^5} \frac{\lambda(q^2, m_B^2, m_{K^*}^2)^{1/2} q^2}{m_B^3} (m_B + m_{K^*})^2 |V_{tb} V_{ts}^*|^2 \\ & \times \left\{ \left(\left[A_1(q^2) \right]^2 + \frac{32m_B^2 m_{K^*}^2}{q^2 (m_B + m_{K^*})^2} \left[A_{12}(q^2) \right]^2 \right) |C_L^\nu - C_R^\nu|^2 \right. \\ & \left. + \frac{\lambda(q^2, m_B^2, m_{K^*}^2)}{(m_B + m_{K^*})^4} \left[V(q^2) \right]^2 |C_L^\nu + C_R^\nu|^2 \right\} \end{aligned} \quad (4.21)$$

Here, $A_1(q^2)$, $A_{12}(q^2)$, and $V(q^2)$ are the form factors associated with the $B \rightarrow K^*$ transition. We have used the values of the decay constants $f_K = (155.7 \pm 0.3)$ MeV and $f_{K^*} = (205 \pm 6)$ MeV [75]. All form factors relevant to the $B \rightarrow K$ and $B \rightarrow K^*$ decays are adopted from ref. [84], where a combination of inputs from Lattice QCD (HPQCD [90], FNAL/MILC[91]) and Light-Cone Sum Rules (LCSR)[58] has been utilised.

In our scenario, the NP contributions in these modes will arise via the diagrams shown in fig. 1e, and contribute to the left-handed vector-type WC C_L^ν . In the SM as well, only the left-handed vector current contributes to these processes. These low-energy couplings can again be decomposed into SM and NP parts, where the NP Wilson coefficients can be expressed in terms of the LEFT coefficients as:

$$C_L^\nu \text{NP} = -\lambda_1 L_{\nu \nu d_i b}^{V,LL}, \quad C_R^\nu \text{NP} = 0. \quad (4.22)$$

We have used the following SM values of the WCs: $C_L^\nu{}^{\text{SM}} = (-12.64 \pm 0.14)$ and $C_R^\nu{}^{\text{SM}} = 0$. In order to utilise the experimental measurements of invisible decays, RGEs of the Wilson coefficients are required. However, it is important to note that the coefficients $C_{L,R}^\nu$ do not evolve under the RGEs [46]. Hence, we can approximate the NP contributions at low energy as $C_L^{\nu,\text{NP}}(\mu_b) \approx C_L^{\nu,\text{NP}}(\mu_{\text{EW}})$. The expression for $C_L^{\nu,\text{NP}}$ in terms of top FCNC couplings is presented in eq. B.1f in the Appendix B.

The effective Hamiltonian and the operator structure describing the $s \rightarrow d\nu\bar{\nu}$ transition are the same as in eq. 4.18 with the replacements $b \leftrightarrow s$ and $s \leftrightarrow d$. The expression for the branching ratio of $K^+ \rightarrow \pi^+ \nu\bar{\nu}$ can be written as given in ref. [87, 92].

$$\mathcal{B}(K^+ \rightarrow \pi\nu\bar{\nu}) = 3\lambda_2^{-2} J_V^{K^+} |C_L^\nu + C_R^\nu|^2. \quad (4.23)$$

with

$$J_V^{K^+} = \frac{1}{\Gamma_{K^+}^{\text{Exp}}} \frac{1}{3 \cdot 2^9 \pi^3 m_{K^+}^3} \int ds \lambda^{3/2}(s, m_{K^+}^2, m_{\pi^+}^2) \left| f_+^{K^+}(s) \right|^2 = 0.23 G_F^{-2} \quad (4.24a)$$

$$(\lambda_2)^{-1} = \frac{4G_F}{\sqrt{2}} V_{td} V_{ts}^* \frac{e^2}{16\pi^2}, \quad C_L^\nu{}^{\text{SM}} = \lambda_2 \times (1.30 \times 10^{-10} \text{ GeV}^{-2}), \quad C_R^\nu{}^{\text{SM}} = 0 \quad (4.24b)$$

Note that the branching ratio expression in eq. (4.23) contains only the vector-type current. However, it can be further parametrised in terms of scalar and tensor currents [87, 92]. Also, for this decay we obtain $C_R^{\nu,\text{NP}} = 0$. Since the SM contribution is purely vectorial and our NP analysis also yields only vector-type currents, we restrict our discussion to this case.

Meson Mixing: In our analysis, we also investigate the impact of various neutral meson mixing processes. The contribution from $B^0 - \bar{B}^0$ mixing is found to be numerically insignificant. This is because such mixing effects arise only at the two-loop level for the top FCNC NP operators, requiring double insertions of penguin-type topologies [see fig. (1a–1b)]. We have explicitly verified that these contributions do not lead to any substantial impact on the NP parameter space.

Furthermore, we examine the contributions to $D^0 - \bar{D}^0$ mixing. In the SM, this process is highly suppressed due to the CKM hierarchy and is challenging to compute, as it is predominantly governed by long-distance (LD) effects. In our scenario, the mixing amplitude arises through box diagrams with *quadruple insertions*, making the diagrams proportional to the product of couplings, such as $C_i C_j C_k C_l / \Lambda^8$. The $D^0 - \bar{D}^0$ mixing might play an important role in constraining these product couplings, which is beyond the scope of the present study. However, we have explicitly checked that the allowed ranges obtained for individual couplings from other inputs are fully consistent with current data on the $D^0 - \bar{D}^0$ mixing amplitude.

4.1.2 Observables related to FCCC Processes

The FCCC processes involve transitions between quarks of different flavours mediated by charged weak currents, typically through the exchange of W^\pm bosons. In the SM, these

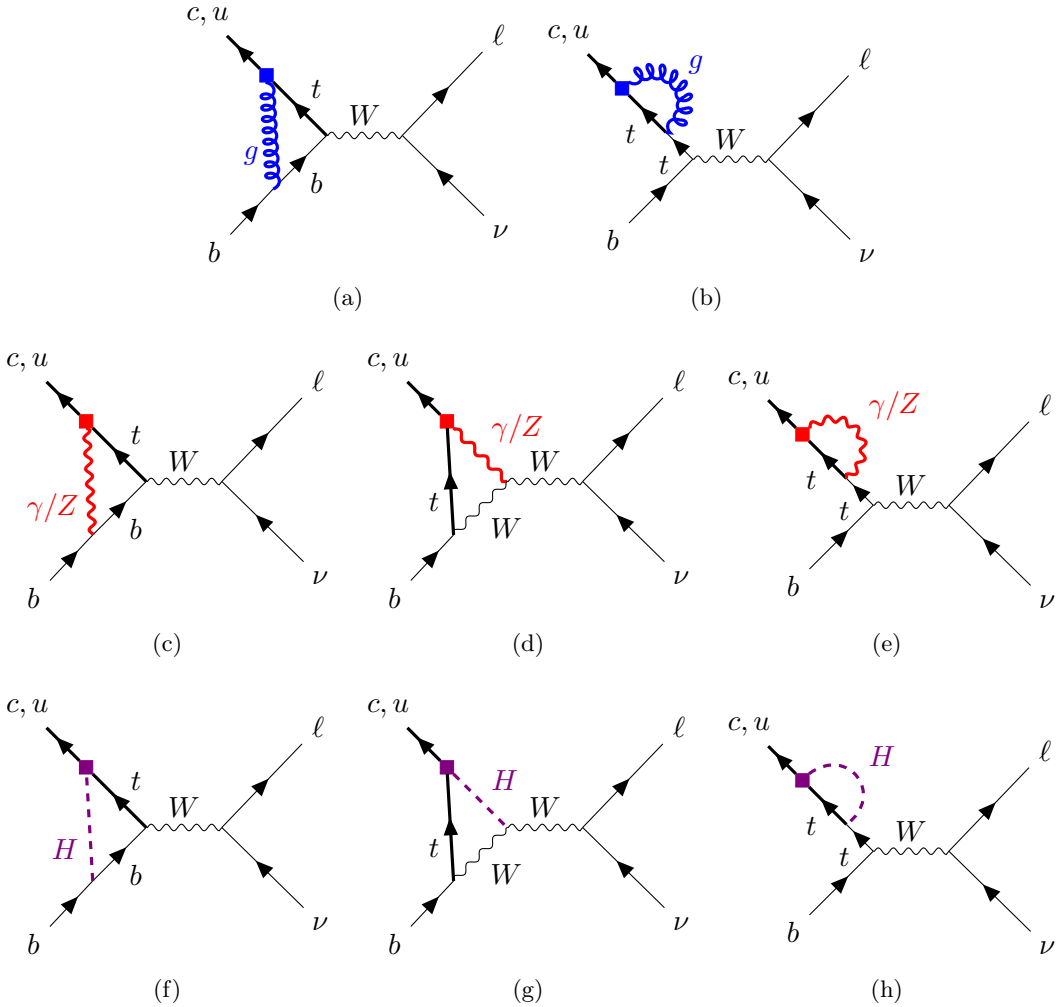


Figure 2. Feynman diagrams contributing to the FCCC processes $(b \rightarrow c(u) \ell \nu)$. Similarly, top FCNC couplings also affect the quark-level transitions $c \rightarrow s(d) \ell \nu$ and $s \rightarrow u \ell \nu$, although those diagrams are not explicitly shown here.

processes occur at the tree level, making them experimentally accessible. Their coupling strengths provide direct measurements of the CKM matrix elements, offering a powerful avenue to test the flavour structure and internal consistency of the SM. Because these processes are unsuppressed in the SM, they serve as an exceptionally sensitive probe for NP; any deviation from SM predictions would be a clear signal of NP. Given the relatively high-precision measurements and the relatively clean theoretical predictions in these channels, they provide a powerful means to impose stringent constraints on NP scenarios that might contribute to these processes, constraints that are expected to become even stronger with future data.

In this subsection 4.1.2, we study the impact of various top FCNC couplings on semileptonic and leptonic decays of B , B_s , K , D and D_s mesons. In addition, we also explore the contribution of NP coupling to anomalous $t \rightarrow bW$ couplings.

Leptonic and Semi-leptonic decays: In our scenario, the contributions in the FCCC semileptonic and leptonic decays will be via the one-loop diagrams shown in fig. 2. The resulting effective Hamiltonian relevant to the processes $d_i \rightarrow u_j \ell \nu_\ell$ can be written as:

$$\mathcal{H}^{d_i \rightarrow u_j \ell \nu_\ell} = \frac{4G_F}{\sqrt{2}} V_{u_j d_i} \left[(1 + C_{V_L}) O_{V_L} + C_{V_R} O_{V_R} \right] \quad (4.25)$$

with the operator defined as

$$O_{V_L} = (\bar{u}_j \gamma^\mu P_L d_i) (\bar{\ell} \gamma_\mu P_L \nu_\ell), \quad O_{V_R} = (\bar{u}_j \gamma^\mu P_R d_i) (\bar{\ell} \gamma_\mu P_L \nu_\ell). \quad (4.26)$$

Note that the most general effective Hamiltonian for $d_i \rightarrow u_j \ell \nu_\ell$ transition also contains scalar- and tensor-type four fermion currents. However, the diagrams in fig. 2 will contribute only in C_{V_L} and C_{V_R} , respectively. In the SM, both C_{V_L} and C_{V_R} are zero. The detailed mathematical expressions for C_{V_L} and C_{V_R} at the scale μ_{EW} are discussed in Appendix B, and we obtain the corresponding WCs at the scale μ_b following the given RGEs as given below

$$\begin{pmatrix} C_{V_L} \\ C_{V_R} \end{pmatrix}_{\mu_b} = \begin{pmatrix} 1.00716 & 0 \\ 0 & 1.00358 \end{pmatrix} \begin{pmatrix} C_{V_L} \\ C_{V_R} \end{pmatrix}_{\mu_{\text{EW}}}. \quad (4.27)$$

Using the effective Hamiltonian in eq. (4.25), we obtain the differential decay rate for the process $P \rightarrow M \ell \nu$, where P and M are pseudoscalar mesons, corresponding to the quark-level transition $d_i (u_i) \rightarrow u_j (d_j) \ell \nu_\ell$ [93], as:

$$\begin{aligned} \frac{d\Gamma(P \rightarrow M \ell \nu_\ell)}{dq^2} &= \frac{G_F^2 |V_{u_j d_i}|^2}{192\pi^3 m_P^3} q^2 \sqrt{\lambda(q^2, m_P^2, m_M^2)} \left(1 - \frac{m_\ell^2}{q^2}\right)^2 |1 + C_{V_L} + C_{V_R}|^2 \\ &\times \left\{ \left(1 + \frac{m_\ell^2}{2q^2}\right) H_{V,0}^{s,2} + \frac{3}{2} \frac{m_\ell^2}{q^2} H_{V,t}^{s,2} \right\}, \end{aligned} \quad (4.28)$$

All the relevant parameters in eq. (4.28), including the helicity amplitudes H_V , are taken from ref. [93, 94]. Similarly, the branching fraction for the leptonic decay $P \rightarrow \ell \nu_\ell$ can be written as:

$$\mathcal{B}(P \rightarrow \ell \nu_\ell) = \frac{\tau_P}{8\pi} m_P m_\ell^2 f_P^2 G_F^2 \left(1 - \frac{m_\ell^2}{m_P^2}\right)^2 \left|V_{u_j d_i} (1 + C_{V_1}^\ell - C_{V_2}^\ell)\right|^2. \quad (4.29)$$

The contributions of NP to the rate distributions or branching ratios of these decays can affect the overall normalisation or the extraction of CKM matrix elements. Specifically, the modification can be expressed as:

$$\left|V_{u_j d_i}\right| \longrightarrow \left|V_{u_j d_i} (1 + C_{V_L} \pm C_{V_R})\right|, \quad (4.30)$$

where the (+) sign applies to CKM modifications in semileptonic decays, while the (-) sign applies to leptonic decays. The CKM elements extracted from various processes of the type $P \rightarrow M \ell \nu_\ell$ can therefore serve as inputs to constrain NP parameters.

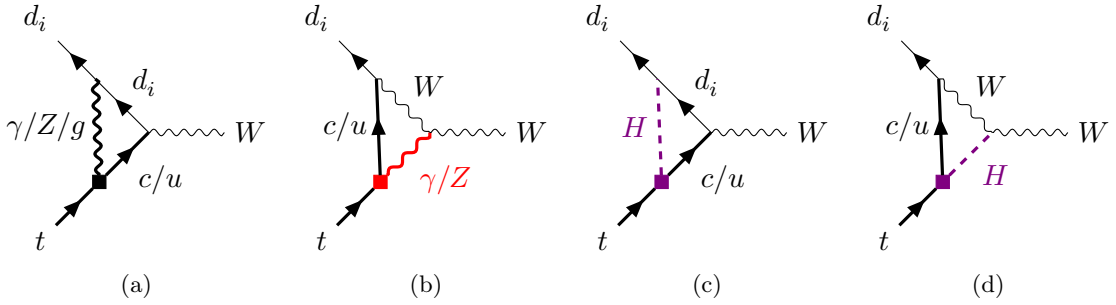


Figure 3. Effects of top FCNC operators on the $t \rightarrow W d_i$ form factor.

In the SM, CKM elements are expressed in terms of the Wolfenstein parameters: A , λ , ρ , and η , which must be determined simultaneously with the NP coefficients. Additional essential inputs include the branching fractions associated with both semileptonic and leptonic decays. A complete list of these inputs along the detailed methodology of the analysis can be found in refs. [94–96]. Along with this list, we have also included the updated results for R_D and R_{D^*} in our analysis, as reported by Belle-II [97]².

Anomalous tWb coupling: The most general Lagrangian describing the effective tWb vertex structure can be written as:

$$\mathcal{L}_{tWb} = -\frac{g_2}{\sqrt{2}} \left(\bar{b} \gamma_\mu (V_L P_L + V_R P_R) t W^{\mu-} + \bar{b} \frac{i \sigma_{\mu\nu} q^\nu}{m_W} (g_L P_L + g_R P_R) t W^{\mu-} \right) + \text{h.c.} \quad (4.31)$$

where $V_{L(R)}$, $g_{L(R)}$ are the anomalous tWb coupling, where $V_L = V_{tb}^*(1 + C_{V_L})$, $V_R = C_{V_R}$ in the SM $V_L = V_{tb}^*$ where other couplings are zero. The ATLAS Collaboration [98–100] has recently provided bounds on the quantity $|f_L V_{tb}|$, which we incorporate in our analysis by assuming the SM value $V_{tb} = 1$. Whereas the bounds on the other three anomalous couplings V_R , g_L , and g_R at 95% confidence level (CL), as provided by the combined ATLAS and CMS analyses [101], are also incorporated into our fitting procedure as additional constraints.

In the presence of effective top FCNC interaction, tWb vertex will be modified at the one-loop level as depicted in fig. 3. These diagrams will contribute to all the tWb anomalous vertex factors in eq. 4.31. We have presented all these vertex factors in terms of the top FCNC couplings in the Appendix B in eq. (B.3).

4.2 Electroweak Precision Observables

The considerable accuracy of electroweak precision measurements of the W and Z -pole observables enables us to tightly constrain NP scenarios. In our framework, NP effects manifest as corrections to the γ and Z self-energy and modifications to the $Z \rightarrow f\bar{f}$ vertex. In the following section, we investigate the impact of various top-FCNC effective operators on different oblique parameters and Z -pole observables.

²The ratio lepton flavour universality ratios are defined as $R(D^{(*)}) = \frac{\Gamma(B \rightarrow D^{(*)}\tau\nu)}{\Gamma(B \rightarrow D^{(*)}\mu\nu)}$.

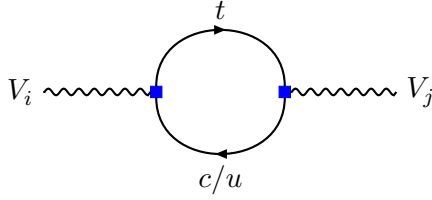


Figure 4. Gauge boson ($V_i = \gamma, Z$) self-energy correction affected due to the presence of top-FCNC processes.

Oblique Parameters: The precision extraction of the oblique parameters S , T , and U provide a model-independent framework to quantify the effects of NP on EWPOs via corrections to the vacuum polarisations (self-energies) of the electroweak gauge bosons [102–104]. These parameters are extracted by comparing precise experimental measurements, primarily from the Z -pole observables and the W boson mass, with their SM predictions. These oblique EWPOs represent a crucial phenomenological sector, offering exceptional sensitivity to the NP, particularly at future lepton colliders such as FCC-ee [105–109]. Among the three oblique parameters, T measures the difference between NP contributions to neutral and charged current interactions at low energies, making it sensitive to custodial isospin violation. Parameters S and $S+U$ capture NP effects in neutral and charged current processes across different energy scales. The parameter U is mainly constrained by the W boson mass and width. In practice, S and T typically provide stronger constraints on NP than U .

The general expression describing the renormalized one-particle irreducible (1PI) two-point functions is defined through $\Pi_{V_i V_j}(q^2)$, where the NP contributions are encoded in $\delta\Pi_{V_i V_j}(q^2)$. Here, $V_i = \gamma, W^\pm, Z$ denotes the gauge bosons involved.

$$\Pi_{V_i V_j}(q^2) = \Pi_{V_i V_j}^{\text{SM}}(q^2) + \delta\Pi_{V_i V_j}(q^2) \quad (4.32\text{a})$$

$$\left(\Pi_{V_i V_j}\right)_{\mu\nu}(q^2) = -ig_{\mu\nu} \left(q^2 - m_{V_i}^2\right) - i \left(g_{\mu\nu} - \frac{q_\mu q_\nu}{q^2}\right) \Sigma_{V_i V_j}^T(q^2) - i \frac{q_\mu q_\nu}{q^2} \Sigma_{V_i V_j}^L(q^2) \quad (4.32\text{b})$$

In our analysis, various top-quark FCNC processes induce corrections to the self-energies of the γ and Z bosons as shown in fig. 4, which lead to modifications of the oblique parameters S , T , and U . Oblique parameters (S , T , and U) originally defined by Peskin and Takeuchi [102].

$$\begin{aligned} S &= \left(\frac{4s_W^2 c_W^2}{\alpha_e}\right) \left(\left[\frac{\delta\Sigma_{ZZ}^T(m_Z^2) - \delta\Sigma_{ZZ}^T(0)}{m_Z^2} \right] - \frac{c_W^2 - s_W^2}{c_W s_W} \frac{\delta\Sigma_{\gamma Z}^T(m_Z^2)}{m_Z^2} - \frac{\delta\Sigma_{\gamma\gamma}^T(m_Z^2)}{m_Z^2} \right), \\ T &= \frac{1}{\alpha_e} \left(\frac{\delta\Sigma_{WW}^T(0)}{m_W^2} - \frac{\delta\Sigma_{ZZ}^T(0)}{m_Z^2} \right), \\ U &= \frac{4s_W^2}{\alpha_e} \left(\left[\frac{\delta\Sigma_{WW}^T(m_W^2) - \delta\Sigma_{WW}^T(0)}{m_W^2} \right] - \frac{c_W}{s_W} \frac{\delta\Sigma_{Z\gamma}^T(m_Z^2)}{m_Z^2} - \frac{\delta\Sigma_{\gamma\gamma}^T(m_Z^2)}{m_Z^2} \right) - S. \end{aligned} \quad (4.33)$$

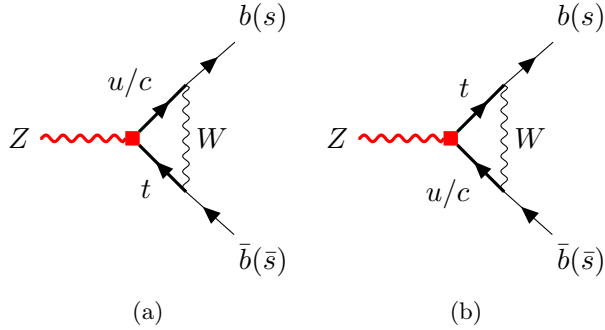


Figure 5. Feynman diagrams of $Z \rightarrow d_i \bar{d}_i$ decay, modified by the top FCNC operators.

where α_e is defined at the electro-weak scale (μ_{EW}). For our fitting procedure, we have used the global fit results provided by the Gfitter group [105], including the correlations among the oblique parameters. The self-energy expressions of the gauge bosons corresponding to fig. 4 are provided in the Appendix B in eqs. (B.4).

Z Pole Observables: The Z -pole observables are among the most precise and sensitive measurements within EWPOs. They play a crucial role in testing the SM and probing potential NP effects. In our analysis, these observables are modified by corrections to the processes $Z \rightarrow f\bar{f}$.

Among these, the decays $Z \rightarrow b\bar{b}$ and $Z \rightarrow s\bar{s}$ receive the dominant contributions, primarily from single insertions of top-quark FCNC operators, as illustrated in fig. 5. We also consider processes such as $Z \rightarrow c\bar{c}$, $Z \rightarrow \ell\bar{\ell}$, and $Z \rightarrow \nu\bar{\nu}$. These channels are affected through double insertions of NP operators, with contributions arising from diagrams involving self-energy corrections to the Z -boson, as discussed earlier (see fig. 4). However, these effects are subleading, being suppressed by $\mathcal{O}(1/\Lambda^4)$, compared to the leading $\mathcal{O}(1/\Lambda^2)$ contributions in the $Z \rightarrow b\bar{b}$ and $Z \rightarrow s\bar{s}$ channels.

The Lagrangian describing the $Z \rightarrow f\bar{f}$ interaction can be written as:

$$\mathcal{L}_{Zf\bar{f}} = \frac{g_2}{2 \cos \theta_W} \sum_f \bar{f} \gamma^\mu \left(g_{Z,v}^f - g_{Z,a}^f \gamma^5 \right) f Z_\mu, \quad (4.34)$$

The vertices can be written in terms of the NP correction as:

$$\begin{aligned} g_{Z,a}^f &\rightarrow g_{Z,a}^{f,SM} + \delta g_{Z,a}^{f,NP} \\ g_{Z,v}^f &\rightarrow g_{Z,v}^{f,SM} + \delta g_{Z,v}^{f,NP} \end{aligned} \quad (4.35)$$

where $g_{Z,a}^{f,SM}$ and $g_{Z,v}^{f,SM}$ are the axial and vector couplings of the Z boson to fermions respectively and $g_{Z,v}^{f,SM} = (I^3 - 2Q_f \sin^2 \theta)$ and $g_{Z,a}^{f,SM} = I^3$, where I^3 and Q_f represent the third component of the isospin and the charge of the fermion, respectively. The expression for NP couplings $\delta g_{Z,a}^{f,NP}$, $\delta g_{Z,v}^{f,NP}$ are mentioned in the Appendix B in eq. (B.5). The partial

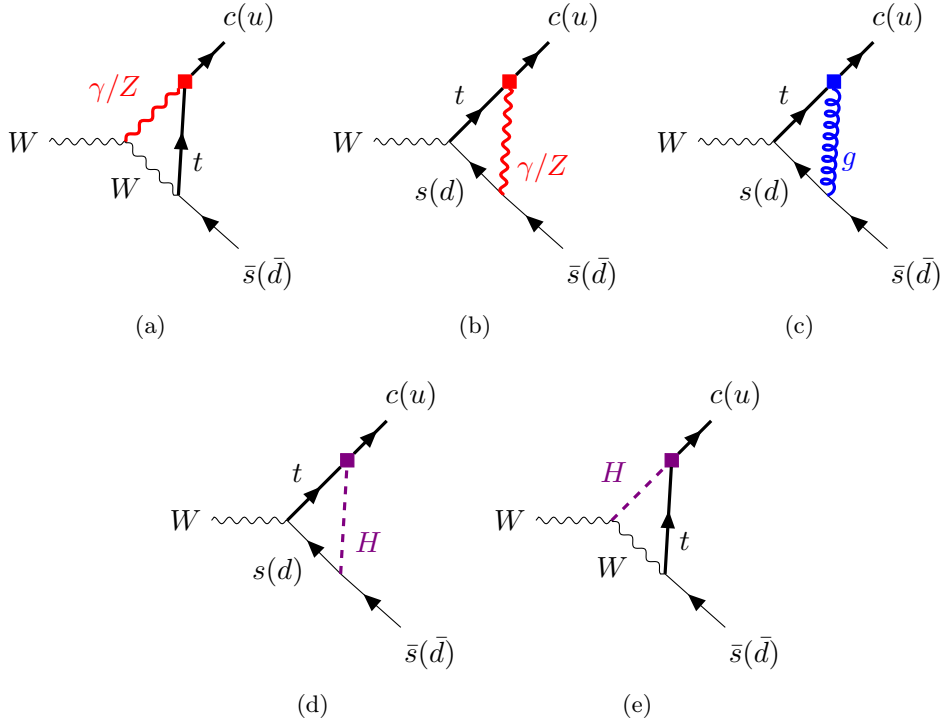


Figure 6. Feynman diagrams of $W \rightarrow u_i \bar{d}_j$ decay, modified by the top FCNC operators.

decay width of $Z \rightarrow f \bar{f}$ process can be written as:

$$\Gamma(Z \rightarrow f \bar{f}) = \frac{N_c^b}{48} \frac{\alpha}{s_W^2 c_W^2} m_Z \sqrt{1 - \mu_f^2} \left(|g_{Z,a}^f|^2 (1 - \mu_f^2) + |g_{Z,v}^f|^2 (1 + \frac{\mu_f^2}{2}) \right) (1 + \delta_f^0) (1 + \delta_b) (1 + \delta_{\text{QCD}}) (1 + \delta_{\text{QED}}) (1 + \delta_\mu^f), \quad (4.36)$$

The parameter $\mu_f^2 = \frac{4m_f^2}{m_Z^2}$ is relevant primarily for the $Z \rightarrow b \bar{b}$ decay channel. The corrections δ_f^0 , δ_b , δ_{QCD} , δ_{QED} , and δ_μ^f account for various radiative effects beyond the leading-order contribution. A detailed discussion can be found in refs. [110, 111] and the references therein. After performing the loop integration, various Z boson decay channels receive corrections, which subsequently affect various Z -pole observables. These include ratio observables, asymmetry parameters, and the total decay width of the Z boson. The corresponding values of these observables are listed in table 3. In our analysis, we have followed the methodology developed in our previous works [15, 95, 96], which simplifies the expressions for Z -pole observables in terms of the modified vector and axial-vector couplings.

W Pole Observables: In addition to the Z -pole observables, the W -pole observables are also affected in the presence of top quark FCNC operators, as shown in fig. 6. These operators induce one-loop level corrections to the $W c \bar{s}$ and $W u \bar{d}$ vertex, which lead to shifts in observables such as R_{Wc} and Γ_{hadrons} . As a result, precision measurements of W -pole observables provide complementary constraints on the NP effects in our framework. The list of observables along with their corresponding values is provided in table 4.

Observables	SM values	Experimental values	Definaton
Γ_Z (GeV)	(2.4961 ± 0.0010)	(2.4955 ± 0.0023)	$\sum_f \Gamma(Z \rightarrow f\bar{f})$
σ_{had} (nb)	(41.484)	(41.541 ± 0.037)	$\frac{12\pi}{m_Z^2} \frac{\Gamma(Z \rightarrow e^+ e^-) \Gamma(Z \rightarrow q\bar{q})}{\Gamma_Z^2}$
A_e	(0.1475 ± 0.0010)	(0.1516 ± 0.0021)	$\frac{\Gamma(Z \rightarrow e_L^+ e_L^-) - \Gamma(Z \rightarrow e_R^+ e_R^-)}{\Gamma(Z \rightarrow e^+ e^-)}$
A_μ	0.1472	0.142 ± 0.015	$\frac{\Gamma(Z \rightarrow \mu_L^+ \mu_L^-) - \Gamma(Z \rightarrow \mu_R^+ \mu_R^-)}{\Gamma(Z \rightarrow \mu^+ \mu^-)}$
A_τ	0.1472	0.143 ± 0.004	$\frac{\Gamma(Z \rightarrow \tau_L^+ \tau_L^-) - \Gamma(Z \rightarrow \tau_R^+ \tau_R^-)}{\Gamma(Z \rightarrow \tau^+ \tau^-)}$
A_b	0.935	0.923 ± 0.020	$\frac{\Gamma(Z \rightarrow b_L \bar{b}_L) - \Gamma(Z \rightarrow b_R \bar{b}_R)}{\Gamma(Z \rightarrow b\bar{b})}$
A_s	0.936	0.90 ± 0.09	$\frac{\Gamma(Z \rightarrow s_L \bar{s}_L) - \Gamma(Z \rightarrow s_R \bar{s}_R)}{\Gamma(Z \rightarrow s\bar{s})}$
A_c	0.667	0.670 ± 0.027	$\frac{\Gamma(Z \rightarrow c_L \bar{c}_L) - \Gamma(Z \rightarrow c_R \bar{c}_R)}{\Gamma(Z \rightarrow c\bar{c})}$
A_e^{FB}	$(1.606 \pm 0.006)\%$	$(1.45 \pm 0.25)\%$	$\frac{3}{4} A_e^2$
A_μ^{FB}	1.63%	$(1.69 \pm 0.13)\%$	$\frac{3}{4} A_e A_\mu$
A_τ^{FB}	1.63%	$(1.88 \pm 0.17)\%$	$\frac{3}{4} A_e A_\tau$
A_b^{FB}	$(10.34 \pm 0.07)\%$	$(9.92 \pm 0.16)\%$	$\frac{3}{4} A_e A_b$
A_s^{FB}	$(10.35 \pm 0.07)\%$	$(9.8 \pm 1.1)\%$	$\frac{3}{4} A_e A_s$
A_c^{FB}	$(7.35 \pm 0.02)\%$	$(7.07 \pm 0.35)\%$	$\frac{3}{4} A_e A_c$
R_e	20.736 ± 0.010	20.804 ± 0.050	$\frac{\Gamma(Z \rightarrow q\bar{q})}{\Gamma(Z \rightarrow e^+ e^-)}$
R_μ	20.736 ± 0.010	20.784 ± 0.034	$\frac{\Gamma(Z \rightarrow q\bar{q})}{\Gamma(Z \rightarrow \mu^+ \mu^-)}$
R_τ	20.781 ± 0.010	20.764 ± 0.045	$\frac{\Gamma(Z \rightarrow q\bar{q})}{\Gamma(Z \rightarrow \tau^+ \tau^-)}$
R_b	0.21581	(0.21629 ± 0.00066)	$\frac{\Gamma(Z \rightarrow b\bar{b})}{\sum_q \Gamma(Z \rightarrow q\bar{q})}$
R_c	0.1722	(0.1721 ± 0.0030)	$\frac{\Gamma(Z \rightarrow c\bar{c})}{\sum_q \Gamma(Z \rightarrow q\bar{q})}$

Table 3. Z Pole Observables: List of observables affected by top quark FCNC operators. All experimental and SM values are taken from refs. [76, 112–115].

Observables	SM values	Experimental values	Definaton
Γ_W (GeV)	2.088	2.085 ± 0.042 [76]	$\sum_f \Gamma(W \rightarrow f\bar{f}')$
R_{Wc}	0.50	0.49 ± 0.04 [76]	$\frac{\Gamma(W \rightarrow cs)}{\Gamma(W \rightarrow cs) + \Gamma(W \rightarrow ud)}$

Table 4. W Pole Observables: List of observables affected by top quark FCNC operators.

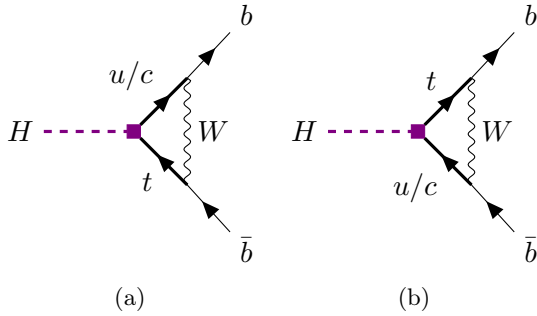


Figure 7. Modification of the $H \rightarrow b\bar{b}$ decay channel due to the presence of top FCNC operators.

4.3 Other relevant Observables

In addition to low-energy observables and EWPOs, several other processes are also sensitive to top-quark FCNC interactions. For instance, various Higgs boson decays like ($H \rightarrow b\bar{b}$, WW^* , $\gamma\gamma(Z)$) can receive one-loop level corrections from top-FCNC operators, potentially altering the decay width and coupling strength. Trilinear gauge couplings (TGC), which are tightly constrained by LEP and LHC data, can also be modified. Furthermore, these top FCNC operators can induce electric and chromomagnetic dipole and magnetic moments for various quark flavours, which could provide additional constraints on the new physics parameter space.

4.3.1 Observables related to Higgs Physics

In our analysis, we have incorporated the most recent measurements of Higgs boson production cross sections, decay branching ratios as reported by the ATLAS Collaboration [116]. Among the various Higgs decay channels, the processes $H \rightarrow b\bar{b}$ and $H \rightarrow WW^*$ receive contributions from top FCNC operators via single insertions at the one-loop level. On the other hand, the other visible-sector decays $H \rightarrow \gamma\gamma$ and $H \rightarrow \gamma Z$ and Higgs production via gluon fusion ($gg \rightarrow H$) are affected only through double insertions of top FCNC operators. In the following paragraphs we will discuss the contributions in these decays via the insertion of top-FCNC interactions.

$H \rightarrow b\bar{b}$ decay: In the presence of top FCNC interactions, the $Hb\bar{b}$ vertex receives loop-level corrections, as depicted in fig. 7. While the vertex is purely scalar in the SM, these corrections introduce deviations that modify its chiral structure. In our analysis, we incorporate these effects through modification of the chiral current.

$$\mathcal{L}_{Hb\bar{b}} = C_L^H(\bar{b}P_L b) + C_R^H(\bar{b}P_R b) \quad (4.37)$$

The modified $Hb\bar{b}$ vertex can be expressed as $C_{L(R)}^H = C_{L(R)}^{H,\text{SM}} + C_{L(R)}^{H,\text{NP}}$, where the SM contribution is given by $C_{L,R}^{H,\text{SM}} = \frac{m_b}{v}$, with v being the vacuum expectation value of the Higgs field. The expressions for the new physics (NP) contributions $C_{L,R}^{H,\text{NP}}$ are provided

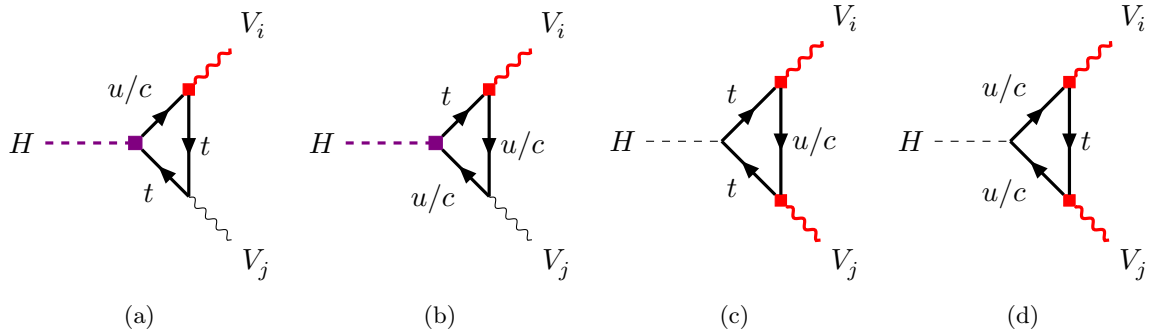


Figure 8. Feynman diagrams depicted $H \rightarrow V_i V_j$ decay channels, modified by the top FCNC operators. Here, $V_i, V_j = \gamma, Z, g$. Additionally, these diagrams correspond to the $H \rightarrow \gamma\gamma$, $H \rightarrow \gamma Z$ and $H \rightarrow gg$ decays.

in Appendix B in eqs. (B.6a)-(B.6b). The decay width can then be written in terms of the modified $Hb\bar{b}$ current as:

$$\Gamma(H \rightarrow b\bar{b}) = \frac{N_c}{16\pi m_H^2} \sqrt{m_H^2 - 2m_b^2} \left[m_H^2 \left((C_L^H)^2 + (C_R^H)^2 \right) - 2m_b^2 \left(C_L^H + C_R^H \right)^2 \right]. \quad (4.38)$$

Here, the color factor $N_c = 3$ accounts for the three possible color states of the $b\bar{b}$ pair. We take the running bottom quark mass at the Higgs mass scale, $m_b = m_b(M_H) \approx 2.7$ GeV. The experimental value of the partial decay width for the process $H \rightarrow b\bar{b}$ is given by:

$$\Gamma(H \rightarrow b\bar{b}) = (1.961 \pm 0.923) \times 10^{-3} \text{ GeV}.$$

This value is derived using the total Higgs decay width $\Gamma_H^{\text{tot}} = 3.7^{+1.9}_{-1.4}$ MeV, which corresponds to the PDG average [76], based on measurements reported by both ATLAS [117] and CMS [118, 119]. We also checked the process $H \rightarrow WW^* \rightarrow Wff'$, which is, in principle, affected by top FCNC operators at one-loop. However, due to the unitarity properties of the CKM matrix, the loop correction effectively vanishes at zero light quark mass limit.

$H \rightarrow \gamma\gamma(Z)$ decay: In the SM, the Higgs boson does not couple to photons at tree level, making the $H \rightarrow \gamma\gamma$ and $H \rightarrow \gamma Z$ decay channels rare with small branching ratios. Despite this, the diphoton channel played a crucial role in the discovery of the Higgs boson due to its clean experimental signature at colliders.

In the SM, the decays $H \rightarrow \gamma\gamma$ and $H \rightarrow \gamma Z$ are mediated by loop diagrams involving closed fermion and gauge boson loops, with the dominant contribution arising from the top quark. In our analysis, we obtain additional fermion loop contributions induced by top FCNC operators as depicted in fig. 8, which modify the amplitude beyond the SM prediction. The effective vertices can be written as

$$\delta\mathcal{L}_{h\gamma\gamma} = -\frac{\delta_{\gamma\gamma}}{2\Lambda^2} e^2 v h F_{\mu\nu} F^{\mu\nu} \quad (4.39a)$$

$$\delta\mathcal{L}_{h\gamma Z} = -\frac{\delta_{\gamma Z}}{2\Lambda^2} e^2 v h F_{\mu\nu} Z^{\mu\nu} \quad (4.39b)$$

Thus, the resulting modified decay width can be expressed as [120] :

$$\frac{\Gamma(h \rightarrow \gamma\gamma)}{\Gamma^{\text{SM}}(h \rightarrow \gamma\gamma)} \simeq \left| 1 - \frac{4\pi^2 v^2 \delta_{\gamma\gamma}}{\Lambda^2 I^{\gamma\gamma}} \right|^2 \quad (4.40\text{a})$$

$$\frac{\Gamma(h \rightarrow \gamma Z)}{\Gamma^{\text{SM}}(h \rightarrow \gamma Z)} \simeq \left| 1 - \frac{4\pi^2 v^2 \delta_{\gamma Z}}{\Lambda^2 I^{\gamma Z}} \right|^2 \quad (4.40\text{b})$$

Here, $I^{\gamma\gamma(Z)}$ denotes the Feynman parameter integrals with $I^{\gamma\gamma} \approx -1.65$ and $I^{\gamma Z} \approx -2.87$. The analytic and numerical expressions of these Feynman integrals are taken from refs. [41, 120, 121]. The new physics coupling modifiers $\delta_{\gamma\gamma(Z)}$ are provided in eqs. (B.6c)- (B.6d).

$gg \rightarrow H$: Like the $H \rightarrow \gamma\gamma(Z)$ channels, the $gg \rightarrow H$ process is another important probe, as it is loop-mediated in the SM. In the SM, the dominant contribution arises from a top-quark triangle loop. In our analysis, similar types of NP triangular loop contributions arise, as mentioned in fig. 8 (mirror symmetric). The effective Lagrangian describing the NP Higgs-gluon production channel is given by:

$$\delta\mathcal{L}_{gg h} = -\frac{\delta_{gg}}{2\Lambda^2} g_s^2 v h G_{\mu\nu}^a G^{a\mu\nu} \quad (4.41)$$

The corresponding changes in the Higgs production and decay cross sections with respect to the SM predictions can be expressed as [120]:

$$\frac{\sigma(gg \rightarrow h)}{\sigma^{\text{SM}}(gg \rightarrow h)} \simeq \frac{\Gamma(h \rightarrow gg)}{\Gamma^{\text{SM}}(h \rightarrow gg)} \simeq \left| 1 - \frac{8\pi^2 v^2 \delta_{gg}}{\Lambda^2 I^{gg}} \right|^2 \quad (4.42)$$

where $I^{gg} \approx 0.37$ [41, 120, 121] is the Feynman parameter integral arising from the $gg \rightarrow h$ loop diagrams in the SM.

In our analysis, we adopt the κ -framework to confront the new physics scenario, focusing specifically on the Higgs boson production and decay channels: $h \rightarrow \gamma\gamma$, $h \rightarrow Z\gamma$, and $h \rightarrow gg$. The general expression of a κ_i parameter is given by

$$\kappa_i^2 = \frac{\Gamma_i^{\text{Total}}}{\Gamma_i^{\text{SM}}} , \quad (4.43)$$

where Γ_i^{SM} is the partial decay width in the SM and Γ_i^{Total} is the same width including the contribution from NP. In the SM, these ratios $\kappa_i = 1$, and any observed deviation from this value would indicate the presence of physics beyond the SM. The ATLAS collaboration [116, 122] has recently reported measurements of various κ_i coupling modifiers.

$$\kappa_\gamma = (1.02^{+0.08}_{-0.07}) , \quad \kappa_{Z\gamma} = 1.38^{+0.31}_{-0.37} , \quad \kappa_g = 1.01^{+0.11}_{-0.09} . \quad (4.44)$$

We have presented the resulting expressions for δ_{gg} , for different top-FCNC operator insertions, in eq .(B.6e) in the Appendix B.

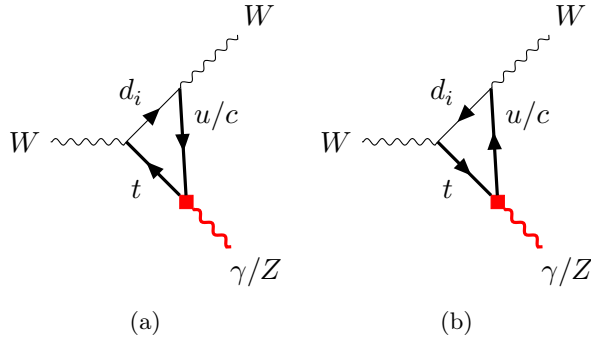


Figure 9. Feynman diagrams modifying $WW\gamma$ and WWZ gauge couplings in the presence of top-FCNC operators.

4.3.2 Trilinear Gauge Couplings

Trilinear gauge couplings (TGCs) describe the interactions among three gauge bosons, such as $WW\gamma$ and WWZ , and are a direct consequence of the non-Abelian structure of the electroweak gauge group in the SM [123–125]. Due to the high precision of TGC measurements at LEP [108], ATLAS [126–130] and CMS [131–134], particularly from diboson production channels, these observables provide stringent constraints on potential NP contributions. We include their effects in our analysis to constrain the parameter space of the relevant top FCNC effective operators. The general Lagrangian describing the triple gauge boson interactions involving W^+W^-V ($V = \gamma, Z$) can be parameterized in a Lorentz-invariant form as:

$$\begin{aligned} \mathcal{L}_{WWV} = ig_{WWV} & \left(g_1^V (W_{\mu\nu}^+ W^{-\mu} W^{+\nu} - W_{\mu}^+ W_{\nu}^- W^{\mu\nu}) + \kappa_V W_{\mu}^+ W_{\nu}^- V^{\mu\nu} \right. \\ & + \frac{\lambda_V}{M_W^2} W_{\lambda\mu}^+ W_{\nu}^{-\mu} V^{\nu\lambda} + ig_4^V W_{\mu}^+ W_{\nu}^- (\partial^{\mu} V^{\nu} + \partial^{\nu} V^{\mu}) - ig_5^V \epsilon^{\mu\nu\rho\sigma} (W_{\mu}^+ \overset{\leftrightarrow}{\partial}_{\rho} W_{\nu}^-) V_{\rho} \\ & \left. + \tilde{\kappa}_V W_{\mu}^+ W_{\nu}^- \tilde{V}^{\mu\nu} + \frac{\tilde{\lambda}_V}{M_W^2} W_{\lambda\mu}^+ W_{\nu}^{-\mu} \tilde{V}^{\nu\lambda} \right). \end{aligned} \quad (4.45)$$

Eq. (4.45) is parametrised by seven couplings. Among these, the couplings g_1^V , κ_V , and λ_V conserve both charge (C) and parity (P) individually. The coupling g_5^V violates C and P separately but preserves the combined CP symmetry. On the other hand, the couplings g_4^V , $\tilde{\kappa}_V$, and $\tilde{\lambda}_V$ explicitly violate CP and parameterise possible sources of CP violation in the bosonic sector. Among these couplings, the SM at tree level predicts $g_1^Z = g_1^{\gamma} = \kappa_Z = \kappa_{\gamma} = 1$, all the other couplings in eq. (4.45) are vanishing at tree level. The coupling g_{WWV} takes the value $-ie$ for $g_{WW\gamma}$ and $-ie \cot \theta_W$ for g_{WWZ} , respectively.

These TGCs can be further parametrised in terms of momentum-dependent form factors. A detailed discussion of this parametrisation is provided in our previous work [15], and we follow the same methodology in the present analysis. The modification in different trilinear gauge vertices will be via the one-loop diagrams shown in fig. 9. In our analysis,

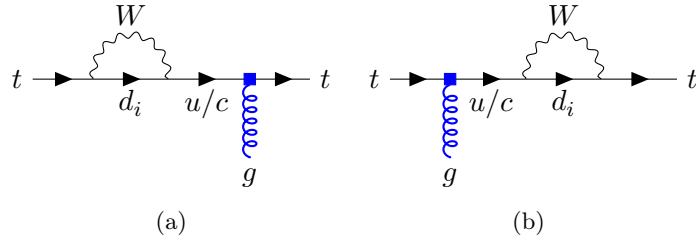


Figure 10. Magnetic dipole moment of top quarks affected by the top FCNC operators.

the following TGCs will be impacted due to top-FCNC couplings

$$g_i \in \{g_Z^1, \kappa_\gamma, \lambda_\gamma, \kappa_Z, \lambda_Z, g_Z^4, g_Z^5, \tilde{\kappa}_Z, \tilde{\lambda}_Z\} \quad (4.46)$$

The NP effects are parametrised through the shifts δg_i , such that $g_i = g_i^{\text{SM}}(1 + \delta g_i)$.

4.3.3 Top Chromo-magnetic dipole moment

In the SM, the top quark chromo-magnetic dipole moment (CMDM) arises from radiative and QCD corrections to the $t\bar{t}g$ vertex and is predicted to be small. At the scale $q^2 = m_Z^2$, its SM value is estimated to be $\hat{\mu}_t^{\text{SM}}(m_Z^2) = -0.0224$ [135], with a recent update including four-point vertex corrections yielding $\|\hat{\mu}_t^{\text{SM}}(m_Z^2)\| = -0.0253$ [136]. Experimentally, the CMS Collaboration reports $\hat{\mu}_t^{\text{Exp}}(m_Z^2) = -0.024^{+0.013}_{-0.009}{}^{+0.016}_{-0.011}$ [137], which is in good agreement with the SM prediction. This makes the CMDM a sensitive and important observable for probing and constraining NP scenarios that may modify the top-gluon interaction.

The general Lagrangian that describes the effective $t\bar{t}g$ interaction can be written as:

$$\mathcal{L}_{t\bar{t}g} = -g_s \left(\bar{t} \gamma^\mu G_\mu t + i \frac{\hat{d}_t}{2m_t} \bar{t} \sigma^{\mu\nu} \gamma_5 G_{\mu\nu}^a T^a t + \frac{\hat{\mu}_t}{2m_t} \bar{t} \sigma^{\mu\nu} G_{\mu\nu}^a T^a t \right) \quad (4.47)$$

where $G_\mu \equiv G_\mu^a T^a$, where G_μ^a are the gluon fields and $T^a = \lambda^a/2$ ($a = 1, \dots, 8$) are the generators of $\text{SU}(3)_C$. The gluon field strength tensor is defined as $G_{\mu\nu} = G_{\mu\nu}^a T^a$, where $G_{\mu\nu}^a \equiv \partial_\mu G_\nu^a - \partial_\nu G_\mu^a - g_s f^{abc} G_\mu^b G_\nu^c$, and f^{abc} are the structure constants of $\text{SU}(3)_C$. The chromo-magnetic dipole moment (CMDM) and chromo-electric dipole moments (CEDM) are defined as $\mu_t = g_s \hat{\mu}_t / m_t$ and $d_t = g_s \hat{d}_t / m_t$ respectively. In our analysis, top quark CMDM and CEDM will be impacted in the presence of NP interactions and the modifications will be via the one-loop level contributions as shown in the fig. 10. Including the NP contributions, the effective CMDM or CEDM can be written as

$$\mu_t = \frac{g_s}{m_t} \left(\hat{\mu}_t^{\text{SM}} + \hat{\mu}_t^{\text{NP}} \right), \quad (4.48)$$

$$d_t = \frac{g_s}{m_t} \left(\hat{d}_t^{\text{SM}} + \hat{d}_t^{\text{NP}} \right). \quad (4.49)$$

Here, $\hat{\mu}_t^{\text{NP}}$ and \hat{d}_t^{NP} encode the NP effects, with its analytical form given in Appendix C in eq. (C.3).

In summary, this section has outlined the complete set of observables considered in our analysis, ranging from low-energy flavour transitions to EWPOs, as well as other relevant observables from different gauge sectors. By incorporating all relevant channels within a unified framework, we ensure that potential NP effects are consistently probed across multiple energy scales. The global χ^2 fit, performed with this comprehensive dataset, allows us to extract the NP-sensitive parameters at the electroweak scale μ_{EW} . The detailed results and their phenomenological implications are presented and discussed extensively in the subsequent section.

5 Analysis and Results

In this analysis, we perform a comprehensive global analysis by incorporating a wide set of observables sensitive to top-FCNC interactions defined at the electroweak scale (μ_{EW}). The dataset includes low-energy flavour observables, EWPOs, and other relevant observables are discussed in the previous section 4 in great detail. In this section, we present the outcome of our combined analysis. The couplings (WCs) associated with different effective operators are considered to be complex. Hence, there will be contributions from both the real and imaginary parts of the couplings, both of which we have simultaneously extracted from the data. The existing low-energy and precision data are rich enough to predict a stable fit of both the real and imaginary parts of the top-FCNC parameters. This allows us to probe both CP-conserving and CP-violating components top FCNC couplings, whereas collider data are still sensitive to the real component of the WCs. We first present the results for different top-FCNC effective processes, followed by a discussion of the relevant SMEFT operators contributing to these processes. Since our primary objective is to explore the complete parameter space of the top-FCNC effective couplings, all fits are performed assuming complex couplings; as a special case, we also consider scenarios with real couplings.

In the following, we first discuss the bounds that can be derived on individual couplings using the current upper limits on the branching fractions of top-FCNC processes. These constraints are inherently limited because the branching ratio for a given decay depends on the squared modulus of the effective coupling. As a result, experimental limits on the branching fraction only constrain the overall magnitude of the coupling, not its phase. Even if both real and imaginary components are present, the observable is insensitive to their individual contributions-only the sum of their squares matters.

This limitation becomes even more severe in multi-parameter or multi-operator scenarios. When several couplings contribute simultaneously, interference terms can appear, but their effects are often absorbed into the total rate, making it impossible to disentangle individual contributions without additional observables such as angular distributions or CP-violating asymmetries. Therefore, single-parameter bounds should be interpreted as indicative rather than comprehensive, and they cannot be straightforwardly extended to scenarios involving multiple couplings or complex phases.

5.1 Constraints from collider searches

In addition to the indirect constraints derived from the observables discussed earlier, it is crucial to acknowledge the existence of direct collider bounds on the branching ratio of top-quark FCNC processes. These bounds originate from dedicated searches at the LHC, conducted by ATLAS [28–31] and CMS [32, 33], where processes such as $t \rightarrow u_j X$ ($X = g, \gamma, Z, H$) have been probed through single-top production channels as well as rare top-quark decay modes. Current experimental analyses set upper limits on the branching fractions of these FCNC processes, which can be straightforwardly translated into constraints on the corresponding top-quark FCNC WCs, as shown in eqs. (5.1a)– (5.1d). For completeness, a summary of the most recent collider bounds is presented in table 5.

Branching Ratio	SM [1]	Experimental Bound
$\mathcal{B}(t \rightarrow \gamma c)$	5×10^{-14}	4.16×10^{-5} (LH) 4.16×10^{-5} (RH) [29] 1.51×10^{-5} [32]
$\mathcal{B}(t \rightarrow \gamma u)$	4×10^{-16}	0.85×10^{-5} (LH) 1.2×10^{-5} (RH) [29] 0.95×10^{-5} [32]
$\mathcal{B}(t \rightarrow Z c)$	1×10^{-14}	1.3×10^{-4} (LH) 1.2×10^{-4} (RH) [28]
$\mathcal{B}(t \rightarrow Z u)$	7×10^{-17}	6.2×10^{-5} (LH) 6.6×10^{-5} (RH) [28]
$\mathcal{B}(t \rightarrow H c)$	3×10^{-15}	3.4×10^{-4} [30]
$\mathcal{B}(t \rightarrow H u)$	2×10^{-17}	2.8×10^{-4} [30]
$\mathcal{B}(t \rightarrow g c)$	5×10^{-12}	3.7×10^{-4} [31]
$\mathcal{B}(t \rightarrow g u)$	4×10^{-14}	6.1×10^{-5} [31]

Table 5. Summary of SM predictions and current experimental upper bounds on top-quark FCNC branching ratios.

The branching ratios of the various top-FCNC processes can be expressed in terms of the NP effective couplings as follows:

$$\mathcal{B}(t \rightarrow u_j g) = C_F \frac{m_t}{16\pi\Gamma_t} \left[\left| \xi_L^{u_j t} \right|^2 + \left| \xi_R^{u_j t} \right|^2 \right], \quad (5.1a)$$

$$\mathcal{B}(t \rightarrow u_j \gamma) = e^2 \frac{m_t}{16\pi\Gamma_t} \left[\left| \lambda_L^{u_j t} \right|^2 + \left| \lambda_R^{u_j t} \right|^2 \right], \quad (5.1b)$$

$$\begin{aligned}
\mathcal{B}(t \rightarrow u_j Z) = & \frac{g_W^2 m_t}{128\pi c_W^2 \Gamma_t} \left(1 - \frac{M_Z^2}{m_t^2}\right)^2 \left[\left(2 + \frac{m_t^2}{M_Z^2}\right) \left(|X_L^{u_j t}|^2 + |X_R^{u_j t}|^2 \right), \right. \\
& + 4 \left(2 + \frac{M_Z^2}{m_t^2}\right) \left(|\kappa_L^{u_j t}|^2 + |\kappa_R^{u_j t}|^2 \right), \\
& \left. + 6 \left(X_L^{u_j t} \kappa_R^{* u_j t} + X_L^{* u_j t} \kappa_R^{u_j t} + X_R^{u_j t} \kappa_L^{* u_j t} + X_R^{* u_j t} \kappa_L^{u_j t} \right) \right], \tag{5.1c}
\end{aligned}$$

$$\mathcal{B}(t \rightarrow u_j H) = \frac{m_t}{64\pi \Gamma_t} \left(1 - \frac{M_H^2}{m_t^2}\right)^2 \left(|\eta_L^{u_j t}|^2 + |\eta_R^{u_j t}|^2 \right). \tag{5.1d}$$

Here, Γ_t denotes the total width of the top quark, whose experimentally measured value is $\Gamma_t = 1.42^{+0.19}_{-0.15}$ GeV [76], and $C_F = 4/3$ is the colour factor. All experimental upper limits on the various top-FCNC processes, summarised in table 5, are quoted at the 95% confidence level. This allows us to estimate the maximum region of parameter space permitted for each NP coupling based on current LHC measurements. In this approach, we obtain:

$$\left[|\xi_L^{ct}|^2 + |\xi_R^{ct}|^2 \right] < 0.77 \times 10^{-4}, \quad \left[|\xi_L^{ut}|^2 + |\xi_R^{ut}|^2 \right] < 1.27 \times 10^{-5}, \tag{5.2a}$$

$$\left[|\lambda_L^{ct}|^2 + |\lambda_R^{ct}|^2 \right] < 1.75 \times 10^{-4}, \quad \left[|\lambda_L^{ut}|^2 + |\lambda_R^{ut}|^2 \right] < 4.0 \times 10^{-5}, \tag{5.2b}$$

$$\left[|X_L^{ct}|^2 + |X_R^{ct}|^2 \right] < 2.71 \times 10^{-4}, \quad \left[|X_L^{ut}|^2 + |X_R^{ut}|^2 \right] < 1.38 \times 10^{-4}, \tag{5.2c}$$

$$\left[|\kappa_L^{ct}|^2 + |\kappa_R^{ct}|^2 \right] < 1.65 \times 10^{-4}, \quad \left[|\kappa_L^{ut}|^2 + |\kappa_R^{ut}|^2 \right] < 0.84 \times 10^{-4}, \tag{5.2d}$$

$$\left[|\eta_L^{ct}|^2 + |\eta_R^{ct}|^2 \right] < 3.08 \times 10^{-3}, \quad \left[|\eta_L^{ut}|^2 + |\eta_R^{ut}|^2 \right] < 2.54 \times 10^{-3}. \tag{5.2e}$$

5.2 Constraints on top-FCNC Effective couplings from the combined analyses

In this subsection, we present the outcomes of our global fit analysis. The extracted values of the various top-FCNC effective couplings are summarised in tables 6, 7, 8, and 9. These tables respectively report the best-fit values and the corresponding allowed ranges for the top-gluon, top-photon, top- Z , and top-Higgs FCNC interactions.

Our analysis considers several benchmark scenarios:

Scenario	Values $\times 10^2$	Scenario	Values $\times 10^2$
$\text{Re}(\xi_L^{ct}), \text{Im}(\xi_L^{ct})$	$(12.3 \pm 19.7), (8.5 \pm 23.9)$	$\text{Re}(\xi_L^{ut}), \text{Im}(\xi_L^{ut})$	$(6.6 \pm 25.1), (-10.9 \pm 22.0)$
$\text{Re}(\xi_R^{ct}), \text{Im}(\xi_R^{ct})$	$(0.07 \pm 1.71), (0.09 \pm 1.60)$	$\text{Re}(\xi_R^{ut}), \text{Im}(\xi_R^{ut})$	$(-0.33 \pm 1.40), (1.57 \pm 4.55)$
$\text{Re}(\xi_L^{ct}), \text{Re}(\xi_R^{ct})$	$(13.2 \pm 16.9), (0.37 \pm 0.97)$	$\text{Re}(\xi_L^{ut}), \text{Re}(\xi_R^{ut})$	$(-8.6 \pm 23.5), (-0.38 \pm 1.29)$
$\text{Re}(\xi_L^{ct}), \text{Im}(\xi_L^{ct}), \text{Re}(\xi_R^{ct}), \text{Im}(\xi_R^{ct})$	$(-12.3 \pm 19.5), (8.2 \pm 24.4), (0.16 \pm 0.98), (0.01 \pm 1.83)$	$\text{Re}(\xi_L^{ut}), \text{Im}(\xi_L^{ut}), \text{Re}(\xi_R^{ut}), \text{Im}(\xi_R^{ut})$	$(-6.4 \pm 52.7), (-3.3 \pm 85.4), (-0.19 \pm 2.05), (-0.40 \pm 5.03)$

Table 6. Extracted values of the complex top-gluon FCNC couplings $\xi_{L,R}^{u_j t}$ ($u_j = u, c$) from the global fit only, showing real and imaginary components under different scenarios.

Scenario	Values $\times 10^2$	Scenario	Values $\times 10^2$
$\text{Re}(\lambda_L^{ct}), \text{Im}(\lambda_L^{ct})$	$(4.8 \pm 75.8), (-3.9 \pm 78.2)$	$\text{Re}(\lambda_L^{ut}), \text{Im}(\lambda_L^{ut})$	$(1.0 \pm 89.0), (-0.2 \pm 90.0)$
$\text{Re}(\lambda_R^{ct}), \text{Im}(\lambda_R^{ct})$	$(0.0 \pm 0.22), (0.0 \pm 0.21)$	$\text{Re}(\lambda_R^{ut}), \text{Im}(\lambda_R^{ut})$	$(-0.04 \pm 1.72), (0.0 \pm 1.17)$
$\text{Re}(\lambda_L^{ct}), \text{Re}(\lambda_R^{ct})$	$(1.3 \pm 90.0), (0.17 \pm 0.21)$	$\text{Re}(\lambda_L^{ut}), \text{Re}(\lambda_R^{ut})$	$(1.1 \pm 89.4), (0.30 \pm 0.87)$
$\text{Re}(\lambda_L^{ct}), \text{Im}(\lambda_L^{ct}), \text{Re}(\lambda_R^{ct}), \text{Im}(\lambda_R^{ct})$	$(-2.7 \pm 76.4), (-7.7 \pm 64.6), (0.0 \pm 0.22), (0.0 \pm 0.22)$	$\text{Re}(\lambda_L^{ut}), \text{Im}(\lambda_L^{ut}), \text{Re}(\lambda_R^{ut}), \text{Im}(\lambda_R^{ut})$	$(1.0 \pm 89.0), (0.0 \pm 90.0), (-0.05 \pm 1.71), (0.0 \pm 1.17)$

Table 7. Constraints on top-photon FCNC dipole couplings $\lambda_{L,R}^{qt}$ obtained from the global fit, showing real and imaginary components under different scenarios.

- 1. Single-Chirality Case:** Only one chiral structure (either left-handed or right-handed) is assumed to be present.
- 2. Dual-Chirality Case:** Both left- and right-handed couplings are allowed simultaneously.
- 3. Real Coupling Case:** A special case where all couplings are assumed to be real-valued.

All extracted coefficients and couplings are defined at the electroweak scale, μ_{EW} , which is the natural scale for processes involving the top quark and heavy electroweak bosons. However, for low-energy flavour observables, such as those relevant to B -meson decays, the appropriate scale is $\mu_b \sim m_b$. A consistent analysis requires translating the high-scale couplings to the low-energy scale or vice-versa by using the RGE framework discussed earlier. This procedure ensures that predictions for low-energy observables, such as branching ratios of rare B decays or meson mixing parameters, are computed using WCs evaluated at the correct scale. Without this step, one would risk introducing large theoretical uncertainties or inconsistencies between different sectors of the analysis. In summary, the connection between μ_{EW} and μ_b through RGE evolution is essential for maintaining theoretical consistency and for combining collider constraints with flavor physics data in a global fit.

Scenario	Values $\times 10$	Scenario	Values $\times 10$
$\text{Re}(\kappa_L^{ct}), \text{Im}(\kappa_L^{ct})$	$(-0.20 \pm 2.38), (-1.92 \pm 2.84)$	$\text{Re}(\kappa_L^{ut}), \text{Im}(\kappa_L^{ut})$	$(0.29 \pm 5.05), (-2.89 \pm 2.12)$
$\text{Re}(\kappa_R^{ct}), \text{Im}(\kappa_R^{ct})$	$(0.16 \pm 0.41), (2.75 \pm 2.04)$	$\text{Re}(\kappa_R^{ut}), \text{Im}(\kappa_R^{ut})$	$(0.89 \pm 2.03), (2.04 \pm 2.13)$
$\text{Re}(\kappa_L^{ct}), \text{Re}(\kappa_R^{ct})$	$(-0.29 \pm 2.92), (0.03 \pm 0.36)$	$\text{Re}(\kappa_L^{ut}), \text{Re}(\kappa_R^{ut})$	$(0.29 \pm 0.99), (-0.04 \pm 0.15)$
$\text{Re}(X_L^{ct}), \text{Re}(X_R^{ct})$	$(-0.13 \pm 0.39), (3.1 \pm 3.52)$	$\text{Re}(X_L^{ut}), \text{Re}(X_R^{ut})$	$(0.10 \pm 0.27), (-0.92 \pm 2.63)$
$\text{Re}(\kappa_L^{ct}), \text{Im}(\kappa_L^{ct}),$ $\text{Re}(\kappa_R^{ct}), \text{Im}(\kappa_R^{ct})$.	$(-1.44 \pm 4.12), (1.40 \pm 4.16),$ $(2.64 \pm 6.90), (-4.59 \pm 4.49)$	$\text{Re}(\kappa_L^{ut}), \text{Im}(\kappa_L^{ut}),$ $\text{Re}(\kappa_R^{ut}), \text{Im}(\kappa_R^{ut})$.	$(-2.31 \pm 2.15), (0.77 \pm 2.93),$ $(1.16 \pm 0.51), (-2.75 \pm 0.49)$

Table 8. Fitted values of complex top– Z boson dipole couplings ($\kappa_{L,R}^{u_j t}$) and vector couplings ($X_{L,R}^{u_j t}$) from the global fit, showing real and imaginary components under different scenarios.

The most stringent constraints on the top-gluon FCNC couplings arise primarily from the radiative B -meson decay, where the mixing of the gluon dipole operators (O_8) into the photon dipole operators (O_7) plays a crucial role in enhancing the sensitivity. In addition to these effects, contributions from δ_{gg} (the modified Higgs-gluon coupling) and anomalous Wtb interactions also provide important complementary constraints.

On the other hand, the strongest constraints on the top-photon FCNC couplings originate from the direct contributions of the photon dipole operators to the radiative decay $B \rightarrow X_s \gamma$, as well as to other exclusive radiative decay channels. Additional sensitivity arises from $\delta_{\gamma\gamma(Z)}$, which parameterises the modified Higgs–photon(Z)-boson couplings.

For the various top- Z FCNC effective couplings, rare B -meson decays play a particularly important role in constraining the vector-type interactions. In contrast, the tensor-type couplings receive their strongest bounds from $\delta_{\gamma Z}$, as well as from several FCCC observables and Z -pole observables.

It is evident from the tables 6, 7, 8, and 9 that the most tightly constrained coupling is the right-chiral tensor coupling λ_R^{ct} , which is bounded at the order of $\mathcal{O}(10^{-3})$. In comparison, other right-handed dipole couplings associated with the top-photon interaction, λ_R^{ut} , and the top–gluon interactions, $\xi_R^{u_j t}$ ($u_j = u, c$), are constrained at the order of $\mathcal{O}(10^{-2})$. The left-chiral dipole couplings in both the top-gluon and top-photon sectors, as well as the left- and right-chiral tensor and vector couplings of the top- Z interaction, $(\kappa_{L,R}^{u_j t}, X_{L,R}^{u_j t})$, are comparatively less sensitive by the current experimental data, typically lying in the range of $\mathcal{O}(10^{-1})$.

As shown in table 9, the top-Higgs FCNC couplings are only weakly constrained by the observables included in the global fit. In addition, we consider several observables for which only experimental upper limits are currently available. Although such measurements cannot be incorporated directly into the global fit, they provide significantly stronger constraints on specific combinations of the $t\bar{c}H$ and $t\bar{u}H$ couplings. Consequently, their impact is not reflected in the fit results presented here. The constraints derived from these observables on the relevant product couplings will be discussed separately in a later section.

Scenario	Values	Scenario	Values
$\text{Re}(\eta_L^{ct}), \text{Im}(\eta_L^{ct})$	$(-1.05 \pm 12.96), (1.1 \pm 288.9)$	$\text{Re}(\eta_L^{ut}), \text{Im}(\eta_L^{ut})$	$(0.13 \pm 5.01), (0.46 \pm 63.17)$
$\text{Re}(\eta_R^{ct}), \text{Im}(\eta_R^{ct})$	$(0.37 \pm 1.71), (3.09 \pm 7.57)$	$\text{Re}(\eta_R^{ut}), \text{Im}(\eta_R^{ut})$	$(-0.02 \pm 0.07), (0.02 \pm 1.63)$
$\text{Re}(\eta_L^{ct}), \text{Re}(\eta_R^{ct})$	$(-1.05 \pm 12.95), (0.01 \pm 0.17)$	$\text{Re}(\eta_L^{ut}), \text{Re}(\eta_R^{ut})$	$(1.49 \pm 5.27), (-0.02 \pm 0.07)$
$\text{Re}(\eta_L^{ct}), \text{Im}(\eta_L^{ct}), \text{Re}(\xi_L^{ct}), \text{Im}(\xi_L^{ct})$	$(-0.95 \pm 16.92), (0.96 \pm 46.78), (-0.04 \pm 0.76), (0.06 \pm 0.53)$	$\text{Re}(\eta_R^{ct}), \text{Im}(\eta_R^{ct}), \text{Re}(\xi_R^{ct}), \text{Im}(\xi_R^{ct})$	$(0.38 \pm 1.59), (3.10 \pm 6.98), (-0.001 \pm 0.011), (0.0 \pm 0.0267)$
$\text{Re}(\eta_L^{ut}), \text{Im}(\eta_L^{ut}), \text{Re}(\xi_L^{ut}), \text{Im}(\xi_L^{ut})$	$(0.02 \pm 5.56), (-0.89 \pm 9.36), (0.10 \pm 0.27), (-0.10 \pm 0.23)$	$\text{Re}(\eta_R^{ut}), \text{Im}(\eta_R^{ut}), \text{Re}(\xi_R^{ut}), \text{Im}(\xi_R^{ut})$	$(0.06 \pm 0.97), (0.01 \pm 1.62), (0.003 \pm 0.16), (0.09 \pm 0.07)$

Table 9. Global fit constraints on top-Higgs FCNC couplings $\eta_{L,R}^{qt}$ under various scenarios.

In the above tables, we also present the fitted values of the top-FCNC effective couplings in the multi-operator scenarios involving different complex Wilson coefficients. In most cases, the allowed ranges of the couplings become noticeably more relaxed, a consequence of the enlarged parameter space and the correlations among multiple operators. Nevertheless, despite the increased dimensionality of the fit, we obtain stable and well-converged minima, due to the large number of observables included in our global analysis. For the multi-parameter fit in the top-Higgs sector, we also examined scenarios that include operators from different top-FCNC sectors, such as the simultaneous presence of top-Higgs and top-gluon couplings. In these cases, the constraints on the top-Higgs interactions become significantly stronger, primarily due to the sensitivity of the modified gluon-Higgs interactions. The coupling δ_{gg} plays a crucial role in tightening the allowed parameter space. In the multi-parameter analysis, it is essential to examine the correlations among the fitted parameters, as these correlations strongly influence the allowed ranges and the stability of the fit. For this reason, we explicitly report the correlation matrices for each scenario in the tables presented in Appendix D.

In summary, across all operator categories, several characteristic features are common. Most notably, the bounds on imaginary components are comparable with the respective real parts. The data used are sufficiently sensitive to the complex couplings which demonstrates that apart from the collider searches the current data support a stable and competitive global fit in the full complex parameter space. Furthermore, the right-handed components of the dipole (tensor) operators are more tightly constrained than the corresponding left-handed couplings. This difference is due to the different CKM suppressions and mass insertions entering the underlying low-energy and other relevant observables. A similar trend is observed in the scalar sector, where the right-chiral scalar couplings also exhibit tighter bounds compared to their left-chiral counterparts.

Previously, we noted that measurements of the branching fractions of top-FCNC decays primarily constrain a single coupling at a time. Consequently, they do not allow simultaneous bounds on both left- and right-handed couplings, nor on the real and imaginary components of the same coupling. Our analysis demonstrates that these limitations can be overcome by incorporating additional datasets where the effective top-FCNC couplings also

contribute. This broader approach enables us to extract complementary information that is inaccessible through branching fraction measurements alone. Therefore, a direct comparison between our bounds and those derived solely from collider branching fraction data is not strictly meaningful. Nevertheless, it is noteworthy that our bounds in tables 6, 7, 8, and 9 are generally comparable to those obtained from top-FCNC branching fractions (see eq. (5.2)), and in specific scenarios, such as for λ_R^{ct} , our constraints are even more stringent. Since all fitted NP couplings remain consistent with zero within 1σ uncertainties, the limits obtained from the LHC lie entirely within the parameter space allowed by our global fit.

5.2.1 SMEFT Correspondence

In this subsubsection, we summarise in table 10 the values of the SMEFT WCs which are connected to the top-FCNC effective couplings via the relations given in eq. 2.6. This mapping provides a direct connection between the experimental constraints expressed in the effective basis (2.1) and the SMEFT WCs. We have obtained these constraints directly using the bounds on the top-FCNC couplings from our global analysis discussed in the previous subsection. As previously mentioned, all NP effective couplings in our analysis are treated as complex, and this property is carried over to the corresponding SMEFT coefficients. In table 11, we also present the results for the real coupling scenarios and report the values of the SMEFT coefficients at different NP scales Λ .

Complex SMEFT Couplings (μ_{EW})			
Scenarios	Value ($10^7 \times \text{GeV}^{-2}$)	Scenarios	Value ($10^7 \times \text{GeV}^{-2}$)
$\text{Re}(\mathcal{C}_{23}^{uG}), \text{Im}(\mathcal{C}_{23}^{uG})$	$(0.23 \pm 6.51), (0.73 \pm 3.0)$	$\text{Re}(\mathcal{C}_{13}^{uG}), \text{Im}(\mathcal{C}_{13}^{uG})$	$(-0.70 \pm 2.90), (3.27 \pm 9.45)$
$\text{Re}(\mathcal{C}_{23}^{uB}), \text{Im}(\mathcal{C}_{23}^{uB})$	$(0.0 \pm 0.17), (0.0 \pm 0.29)$	$\text{Re}(\mathcal{C}_{13}^{uB}), \text{Im}(\mathcal{C}_{13}^{uB})$	$(0.03 \pm 0.54), (0.0 \pm 0.86)$
$\text{Re}(\mathcal{C}_{23}^{uW}), \text{Im}(\mathcal{C}_{23}^{uW})$	$(0.0 \pm 0.60), (0.01 \pm 0.30)$	$\text{Re}(\mathcal{C}_{13}^{uW}), \text{Im}(\mathcal{C}_{13}^{uW})$	$(-0.14 \pm 0.87), (0.0 \pm 1.14)$
$\text{Re}(\mathcal{C}_{23}^{u\phi}), \text{Im}(\mathcal{C}_{23}^{u\phi})$	$(1.54 \pm 18.94), (0.01 \pm 568)$	$\text{Re}(\mathcal{C}_{13}^{u\phi}), \text{Im}(\mathcal{C}_{13}^{u\phi})$	$(-5.84 \pm 8.48), (-11.2 \pm 38.4)$
$\text{Re}(\mathcal{C}_{23}^{uB}), \text{Re}(\mathcal{C}_{23}^{uW})$	$(-0.22 \pm 2.20), (0.32 \pm 4.00)$	$\text{Re}(\mathcal{C}_{13}^{uB}), \text{Re}(\mathcal{C}_{13}^{uW})$	$(-0.12 \pm 1.00), (-0.55 \pm 1.62)$

Table 10. Fit results for top-quark FCNC processes. The SMEFT WCs are treated as complex, with the shorthand notation \mathcal{C} denoting \mathcal{C}/Λ^2 . All coefficients are evaluated at the electroweak scale μ_{EW} .

Table 10 shows that the most strongly constrained SMEFT coefficients are the top-dipole couplings ($\mathcal{C}_{23}^{uB}, \mathcal{C}_{23}^{uW}$), which are bounded at the level of $\mathcal{O}(10^{-8})$. The chromomagnetic operator \mathcal{C}_{23}^{uG} is slightly less constrained, at $\mathcal{O}(10^{-7})$, while the top-Higgs couplings ($\mathcal{C}^{\phi u}, \mathcal{C}^{u\phi}$) remain comparatively weakly constrained, with bounds in the range $\mathcal{O}(10^{-5}\text{--}10^{-6})$. The bounds on the imaginary components of the WCs are comparable with the respective real components. A similar pattern is observed for the top-up SMEFT FCNC coefficients,

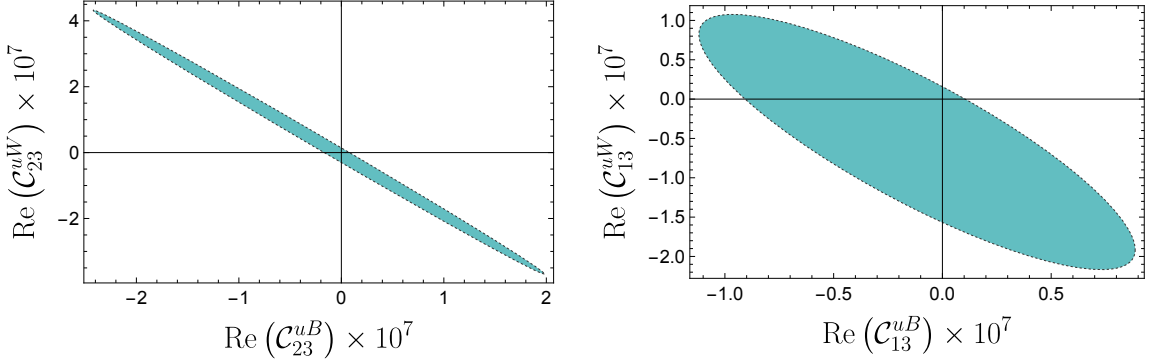


Figure 11. Correlations among the SMEFT WCs contributing to the top FCNC processes $t \rightarrow u_j \gamma(Z)$ are shown. The pastel blue ellipse represents 1σ errors. SMEFT WCs are defined at the reference scale μ_{EW} .

although, in most cases, the top-up couplings are less constrained than their top-charm counterparts.

The operators $\mathcal{O}_{pr}^{\phi q(1)}$ and $\mathcal{O}_{pr}^{\phi q(3)}$, which involve the $SU(2)_L$ doublet q_L , induce both up- and down-type FCNC interactions. Since they contribute at tree level to down-type FCNC processes like $b \rightarrow s(d)\gamma$ or $b \rightarrow s(d)\ell\ell$ decays, the corresponding bounds can be extremely restrictive, reaching the level of $\mathcal{O}(10^{-10})$,

$$\mathcal{C}_{32}^{\phi q(-)}(\mu_{\text{EW}}) = (-0.58 \pm 2.02) \times 10^{-10}, \quad \mathcal{C}_{31}^{\phi q(-)}(\mu_{\text{EW}}) = (0.27 \pm 4.95) \times 10^{-10}. \quad (5.3)$$

However, if these coefficients were extracted by considering only up-type FCNC couplings, their values would be

$$\mathcal{C}_{32}^{\phi q(-)}(\mu_{\text{EW}}) = (-2.20 \pm 6.46) \times 10^{-7}, \quad \mathcal{C}_{31}^{\phi q(-)}(\mu_{\text{EW}}) = (1.70 \pm 4.45) \times 10^{-7}. \quad (5.4)$$

The bounds are derived from their one-loop level contributions to various observables, such as the decays $b \rightarrow s(d)\gamma$ and $b \rightarrow s(d)\ell\ell$. As discussed earlier, certain NP models can affect top-quark FCNC interactions and down-type FCNC interactions in different ways. These different types of interactions may influence distinct sets of observables, and even when they impact the same observables, their contributions can vary significantly, as illustrated in the example above. Therefore, it is crucial to determine independent constraints on the couplings associated with top-quark and down-type FCNC interactions.

It is worth noting that in our analysis, the coefficients $\mathcal{C}^{\phi q(1)}$ and $\mathcal{C}^{\phi q(3)}$ always appear in the specific combination $\mathcal{C}^{\phi q(1)} - \mathcal{C}^{\phi q(3)}$. As a result, it is not possible to disentangle them individually from the fit. Therefore, in eq. (5.3) we extract their values through the combination $\mathcal{C}^{\phi q(-)} \equiv \mathcal{C}^{\phi q(1)} - \mathcal{C}^{\phi q(3)}$.

Unlike the vector combination $\mathcal{C}^{\phi q(-)}$, the two dipole operators \mathcal{C}^{uB} and \mathcal{C}^{uW} appear in the $tu_j\gamma$ and tu_jZ vertices in specific linear combinations as shown in eq. (2.6). As a consequence, these coefficients exhibit a strong negative correlation when they are fitted simultaneously, as shown in fig. 11. The corresponding multiparameter fit results are presented in the last row of table 10. The simultaneous fit yields a noticeably more relaxed

parameter space compared to the individual parameter fits, reflecting the strong interplay between these two dipole couplings. It is worth noting that we present only the real-parameter fit for this operator pair; in the complex scenario, the number of free parameters increases and the strong correlations between them prevent the fit from converging to a stable minimum.

Real-Parameter Scenario					
Coupling (GeV ⁻²)	μ_b	μ_t	$\mu = 1$ TeV	$\mu = 5$ TeV	$\mu = 10$ TeV
$\mathcal{C}_{23}^{uG} \times 10^7$	(-0.76 ± 2.29)	(-0.66 ± 1.97)	(-0.63 ± 1.88)	(-0.61 ± 1.82)	(-0.60 ± 1.80)
$\mathcal{C}_{23}^{uB} \times 10^8$	(0.23 ± 0.20)	(-0.10 ± 1.45)	(-0.24 ± 1.97)	(-0.37 ± 2.42)	(-0.42 ± 2.62)
$\mathcal{C}_{23}^{uW} \times 10^8$	(-0.35 ± 0.91)	(-0.88 ± 2.48)	(-1.09 ± 3.10)	(-1.27 ± 3.63)	(-1.35 ± 3.85)
$\mathcal{C}_{23}^{\phi q(1)} \times 10^{10}$	(-0.43 ± 1.86)	(-0.61 ± 2.05)	(-0.68 ± 2.11)	(-0.74 ± 2.17)	(-0.77 ± 2.19)
$\mathcal{C}_{23}^{\phi q(3)} \times 10^{10}$	(-0.27 ± 1.87)	(0.59 ± 2.05)	(0.62 ± 2.09)	(0.65 ± 2.12)	(0.66 ± 2.13)
$\mathcal{C}_{23}^{\phi u} \times 10^6$	(0.59 ± 7.16)	(0.79 ± 9.32)	(0.85 ± 10.2)	(0.92 ± 10.97)	(0.94 ± 11.29)
$\mathcal{C}_{23}^{u\phi} \times 10^6$	(0.12 ± 1.78)	(0.18 ± 1.91)	(0.19 ± 1.91)	(0.20 ± 1.90)	(0.20 ± 1.89)
$\mathcal{C}_{13}^{uG} \times 10^7$	(-1.16 ± 2.97)	(-1.00 ± 2.63)	(-0.96 ± 2.55)	(-0.93 ± 2.50)	(-0.91 ± 2.48)
$\mathcal{C}_{13}^{uB} \times 10^8$	(0.35 ± 3.31)	(-0.15 ± 5.79)	(-0.36 ± 6.82)	(-0.55 ± 7.72)	(-0.63 ± 8.09)
$\mathcal{C}_{13}^{uW} \times 10^7$	(-0.06 ± 0.59)	(-0.15 ± 0.92)	(-0.18 ± 1.05)	(-0.21 ± 1.17)	(-0.22 ± 1.21)
$\mathcal{C}_{13}^{\phi q(1)} \times 10^{10}$	(0.20 ± 4.57)	(0.28 ± 5.02)	(0.32 ± 5.18)	(0.34 ± 5.32)	(0.36 ± 5.37)
$\mathcal{C}_{13}^{\phi q(3)} \times 10^{10}$	(-0.23 ± 4.59)	(-0.28 ± 5.00)	(-0.29 ± 5.12)	(-0.50 ± 5.20)	(-0.31 ± 5.23)
$\mathcal{C}_{13}^{\phi u} \times 10^6$	(-1.19 ± 3.45)	(-1.56 ± 4.49)	(-1.70 ± 4.92)	(-1.83 ± 5.29)	(-1.88 ± 5.44)
$\mathcal{C}_{13}^{u\phi} \times 10^7$	(-3.17 ± 8.29)	(-2.97 ± 7.70)	(-2.86 ± 7.40)	(-2.76 ± 7.10)	(-2.71 ± 6.97)

Table 11. Fit results for the top-FCNC SMEFT WCs in the real-coupling scenario. The scale dependence of the coefficients is shown for different values of the NP scale (Λ).

Scale dependency of the couplings: Table 11 presents the results for the SMEFT WCs in the real-coupling scenarios. We display these results separately because several of the observables discussed earlier are particularly sensitive to the imaginary parts of the NP couplings. To isolate the effects free from CP-violating contamination, we therefore examine this special case in which all couplings are taken to be real. The table also shows the renormalisation-group running of these coefficients for different choices of the NP scale Λ . As mentioned earlier, to perform the RGE of the SMEFT WCs, we use the ADMs derived in refs. [41, 42, 45]. The evolution is obtained by solving the full set of seven coupled differential equations, with initial conditions given by the values of the SMEFT coefficients at the matching scale (μ_{EW}). The details of the ADMs, together with the corresponding initial conditions of SM input parameters, are provided in Appendix A. It is worth mentioning that, for running the WCs, $\mathcal{C}^{\phi q(1)}$ and $\mathcal{C}^{\phi q(3)}$, we assign identical initial conditions as mentioned in eq. (5.3) to both coefficients but with a relative minus sign. This choice is

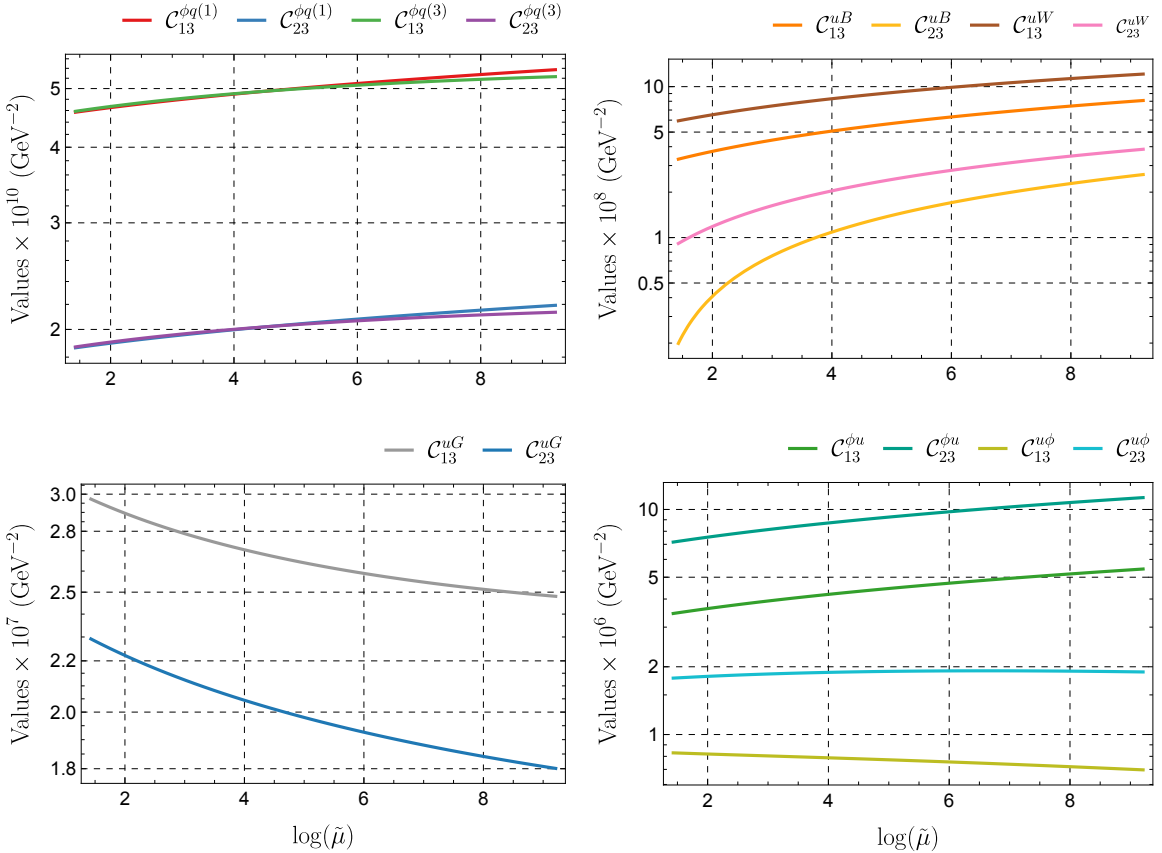


Figure 12. Evolution of the SMEFT couplings (\mathcal{C}_i/Λ^2) over the energy range up to 10 TeV. We use the shorthand notation ($\mathcal{C}_i \equiv \mathcal{C}_i/\Lambda^2$) throughout. The quantity $\tilde{\mu}$ denotes the normalised energy scale, defined as $\tilde{\mu} = \mu/1 \text{ GeV}$.

justified in the single-parameter scenarios (only one parameter is present at a time), since these operators always appear in a specific combination hard to disentangle from the fit. In fig. 12, we show the extrapolated evolution of the SMEFT couplings over the energy range from the scale μ_b up to the NP scale of 10 TeV. We observe that the coefficients \mathcal{C}^{uG} and $\mathcal{C}^{u\phi}$ decrease as the scale μ is increased, indicating that their running is dominated by the strong coupling g_s . In contrast, the remaining coefficients \mathcal{C}^{uB} , \mathcal{C}^{uW} , $\mathcal{C}^{\phi q(1)}$, $\mathcal{C}^{\phi q(3)}$, and $\mathcal{C}^{\phi u}$ grow with increasing energy scale, reflecting their ADM structure and the dominance of electroweak contributions in their evolution. As evident from fig. 12, the WCs \mathcal{C}^{uB} and \mathcal{C}^{uW} exhibit a substantial change as they evolve from the scale μ_b up to $\mu_\Lambda = 10 \text{ TeV}$.

Impact of LHC searches on the allowed SMEFT parameter space: We have already seen in subsection 5.1 that different collider searches may also impose constraints on the top-FCNC effective couplings (only one independent coupling at a time), we now translate those bounds into the corresponding SMEFT WCs. This allows us to assess the impact of collider limits directly in the SMEFT WC and to compare them with the regions

favoured by our global fit. Following are the bounds on the SMEFT WCs from the collider searches on top FCNC decays [29–31]

$$\left| \mathcal{C}_{13}^{uG} \right| < 0.57 \times 10^{-7}, \quad \left| \mathcal{C}_{23}^{uG} \right| < 1.4 \times 10^{-7}, \quad (5.5a)$$

$$\left| \mathcal{C}_{13}^{uW} + \mathcal{C}_{13}^{uB} \right| < 0.123 \times 10^{-6}, \quad \left| \mathcal{C}_{23}^{uW} + \mathcal{C}_{23}^{uB} \right| < 0.235 \times 10^{-6}, \quad (5.5b)$$

$$\left| (\mathcal{C}_{31}^{uW})^* + (\mathcal{C}_{31}^{uB})^* \right| < 0.103 \times 10^{-6}, \quad \left| (\mathcal{C}_{32}^{uW})^* + (\mathcal{C}_{32}^{uB})^* \right| < 0.227 \times 10^{-6}, \quad (5.5c)$$

$$\left| \mathcal{C}_{13}^{u\phi} \right| < 0.68 \times 10^{-6}, \quad \left| \mathcal{C}_{23}^{u\phi} \right| < 0.78 \times 10^{-6}, \quad (5.5d)$$

Due to the limitations we have mentioned earlier, we can constrain only one WC taken at a time from the collider data. In refs. [30, 31], the bounds on \mathcal{C}_{13}^{uG} , \mathcal{C}_{23}^{uG} , $\mathcal{C}_{13}^{u\phi}$ and $\mathcal{C}_{23}^{u\phi}$ are obtained considering only right-handed vector quark currents, contributions from the left-handed vector quark currents have been neglected. In ref. [29], both the left- and right-handed quark currents have been considered, and one can obtain bounds on the combinations of the \mathcal{C}_{ij}^{uW} and \mathcal{C}_{ij}^{uB} , respectively, not on a single WC.

The bounds mentioned in the above equations can be compared with those obtained in table 11. The coefficients, such as \mathcal{C}_{13}^{uW} , \mathcal{C}_{23}^{uW} , $\mathcal{C}_{23}^{\phi q(-)}$, and $\mathcal{C}_{13}^{\phi q(-)}$ are more strongly constrained by our global analysis, reflecting the sensitivity of low energy flavour observables to these particular operator structures. It is worth mentioning that the parameter space of \mathcal{C}_{3i} is substantially overestimated in the global fit; therefore, we do not present their fitted values in the main text. For completeness, the corresponding fit results are provided in Appendix E.

5.3 Predictions for branching ratios

In the previous subsections 5.2 and 5.2.1, we presented the bounds on various top effective couplings and their corresponding SMEFT WCs, obtained collectively from low-energy flavour observables, EWPOs, and other relevant measurements. Using these bounds we predict the branching fractions of various top-FCNC decays, which we have in table 12, which can be compared with the current experimental upper limits and the respective SM predictions shown in table 5. It is evident that the predicted branching ratios for top-FCNC processes in the SM are extremely small, ranging from $\mathcal{O}(10^{-12})$ to $\mathcal{O}(10^{-17})$, and thus remain far below the current experimental sensitivities.

In table 12, we have presented the top-FCNC branching fractions only for the scenarios in which our bounds are allowed by the current experimental limits. Hence, we restrict ourselves to the SMEFT operators that generate right-handed tensor and scalar FCNC interactions, as well as a few left-handed vector operators. Our global fit comparatively weakly constrains the remaining SMEFT operators, and the collider bounds can further constrain their unconstrained parameter space.

For the dipole-induced processes $t \rightarrow c\gamma$ and $t \rightarrow u\gamma$, we find a significant improvement relative to the current experimental limits; our prediction lies approximately two orders of

Process	Scenario	Our prediction	Process	Scenario	Our prediction
$\mathcal{B}(t \rightarrow cg)$	$\text{Re } \mathcal{C}_{23}^{uG} \neq 0$	$(0.06 \pm 3.48) \times 10^{-4}$	$\mathcal{B}(t \rightarrow ug)$	$\text{Re } \mathcal{C}_{13}^{uG} \neq 0$	$(0.57 \pm 4.72) \times 10^{-4}$
	$\text{Re } \mathcal{C}_{23}^{uG}, \text{Im } \mathcal{C}_{23}^{uG} \neq 0$	$(0.69 \pm 3.75) \times 10^{-4}$		$\text{Re } \mathcal{C}_{13}^{uG}, \text{Im } \mathcal{C}_{13}^{uG} \neq 0$	$(1.29 \pm 7.06) \times 10^{-3}$
$\mathcal{B}(t \rightarrow c\gamma)$	$\text{Re } \mathcal{C}_{23}^{uB}, \text{Re } \mathcal{C}_{23}^{uW} \neq 0$	$(0.13 \pm 0.70) \times 10^{-6}$	$\mathcal{B}(t \rightarrow u\gamma)$	$\text{Re } \mathcal{C}_{13}^{uB}, \text{Re } \mathcal{C}_{13}^{uW} \neq 0$	$(1.09 \pm 2.85) \times 10^{-5}$
	$\text{Re } \mathcal{C}_{23}^{uB}, \text{Im } \mathcal{C}_{23}^{uB} \neq 0$	$(0.01 \pm 0.97) \times 10^{-7}$		$\text{Re } \mathcal{C}_{13}^{uB}, \text{Im } \mathcal{C}_{13}^{uB} \neq 0$	$(0.06 \pm 2.07) \times 10^{-6}$
	$\text{Re } \mathcal{C}_{23}^{uW}, \text{Im } \mathcal{C}_{23}^{uW} \neq 0$	$(0.01 \pm 0.77) \times 10^{-7}$		$\text{Re } \mathcal{C}_{13}^{uW}, \text{Im } \mathcal{C}_{13}^{uW} \neq 0$	$(0.37 \pm 4.52) \times 10^{-6}$
$\mathcal{B}(t \rightarrow cZ)$	$\text{Re } \mathcal{C}_{23}^{uB}, \text{Re } \mathcal{C}_{23}^{uW} \neq 0$	$(0.07 \pm 1.58) \times 10^{-4}$	$\mathcal{B}(t \rightarrow uZ)$	$\text{Re } \mathcal{C}_{13}^{uB}, \text{Re } \mathcal{C}_{13}^{uW} \neq 0$	$(0.08 \pm 0.69) \times 10^{-4}$
	$\text{Re } \mathcal{C}_{23}^{uB}, \text{Im } \mathcal{C}_{23}^{uB} \neq 0$	$(0.02 \pm 1.68) \times 10^{-8}$		$\text{Re } \mathcal{C}_{13}^{uB}, \text{Im } \mathcal{C}_{13}^{uB} \neq 0$	$(0.11 \pm 3.58) \times 10^{-7}$
	$\text{Re } \mathcal{C}_{23}^{uW}, \text{Im } \mathcal{C}_{23}^{uW} \neq 0$	$(0.02 \pm 1.48) \times 10^{-7}$		$\text{Re } \mathcal{C}_{13}^{uW}, \text{Im } \mathcal{C}_{13}^{uW} \neq 0$	$(0.07 \pm 0.86) \times 10^{-5}$
	$\text{Re } \mathcal{C}_{23}^{\phi q(-)} \neq 0$	$(0.56 \pm 3.86) \times 10^{-11}$		$\text{Re } \mathcal{C}_{13}^{\phi q(-)} \neq 0$	$(0.12 \pm 4.31) \times 10^{-11}$
$\mathcal{B}(t \rightarrow cH)$	$\text{Re } \mathcal{C}_{23}^{u\phi} \neq 0$	$(0.19 \pm 6.51) \times 10^{-4}$	$\mathcal{B}(t \rightarrow uH)$	$\text{Re } \mathcal{C}_{13}^{u\phi} \neq 0$	$(0.77 \pm 5.36) \times 10^{-4}$

Table 12. Branching-ratio predictions for top FCNC decay modes evaluated in different SMEFT scenarios.

Scenario	$\mathcal{B}(t \rightarrow ce^+e^-)$	$\mathcal{B}(t \rightarrow c\mu^+\mu^-)$	$\mathcal{B}(t \rightarrow c\nu\bar{\nu})$
via $t \rightarrow c\gamma$	$(0.47 \pm 2.63) \times 10^{-8}$	$(0.25 \pm 1.39) \times 10^{-8}$	—
via $t \rightarrow cZ$	$(0.20 \pm 4.68) \times 10^{-7}$	$(0.20 \pm 4.68) \times 10^{-7}$	$(0.15 \pm 3.60) \times 10^{-9}$
via $t \rightarrow cH$	$(0.08 \pm 2.66) \times 10^{-16}$	$(0.03 \pm 1.14) \times 10^{-11}$	—
Scenario	$\mathcal{B}(t \rightarrow ue^+e^-)$	$\mathcal{B}(t \rightarrow u\mu^+\mu^-)$	$\mathcal{B}(t \rightarrow u\nu\bar{\nu})$
via $t \rightarrow u\gamma$	$(0.41 \pm 1.08) \times 10^{-6}$	$(2.20 \pm 5.71) \times 10^{-7}$	—
via $t \rightarrow uZ$	$(0.24 \pm 2.06) \times 10^{-7}$	$(0.24 \pm 2.06) \times 10^{-7}$	$(0.18 \pm 1.58) \times 10^{-9}$
via $t \rightarrow uH$	$(0.31 \pm 2.19) \times 10^{-16}$	$(0.13 \pm 0.94) \times 10^{-11}$	—

Table 13. Branching-ratio predictions for different three body top-FCNC processes.

magnitude below the existing bounds. In particular, the one-operator scenarios $\mathcal{O}_{2(1)3}^{uB}$ or $\mathcal{O}_{2(1)3}^{uW}$ with the respective complex WCs, we see our bounds on $\mathcal{B}(t \rightarrow c(u)\gamma)$ and $\mathcal{B}(t \rightarrow c(u)Z)$ are approximately two orders of magnitude smaller than the current experimental bounds. Also, we note $\mathcal{B}(t \rightarrow c(u)Z) \approx 10^{-11}$ for the scenarios with the operator $\mathcal{O}_{2(1)3}^{\phi q(-)}$, which is approximately five-order of magnitude smaller than the current experimental limits. For the other FCNC decay channels, our predictions are found at the ballpark to the current experimental sensitivities.

In addition to the two-body FCNC modes, we have also studied the three-body decays $t \rightarrow u_j \ell^+ \ell^-$, which arise through off-shell photon, Z -, and H -boson exchange. Depending on the choice of intermediate mediator, different SMEFT operators contribute, leading to distinct predictions for the branching fractions of the various $t \rightarrow u_j \ell^+ \ell^-$ and $t \rightarrow u_j \nu\bar{\nu}$ channels. The general expression for the differential decay width of a sequential three-body decay is given by

$$d\Gamma_{A \rightarrow b, q^*(c,d)} = \frac{|\mathcal{M}|^2}{512\pi^3 m_A^3 q^2} \lambda^{1/2}(m_A^2, m_b^2, q^2) \lambda^{1/2}(q^2, m_c^2, m_d^2) dq^2 d\cos\theta \quad (5.6)$$

where λ is the Källén function and q^* denotes the off-shell propagator, which in our case

corresponds to γ^* , Z^* , or H^* . The expression for differential decay width can be written as

$$\frac{d\Gamma(q^2)}{dq^2} \Big|_{t \rightarrow u_j \gamma^*(\ell\ell)} = \frac{e^2 v^2 m_t^3}{96\pi^3 q^2} \left(1 - \frac{q^2}{m_t^2}\right)^2 \left(2 + \frac{q^2}{m_t^2}\right) \left|c_W \mathcal{C}_{pq}^{uB} + s_W \mathcal{C}_{pq}^{uW}\right|^2, \quad (5.7a)$$

$$\begin{aligned} \frac{d\Gamma(q^2)}{dq^2} \Big|_{t \rightarrow u_j Z^*(\ell\ell)} &= \frac{g_Z^2 m_t^3 v^2 (g_{Z_L}^2 + g_{Z_R}^2)}{1536\pi^3 (q^2 - M_Z^2)^2} \left(1 - \frac{q^2}{m_t^2}\right)^2 \left\{ 8q^2 \left(2 + \frac{q^2}{m_t^2}\right) \left|c_W \mathcal{C}_{pq}^{uW} - s_W \mathcal{C}_{pq}^{uB}\right|^2 \right. \\ &\quad \left. + g_Z^2 v^2 \left(1 + \frac{2q^2}{m_t^2}\right) \left|\mathcal{C}_{pq}^{\phi q(-)}\right|^2 \right\}, \end{aligned} \quad (5.7b)$$

$$\frac{d\Gamma(q^2)}{dq^2} \Big|_{t \rightarrow u_j H^*(\ell\ell)} = \frac{9m_t m_\ell^2 v^2 q^2}{1024\pi^3 (q^2 - M_H^2)^2} \left(1 - \frac{q^2}{m_t^2}\right)^2 \left|\mathcal{C}_{pq}^{u\phi}\right|^2. \quad (5.7c)$$

where g_Z , g_{Z_L} , and g_{Z_R} denote the couplings associated with the neutral-current interactions of the Z boson with fermions. They are given by

$$g_Z = \frac{e}{s_W c_W}, \quad g_{Z_L} = I_W^{(3)} - Q_f s_W^2, \quad g_{Z_R} = -Q_f s_W^2,$$

with $I_W^{(3)}$ being the weak isospin of the fermion and Q_f its electric charge. Since the decay $t \rightarrow u_j \nu \bar{\nu}$ proceeds only via an off-shell Z boson, its differential decay rate has the same structure as $t \rightarrow u_j \ell^+ \ell^-$ in the massless limit, with the proper replacement of $Z \nu \bar{\nu}$ coupling. In table 13, we summarise the predicted branching fractions for the three-body FCNC modes in the different scenarios considered. To the best of our knowledge, no experimental upper limits for these channels currently exist. The corresponding SM predictions are extremely small, as reported in refs. [15, 138]:

$$\begin{aligned} \mathcal{B}(t \rightarrow ce^+ e^-) &= 8.48 \times 10^{-15}, & \mathcal{B}(t \rightarrow c\mu^+ \mu^-) &= 9.55 \times 10^{-15}, \\ \mathcal{B}(t \rightarrow ue^+ e^-) &= 6.81 \times 10^{-17}, & \mathcal{B}(t \rightarrow u\mu^+ \mu^-) &= 7.68 \times 10^{-17}, \\ \mathcal{B}(t \rightarrow c \nu \bar{\nu}) &= 2.99 \times 10^{-14}, & \mathcal{B}(t \rightarrow u \nu \bar{\nu}) &= 2.40 \times 10^{-16}. \end{aligned} \quad (5.8)$$

In our analysis, we have predicted branching ratio several order magnitude larger than SM predictions for all these channels, which will provide a well motivated target range for future experimental searches.

$Z(H)$ mediated FCNC interaction:

The top-FCNC interaction vertices can also contribute to the FCNC decays of the Z and H bosons. In the SM, the processes $Z(H) \rightarrow d_i \bar{d}_j$ ($i \neq j$) occur only at the one-loop level and are therefore extremely suppressed, unlike other SM FCNC transitions. The corresponding SM predictions for the branching ratios are $\mathcal{B}(Z(H) \rightarrow b\bar{s}(\bar{d})) \sim \mathcal{O}(10^{-7}(10^{-9}))$ [139, 140], however, at collider, no FCNC decays of the Z or H bosons have been observed so far.

In our analysis, the top-FCNC interactions contributing to the rare Z FCNC decays, with

a similar topology as shown in fig. 5. For $\mathcal{B}(Z \rightarrow b\bar{s})$, the loop amplitude contains a CKM factor of $\mathcal{O}(1)$ when the tcZ coupling is inserted, resulting in the dominant contribution to this decay. Similarly, for $\mathcal{B}(Z \rightarrow b\bar{d})$, the loop arising from the tuZ coupling also carries a CKM factor of $\mathcal{O}(1)$. The same pattern holds for the Higgs FCNC decays, the branching ratio $\mathcal{B}(H \rightarrow b\bar{s})$ is dominated by the tch coupling, while $\mathcal{B}(H \rightarrow b\bar{d})$ receives its dominant contribution from the tuh coupling. However, our NP predictions for these modes remain extremely small and effectively indistinguishable from the SM expectations. Consequently, if any FCNC decay of the Z or H boson were to be observed at colliders, such a signal would not mainly originate from top-FCNC interactions.

5.4 Predictions of a few CP asymmetries

We now present our predictions for the CP-violating observables in the radiative FCNC decay of the top quark. In this analysis, the source of CP violation arises from the interference between amplitudes with relative phase differences. In our framework, the weak phase originates from the complex effective top FCNC couplings, which encapsulate the possible NP effects. On the other hand, there are additional phases generated through one-loop corrections to the decay amplitudes as shown in fig. 13, where loop kinematics give rise to absorptive parts once the intermediate states can go on-shell. Such absorptive contributions are essential to generate a non-vanishing CP asymmetry. In addition, we have taken into account the SM one-loop contributions to these radiative top-FCNC decays. The resulting interplay between the weak phases associated with the complex NP couplings and the CKM-induced weak phase from the SM diagrams, together with the phase arising from the absorptive part of the loop dynamics, constitutes a direct source of CP violation in radiative FCNC top decays.

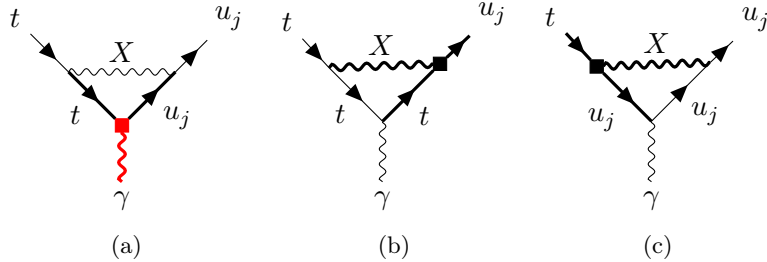


Figure 13. One-loop Feynman diagrams contributing to the radiative decay $t \rightarrow u_j \gamma$, with $X = \gamma, Z, g, H$ denoting neutral intermediate particles. These diagrams also contribute to the FCNC processes $t \rightarrow u_j g$. Self-energy corrections to the external legs of the effective top-photon/gluon vertices are not shown explicitly.

The most general form of the polarised $t \rightarrow u_j \gamma_{\pm}$ amplitudes can be written as,

$$i\mathcal{M}(t \rightarrow u_j + \gamma_{\pm}) = i\bar{u}(p_f) \Gamma_{fi,\gamma}^{\mu}(q^2) u(p_i) \varepsilon_{\pm,\mu}^*(q), \quad (5.9)$$

where $u(p_i)$ and $u(p_f)$ are the Dirac spinors of the initial top and final charm (down) states, respectively, and ε denotes the photon polarisation vectors having momentum $q = (p_i - p_f)$,

γ_+ and γ_- represent the positively and negatively polarised photons, respectively. Here we have followed the same notation as used in ref. [141]. The effective vertex can be written as

$$\Gamma_{fi,\gamma}^\mu(q^2) = i\sigma^{\mu\nu}q_\nu \left(f_{fi,\gamma}^L P_L + f_{fi,\gamma}^R P_R \right). \quad (5.10)$$

where the form factors $f_{fi,\gamma}^L$ and $f_{fi,\gamma}^R$ consist of CKM elements and the complex NP couplings and one-loop integral loop factors and can be further parametrised into

$$f_{fi,\gamma}^L = \sum_\alpha V_{t\alpha}^* V_{u_j\alpha} m_{u_j} \mathcal{F}_\alpha^L + \sum_{l_{\text{NP}}} \mathcal{C}_{l_{\text{NP}}} \mathcal{K}_{l_{\text{NP}}}^L, \quad (5.11a)$$

$$f_{fi,\gamma}^R = \sum_\alpha V_{t\alpha}^* V_{u_j\alpha} m_t \mathcal{F}_\alpha^R + \sum_{l_{\text{NP}}} \mathcal{C}_{l_{\text{NP}}} \mathcal{K}_{l_{\text{NP}}}^R. \quad (5.11b)$$

where the first term in eq. (5.11) corresponds to the one-loop SM contribution to the $t \rightarrow u_j \gamma$ decay, while the second term arises solely from the new-physics sector. In the SM term, α ($\alpha = d, s, b$) denotes the internal down-type quarks, and $\mathcal{F}^{L,R}$ represent the purely loop-induced kinematic functions obtained from the SM contribution, whose explicit expressions can be found in ref. [141]. In contrast, the NP contribution involves $\mathcal{C}_{l_{\text{NP}}}^{L,R}$, which contain the complex NP couplings, and $\mathcal{K}^{L,R}$, which denote the corresponding loop kinematic functions.

Under a CP transformation, each particle is replaced by its corresponding antiparticle, and all additive quantum numbers, including the electric charge, are reversed, while the spin remains unchanged. Therefore, the polarised amplitudes of CP-conjugated processes can be written as

$$i\mathcal{M}(\bar{t} \rightarrow \bar{u}_j + \gamma_\mp) = i\mathcal{M}^{CP}(t \rightarrow u_j + \gamma_\pm) = i\bar{v}(p_i) \bar{\Gamma}_{if,\gamma}^\mu(q^2) v(p_f) \varepsilon_{\mp,\mu}^*(q) \quad (5.12)$$

where $v(p_i)$ and $v(p_f)$ are the Dirac spinors associated with the initial and final anti-fermion states, respectively. The effective vertex function is parametrised in the same manner as introduced earlier.

$$\bar{\Gamma}_{if,\gamma}^\mu(q^2) = i\sigma^{\mu\nu}q_\nu \left(\bar{f}_{if,\gamma}^L P_L + \bar{f}_{if,\gamma}^R P_R \right). \quad (5.13)$$

$$\bar{f}_{if,\gamma}^L = \sum_\alpha V_{t\alpha}^* V_{u_j\alpha} m_t \mathcal{F}_\alpha^R + \sum_{l_{\text{NP}}} \mathcal{C}_{l_{\text{NP}}}^* \mathcal{K}_{l_{\text{NP}}}^R, \quad (5.14a)$$

$$\bar{f}_{if,\gamma}^R = \sum_\alpha V_{t\alpha}^* V_{u_j\alpha} m_{u_j} \mathcal{F}_\alpha^L + \sum_{l_{\text{NP}}} \mathcal{C}_{l_{\text{NP}}}^* \mathcal{K}_{l_{\text{NP}}}^L. \quad (5.14b)$$

It is important to note that, among the various loop diagrams shown in fig. 13, only the diagram fig. 13c gives rise to an absorptive part. In a similar manner, one can compute the polarised amplitudes for the $t \rightarrow u_j g_\pm$ processes following the same procedure.

The polarised CP asymmetries $\Delta_{\text{CP},\pm}$ between $t \rightarrow u_j \gamma_{\pm}$ and its CP conjugate process $\bar{t} \rightarrow \bar{u}_j \gamma_{\mp}$ are defined respectively, as [142]

$$\Delta_{\text{CP},+} = \frac{\Gamma(t \rightarrow u_j \gamma_+) - \Gamma(\bar{t} \rightarrow \bar{u}_j \gamma_-)}{\Gamma(t \rightarrow u_j \gamma) + \Gamma(\bar{t} \rightarrow \bar{u}_j \gamma)} = \frac{\left|f_{fi}^L\right|^2 - \left|\bar{f}_{if}^R\right|^2}{\left|f_{fi}^L\right|^2 + \left|f_{fi}^R\right|^2 + \left|\bar{f}_{if}^L\right|^2 + \left|\bar{f}_{if}^R\right|^2}, \quad (5.15a)$$

$$\Delta_{\text{CP},-} = \frac{\Gamma(t \rightarrow u_j \gamma_-) - \Gamma(\bar{t} \rightarrow \bar{u}_j \gamma_+)}{\Gamma(t \rightarrow u_j \gamma) + \Gamma(\bar{t} \rightarrow \bar{u}_j \gamma)} = \frac{\left|f_{fi}^R\right|^2 - \left|\bar{f}_{if}^L\right|^2}{\left|f_{fi}^L\right|^2 + \left|f_{fi}^R\right|^2 + \left|\bar{f}_{if}^L\right|^2 + \left|\bar{f}_{if}^R\right|^2}, \quad (5.15b)$$

A photon–polarization–independent CP asymmetry can also be obtained by summing over the two polarized asymmetries $\Delta_{\text{CP},+}$ and $\Delta_{\text{CP},-}$, which gives

$$\begin{aligned} \Delta_{\text{CP}} &= \frac{\Gamma(t \rightarrow u_j \gamma_+) - \Gamma(\bar{t} \rightarrow \bar{u}_j \gamma_-) + \Gamma(t \rightarrow u_j \gamma_-) - \Gamma(\bar{t} \rightarrow \bar{u}_j \gamma_+)}{\Gamma(t \rightarrow u_j \gamma) + \Gamma(\bar{t} \rightarrow \bar{u}_j \gamma)}, \\ &= \frac{\Gamma(t \rightarrow u_j \gamma) - \Gamma(\bar{t} \rightarrow \bar{u}_j \gamma)}{\Gamma(t \rightarrow u_j \gamma) + \Gamma(\bar{t} \rightarrow \bar{u}_j \gamma)} = \frac{\left|f_{fi}^L\right|^2 + \left|f_{fi}^R\right|^2 - \left|\bar{f}_{if}^R\right|^2 - \left|\bar{f}_{if}^L\right|^2}{\left|f_{fi}^L\right|^2 + \left|f_{fi}^R\right|^2 + \left|\bar{f}_{if}^L\right|^2 + \left|\bar{f}_{if}^R\right|^2}. \end{aligned} \quad (5.16)$$

Using the parametrisations of the form factors given in eqs. (5.11) and (5.14), the two polarised CP asymmetries can be further expressed in terms of the particle masses, loop functions, CKM matrix elements, and complex NP couplings. The resulting expression can then be written as

$$\Delta_{\text{CP},+} = -\frac{m_{u_j}^2 \sum_{\alpha, \beta} \mathcal{J}_{\alpha\beta} \text{Im}(\mathcal{F}_{\alpha}^L \mathcal{F}_{\beta}^{L*}) + 2m_{u_j} \sum_{\alpha, l_{\text{NP}}} \text{Im}(V_{t\alpha} V_{u_j\alpha}^* \mathcal{C}_{l_{\text{NP}}}) \text{Im}(\mathcal{K}_{l_{\text{NP}}}^L \mathcal{F}_{\alpha}^{L*}) + \sum_{l_{\text{NP}} \neq l'_{\text{NP}}} \text{Im}(\mathcal{C}_{l_{\text{NP}}} \mathcal{C}_{l'_{\text{NP}}}^*) \text{Im}(\mathcal{K}_{l_{\text{NP}}}^L \mathcal{K}_{l'_{\text{NP}}}^{L*})}{\mathcal{D}} \quad (5.17a)$$

$$\Delta_{\text{CP},-} = -\frac{m_t^2 \sum_{\alpha, \beta} \mathcal{J}_{\alpha\beta} \text{Im}(\mathcal{F}_{\alpha}^R \mathcal{F}_{\beta}^{R*}) + 2m_t \sum_{\alpha, l_{\text{NP}}} \text{Im}(V_{t\alpha} V_{u_j\alpha}^* \mathcal{C}_{l_{\text{NP}}}) \text{Im}(\mathcal{K}_{l_{\text{NP}}}^R \mathcal{F}_{\alpha}^{R*}) + \sum_{l_{\text{NP}} \neq l'_{\text{NP}}} \text{Im}(\mathcal{C}_{l_{\text{NP}}} \mathcal{C}_{l'_{\text{NP}}}^*) \text{Im}(\mathcal{K}_{l_{\text{NP}}}^R \mathcal{K}_{l'_{\text{NP}}}^{R*})}{\mathcal{D}} \quad (5.17b)$$

with the denominator given by

$$\begin{aligned} \mathcal{D} &= \sum_{\alpha, \beta} \mathcal{R}_{\alpha\beta} \left\{ m_t^2 \text{Re}(\mathcal{F}_{\alpha}^R \mathcal{F}_{\beta}^{R*}) + m_{u_j}^2 \text{Re}(\mathcal{F}_{\alpha}^L \mathcal{F}_{\beta}^{L*}) \right\}, \\ &+ 2 \sum_{\alpha, l_{\text{NP}}} \text{Re}(V_{t\alpha} V_{u_j\alpha}^* \mathcal{C}_{l_{\text{NP}}}) \left\{ m_t \text{Re}(\mathcal{F}_{\alpha}^{R*} \mathcal{K}_{l_{\text{NP}}}^R) + m_{u_j} \text{Re}(\mathcal{F}_{\alpha}^{L*} \mathcal{K}_{l_{\text{NP}}}^L) \right\}, \\ &+ \sum_{l_{\text{NP}}, l'_{\text{NP}}} \text{Re}(\mathcal{C}_{l_{\text{NP}}} \mathcal{C}_{l'_{\text{NP}}}^*) \left\{ \text{Re}(\mathcal{K}_{l_{\text{NP}}}^L \mathcal{K}_{l'_{\text{NP}}}^{L*}) + \text{Re}(\mathcal{K}_{l_{\text{NP}}}^R \mathcal{K}_{l'_{\text{NP}}}^{R*}) \right\}. \end{aligned} \quad (5.18)$$

where $\alpha, \beta = d, s, b$ and

$$\mathcal{J}_{\alpha\beta} = \text{Im} \left(V_{t\alpha}^* V_{u_j\alpha} V_{t\beta} V_{u_j\beta}^* \right), \quad \mathcal{R}_{\alpha\beta} = \text{Re} \left(V_{t\alpha}^* V_{u_j\alpha} V_{t\beta} V_{u_j\beta}^* \right). \quad (5.19)$$

It is evident from eqs. (5.17a) and (5.17b) that a non-vanishing CP asymmetry requires the interference of at least two amplitudes possessing different weak and strong phases. In our analysis, the weak phase originates from the complex NP effective couplings, the Jarlskog invariant ($\mathcal{J}_{\alpha\beta}$), and the products of CKM matrix elements with these complex couplings, which together quantify the strength of CP violation.

Decay Channel	$\Delta_{\text{CP},+}$	$\Delta_{\text{CP},-}$
$t \rightarrow c \gamma$	$(1.05 \pm 4.93) \times 10^{-4}$	$(-0.11 \pm 6.06) \times 10^{-3}$
$t \rightarrow u \gamma$	$(-2.31 \pm 6.56) \times 10^{-9}$	$(-0.26 \pm 2.24) \times 10^{-4}$
$t \rightarrow c g$	$(-0.05 \pm 1.81) \times 10^{-4}$	$(-0.95 \pm 6.30) \times 10^{-3}$
$t \rightarrow u g$	$(-1.18 \pm 3.52) \times 10^{-8}$	$(-0.32 \pm 1.19) \times 10^{-4}$

Table 14. Results for the CP asymmetries for different top FCNC radiative decay channels $t \rightarrow u_j \gamma$ and $t \rightarrow u_j g$.

Since the left-chiral effective couplings are generally less constrained than their right-chiral counterparts across the various top FCNC processes, and because we have already demonstrated that their allowed parameter space can be further restricted using collider bounds, we tighten the left-chiral tensor and scalar couplings by incorporating the current collider limits, while keeping the remaining couplings at their global-fit values. In table 5.4, we summarise our predictions for the CP asymmetries in different radiative top FCNC decays. The results clearly exhibit the hierarchy $\Delta_{\text{CP},+} < \Delta_{\text{CP},-}$, which follows directly from angular momentum conservation and the $V-A$ structure of the weak interaction, indicate that the photons (or gluons) emitted in top FCNC radiative decays are predominantly left-handed. Moreover, the inclusion of complex NP couplings leads to a substantial enhancement of the CP-violating observables. The resulting CP asymmetries are significantly larger than the corresponding SM expectations [5, 141], with enhancements of at least $\mathcal{O}(10) \times \Delta_{\text{CP}}^{\text{SM}}$ for the $t \rightarrow c\gamma$ and $t \rightarrow cg$ channel which can be tested in future precision experiments.

5.5 Electric dipole moment of light quark

Experimentally, EDMs are not measured directly for the light quarks, since they are confined inside the hadrons. Instead, constraints arise from the precision measurement of the composite systems, such as the neutron [143], proton EDMs, diamagnetic atom (e.g., Hg, Ra, Xe), or paramagnetic molecules (e.g., Th, YbF, HfF) [144–146]. These observables are sensitive to a combination of light-quark EDMs, chromo EDMs (CEDMs), and the CP-odd three gluon Weinberg operators, which allows us to place indirect bounds on quark-level CP violation. There exists a vast literature on EDM calculations, where EDMs are parametrized in terms of various effective operators [147–151], as well as within specific BSM models [152–155]. In our analysis, the EDMs of both light quarks (u, d, s) and heavy

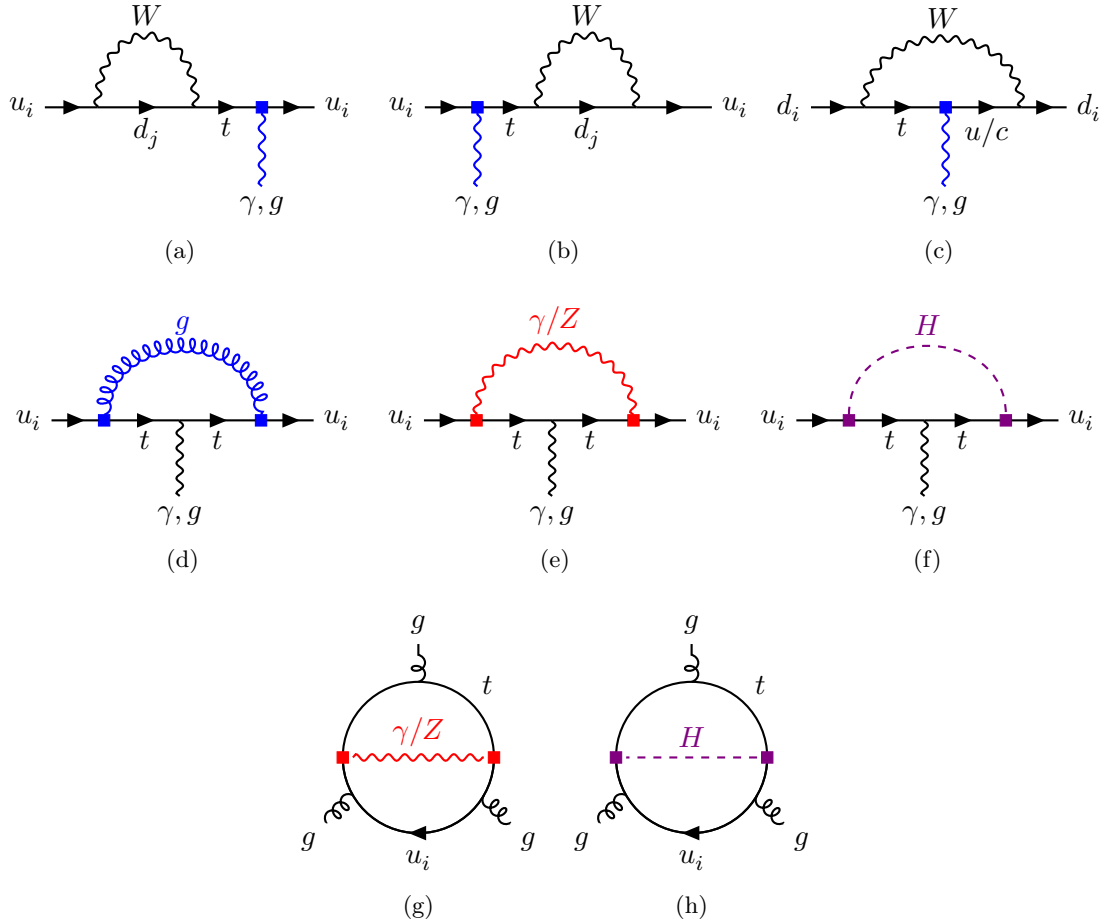


Figure 14. Dipole moment of light quarks affected by the top FCNC operators. Here u_i denotes u and c -quark respectively. The diagrams in the last row denote the contribution of NP in the Weinberg operator.

quarks (c, b, t) are affected by the top-FCNC couplings. The bounds from the top EDM has already been taken into account in our global χ^2 minimization. Generally, the low-energy effective Lagrangian for the hadronic EDM can be expressed as [156]

$$\mathcal{L}_{\text{eff}} \supset +d_q(\mu) \frac{i}{2} \bar{q} \sigma^{\mu\nu} \gamma_5 q F_{\mu\nu} + \tilde{d}_q(\mu) \frac{i}{2} g_s(\mu) \bar{q} \sigma^{\mu\nu} T^a \gamma_5 q G_{\mu\nu}^a + w(\mu) \frac{1}{3} G_{\mu\sigma}^a G_{\nu}^{b,\sigma} \tilde{G}^{c,\mu\nu} \quad (5.20)$$

Here, q runs over all quark flavours except the top quark. $F_{\mu\nu}$ and $G_{\mu\nu}^a$ denote the field strength tensors of QED and QCD, respectively, while $\tilde{G}^{a\mu\nu} = \frac{1}{2} \epsilon^{\mu\nu\alpha\beta} G_{\alpha\beta}^a$ is the dual QCD field strength tensor. The quantities $d_q(\mu)$ and $\tilde{d}_q(\mu)$ represent the EDM and chromo-EDM (cEDM) of quarks, respectively.

Light-quark EDMs contribution to neutron EDMs: The EDMs of the light quarks (u, d, s) contribute directly to the EDM of the nucleon. Their effect are typically encoded through the hadronic matrix elements, connecting fundamental dipole operators to measurable neutron and proton EDMs. In the case of the quark dipole operators, the hadronic

input is captured by the quark tensor charges, which have been computed on the Lattice QCD [75, 157]. The estimate is available only for the neutron EDM, which is expressed as given below in terms of the light-quark contributions [147]:

$$\begin{aligned} \frac{d_n}{e} &= \left(g_T^d \frac{d_u}{e} + g_T^u \frac{d_d}{e} + g_T^s \frac{d_s}{e} \right) + (1 \pm 0.5) \times 1.1 \left(\tilde{d}_d + 0.5 \tilde{d}_u \right) , \\ &+ (22 \pm 10) \times 10^{-3} \text{GeV}\cdot w . \end{aligned} \quad (5.21)$$

In this equation, the terms in the first parenthesis correspond to the contributions arising from the light-quark EDMs, while those in the second parenthesis account for the contributions from the CEDM. The contribution displayed in the second line originates from the Weinberg operator, as defined in eq. 5.20. Here, the values of the hadronic charge currents at the renormalisation scale (Hadronic scale) $\mu_{\text{had}} = 2 \text{ GeV}$ are [75]

$$g_T^u = 0.784(28)(10), \quad g_T^d = -0.204(11)(10), \quad g_T^s = -0.0027(16) . \quad (5.22)$$

The current 90% CL upper limit on the neutron EDM reads as [143]

$$\left| \frac{d_n}{e} \right| < 1.8 \times 10^{-26} \text{ cm.} \quad (5.23)$$

Fig 14 illustrates the loop diagrams through which the various top-quark FCNC couplings contribute to the EDMs and CEDMs of the light quarks (u, d, s). In addition to diagrams with single insertions of the NP couplings, we also include topologies involving double insertions. These contributions are particularly important, as the corresponding loop amplitudes are dominated by the top-quark contribution and can therefore be numerically significant. We emphasize that the contribution of the Weinberg operator, $w(\mu_t)$, is numerically negligible for light quark hadronic EDMs and is thus not relevant for the evaluation of the light-quark EDMs [156]³.

We have matched the 1-loop contributions in fig. 14 to the effective operators defined in eq. 5.20 and obtain the expressions for the light quark EDMs d_q and \tilde{d}_q . The resulting expressions are shown in the Appendix C. These EDMs are also expressed in terms of the LEFT coefficients, which are as follows:

$$d_q(\mu) = 2 \text{Im}[L_{ii}^{q\gamma}](\mu), \quad \tilde{d}_q(\mu) = \frac{2}{g_s(\mu)} \text{Im}[L_{ii}^{qG}](\mu). \quad (5.24)$$

Note that in this equation, we define $L_{ii}/\Lambda \equiv L_{ii}$, which has dimension GeV^{-1} . Hence, we need to convert it into units of cm for consistency with the conventional EDM normalisation. In terms of the LEFT coefficients or light-quark EDMs, the nucleon EDMs can be written as

$$\begin{aligned} \frac{d_n}{e}(\mu) &= -\frac{3.94 \times 10^{-14}}{e} \left(g_T^d \text{Im}[L_{11}^{u\gamma}](\mu_{\text{had}}) + g_T^u \text{Im}[L_{11}^{d\gamma}](\mu_{\text{had}}) + g_T^s \text{Im}[L_{22}^{d\gamma}](\mu_{\text{had}}) \right) , \\ &- \frac{4.3 \times 10^{-14}}{g_s(\mu)} (1 \pm 0.5) \left\{ \text{Im}[L_{11}^{dG}](\mu_{\text{had}}) + 0.5 \text{Im}[L_{11}^{uG}](\mu_{\text{had}}) \right\} . \end{aligned} \quad (5.25)$$

³The contribution from the Weinberg operator becomes relevant when computing the EDMs of the heavier c - and b -quarks, which are not considered in this work. Since the effective operators defined in eq. 5.20 are evaluated at the scale $\mu = 2 \text{ GeV}$, we work within an effective theory with three active light flavours, which excludes the c and b quarks.

As mentioned above, here, we have done an explicit unit conversion ($1\text{GeV}^{-1} = 1.97 \times 10^{-14} \text{cm}$) and the resulting expressions have the unit cm.

It is important to note that all the low-energy couplings appearing in eq. (5.21) are defined at the hadronic scale, μ_{had} . The running of these couplings from the electroweak scale (μ_{EW}) down to μ_{had} is performed through the LEFT framework at leading-logarithmic approximation, as described in ref. [158].

$$\begin{pmatrix} L^{u\gamma} \\ L^{uG} \\ L^{d\gamma} \\ L^{dG} \end{pmatrix}_{\mu_{\text{had}}} = \begin{pmatrix} 0.87 & -0.064 & 0 & 0 \\ -0.05 & 1.23 & 0 & 0 \\ 0 & 0 & 0.88 & 0.03 \\ 0 & 0 & 0.024 & 1.23 \end{pmatrix} \begin{pmatrix} L^{u\gamma} \\ L^{uG} \\ L^{d\gamma} \\ L^{dG} \end{pmatrix}_{\mu_{\text{EW}}} \quad (5.26)$$

The same RGE matrix given in eq. (5.26) can be used for the evolution of both the quark EDMs (d_q) and CEDMs (\tilde{d}_q). However, it is important to note that in the matching relation of eq. (5.24), the strong coupling $g_s(\mu)$ appears explicitly. Since $g_s(\mu)$ varies significantly toward low energies, an additional factor of $(g_s(\mu_{\text{EW}})/g_s(\mu_{\text{had}}))$ must be included when relating $\tilde{d}_q(\mu_{\text{had}})$ to $\tilde{d}_q(\mu_{\text{EW}})$ through the LEFT RGE matrix.

Additionally, we should note that at the hadronic scale, μ_{had} , the dipole moments of the light quarks can be expressed, in the leading-logarithmic approximation, in terms of the CEDM of the charm quark [156].

$$\begin{aligned} \frac{d_d(\mu_{\text{had}})}{e} &= 2.3 \times 10^{-8} \tilde{d}_c(\mu_t) + 1.0 \times 10^{-4} \text{GeV} \cdot w(\mu_t), \\ \frac{d_u(\mu_{\text{had}})}{e} &= -2.1 \times 10^{-8} \tilde{d}_c(\mu_t) - 9.1 \times 10^{-5} \text{GeV} \cdot w(\mu_t), \\ \tilde{d}_d(\mu_{\text{had}}) &= 1.8 \times 10^{-6} \tilde{d}_c(\mu_t) + 7.0 \times 10^{-4} \text{GeV} \cdot w(\mu_t), \\ \tilde{d}_u(\mu_{\text{had}}) &= 8.2 \times 10^{-7} \tilde{d}_c(\mu_t) + 3.1 \times 10^{-4} \text{GeV} \cdot w(\mu_t), \\ w(\mu_{\text{had}}) &= 1.7 \times 10^{-2} \text{GeV}^{-1} \tilde{d}_c(\mu_t) + 0.41 w(\mu_t). \end{aligned} \quad (5.27)$$

Unlike the light quarks, the b and c quarks are not directly included in the nucleon EDM, we integrate out the b and c quarks at their corresponding mass threshold, thus we do not consider non-perturbative matrix elements of operators with b and c quarks between nucleons or pions rather, their contributions are taken into account indirectly, via RGE-induced mixing and matching at the corresponding heavy-quark mass thresholds [40, 159, 160]. Hence, there are contributions to the light quark EDMs and CEDMs from the Weinberg operator and the charm chromo-dipole operators via the operator mixing in the respective RGEs. Since the charm quark lies at the boundary between the perturbative and non-perturbative regimes, ref. [161] attempted to evaluate the charm matrix element directly in Lattice QCD, without integrating out the charm quark; however, these results are preliminary with large hadronic uncertainties. Recently, several attempts have been made to place indirect bounds on the b - and c -quark contributions via RGE effects, through their mixing into the EDMs of the u and d quarks as well as the Weinberg operator (w), as discussed in refs. [150, 156, 162].

In our analysis, we have considered only the RGE effects associated with the charm quark, as its loop contributions are dominant.

Note that the Weinberg operator in eq. (5.20) mixes, under renormalisation, into the quark EDMs and CEDMs, whereas the reverse mixing does not occur [156]. By inserting eq. (5.27) into eq. (5.21), the contribution to the neutron EDM only from the charm-quark CEDM evaluated at the scale μ_t can be written as

$$\left| \frac{d_n}{e} \right| = \left| (3.7 \pm 1.7) \times 10^{-4} \cdot \tilde{d}_c(\mu_t) + (9.3 \pm 4.1) \times 10^{-3} \text{GeV} \cdot w(\mu_t) \right| \quad (5.28)$$

From the above discussion, it is evident that within our working framework the dominant contributions to the neutron EDM, d_n , arise from the light-quark (u, d, s) EDMs and CEDMs defined in eq. 5.25, as well as from those induced through RGE and operator mixing, as described in eqs. 5.26 and 5.28.

If NP effects are present only in the $t \rightarrow u$ transition, or simultaneously in both $t \rightarrow u$ and $t \rightarrow c$ transitions, the dominant contributions to d_n originate solely from the light-quark EDMs and CEDMs in eq. 5.25, including those generated via RGE mixing as in eq. 5.26. In this case, the contributions from charm dipole operators, evaluated at the electroweak scale μ_{EW} and evolved down to the hadronic scale μ_{had} , are numerically negligible.

In contrast, if NP effects are assumed to affect only the $t \rightarrow c$ FCNC vertices, the dominant contribution to the neutron EDM arises from the charm-quark CEDM through RGE-induced mixing, as given in eq. 5.28, all the other contributions are negligible.

Constraint from Neutron EDM: In this part of our analysis, we examine in detail the impact of EDM constraints on the NP parameter space associated with the top-FCNC interactions. To isolate the effects arising from each sector, we study one class of couplings (tu_jX) at a time, allowing us to derive clean and model-independent bounds on the corresponding NP interactions. The Neutron EDM provides an especially sensitive probe the combination of the imaginary components of these NP couplings, and by using the expressions presented in eqs. (5.29), we determine the constraints on the relevant combinations of the NP parameters. For the tu_jZ sector in particular, the EDM contributions can also arise from a specific combination of the vector couplings $X_{L,R}^{u_j t}$ and the tensor (dipole) couplings $\kappa_{L,R}^{u_j t}$. The detailed structure of these interactions, together with the explicit expressions showing how the NP top-FCNC operators feed into the light-quark EDMs, is presented in the Appendix C. These numerical bounds significantly restrict the allowed region of the FCNC parameter space and highlight the strong discriminatory power of EDM measure-

ments in probing CP-violating new physics in the top sector.

$$\left| \text{Im} \left(\xi_L^{ut} \xi_R^{tu*} \right) \right| < 2.20 \times 10^{-8}, \quad \left| \text{Im} \left(\xi_L^{ct} \xi_R^{tc*} \right) \right| < 0.89 \times 10^{-4}, \quad (5.29a)$$

$$\left| \text{Im} \left(\lambda_L^{ut} \lambda_R^{tu*} \right) \right| < 2.19 \times 10^{-7}, \quad \left| \text{Im} \left(\lambda_L^{ct} \lambda_R^{tc*} \right) \right| < 2.39 \times 10^{-4}, \quad (5.29b)$$

$$\left| \text{Im} \left(\eta_L^{ut} \eta_R^{tu*} \right) \right| < 1.61 \times 10^{-7}, \quad \left| \text{Im} \left(\eta_L^{ct} \eta_R^{tc*} \right) \right| < 1.76 \times 10^{-4}, \quad (5.29c)$$

$$\left| \text{Im} \left(\kappa_L^{ut} \kappa_R^{tu*} \right) \right| < 3.63 \times 10^{-8}, \quad \left| \text{Im} \left(\kappa_L^{ct} \kappa_R^{tc*} \right) \right| < 3.97 \times 10^{-5}, \quad (5.29d)$$

$$\left| \text{Im} \left(X_L^{ut} X_R^{tu*} \right) \right| < 2.54 \times 10^{-7}, \quad \left| \text{Im} \left(X_L^{ct} X_R^{tc*} \right) \right| < 2.79 \times 10^{-4}. \quad (5.29e)$$

It is important to note that, in our global analysis, the couplings $X_{L(R)}^{ut}$ are taken to be real, as they originate from Hermitian operators. However, when evaluating the neutron EDM, we allow these couplings to be complex in order to explicitly probe the sensitivity of EDM observables to their CP-violating phases. Therefore, the neutron EDM provides a stringent constraint on the product of the real and imaginary parts of the left- and right-handed FCNC couplings. As a consequence, the real component of a left-handed coupling and the imaginary component of the corresponding right-handed coupling, and vice versa, are expected to be strongly and negatively correlated.

The above constraints can be exploited to derive bounds on the individual real and imaginary components of the left- and right-handed couplings. The following are the bounds on the product couplings we can infer from the above constraints:

$$\left| \text{Im} \left(\xi_L^{ut} \right) \text{Re} \left(\xi_R^{tu*} \right) \right|, \left| \text{Re} \left(\xi_L^{ut} \right) \text{Im} \left(\xi_R^{tu*} \right) \right| < 2.20 \times 10^{-8}, \quad (5.30a)$$

$$\left| \text{Im} \left(\xi_L^{ct} \right) \text{Re} \left(\xi_R^{tc*} \right) \right|, \left| \text{Re} \left(\xi_L^{ct} \right) \text{Im} \left(\xi_R^{tc*} \right) \right| < 0.89 \times 10^{-4}, \quad (5.30b)$$

$$\left| \text{Im} \left(\lambda_L^{ut} \right) \text{Re} \left(\lambda_R^{tu*} \right) \right|, \left| \text{Re} \left(\lambda_L^{ut} \right) \text{Im} \left(\lambda_R^{tu*} \right) \right| < 2.19 \times 10^{-7}, \quad (5.30c)$$

$$\left| \text{Im} \left(\lambda_L^{ct} \right) \text{Re} \left(\lambda_R^{tc*} \right) \right|, \left| \text{Re} \left(\lambda_L^{ct} \right) \text{Im} \left(\lambda_R^{tc*} \right) \right| < 2.39 \times 10^{-4}, \quad (5.30d)$$

$$\left| \text{Im} \left(\eta_L^{ut} \right) \text{Re} \left(\eta_R^{tu*} \right) \right|, \left| \text{Re} \left(\eta_L^{ut} \right) \text{Im} \left(\eta_R^{tu*} \right) \right| < 1.61 \times 10^{-7}, \quad (5.30e)$$

$$\left| \text{Im} \left(\eta_L^{ct} \right) \text{Re} \left(\eta_R^{tc*} \right) \right|, \left| \text{Re} \left(\eta_L^{ct} \right) \text{Im} \left(\eta_R^{tc*} \right) \right| < 1.76 \times 10^{-4}, \quad (5.30f)$$

$$\left| \text{Im} \left(\kappa_L^{ut} \right) \text{Re} \left(\kappa_R^{tu*} \right) \right|, \left| \text{Re} \left(\kappa_L^{ut} \right) \text{Im} \left(\kappa_R^{tu*} \right) \right| < 3.63 \times 10^{-8}, \quad (5.30g)$$

$$\left| \text{Im} \left(\kappa_L^{ct} \right) \text{Re} \left(\kappa_R^{tc*} \right) \right|, \left| \text{Re} \left(\kappa_L^{ct} \right) \text{Im} \left(\kappa_R^{tc*} \right) \right| < 3.97 \times 10^{-5}, \quad (5.30h)$$

$$\left| \text{Im} \left(X_L^{ut} \right) \text{Re} \left(X_R^{tu*} \right) \right|, \left| \text{Re} \left(X_L^{ut} \right) \text{Im} \left(X_R^{tu*} \right) \right| < 2.54 \times 10^{-7}, \quad (5.30i)$$

$$\left| \text{Im} \left(X_L^{ct} \right) \text{Re} \left(X_R^{tc*} \right) \right|, \left| \text{Re} \left(X_L^{ct} \right) \text{Im} \left(X_R^{tc*} \right) \right| < 2.79 \times 10^{-4}. \quad (5.30j)$$

The limits on the relevant product combinations of couplings in the $t \rightarrow c$ sector are comparatively weaker than those on $t \rightarrow u$ couplings. In the same spirit, the above bounds can be represented in terms of the bounds on the connected SMEFT WCs, which are as

given below:

$$\left| \operatorname{Re} \left(\mathcal{C}_{31}^{uG} \right) \operatorname{Im} \left(\mathcal{C}_{13}^{uG} \right) \right|, \left| \operatorname{Im} \left(\mathcal{C}_{31}^{uG} \right) \operatorname{Re} \left(\mathcal{C}_{13}^{uG} \right) \right| < 0.91 \times 10^{-17} \quad (5.31a)$$

$$\left| \operatorname{Re} \left(\mathcal{C}_{32}^{uG} \right) \operatorname{Im} \left(\mathcal{C}_{23}^{uG} \right) \right|, \left| \operatorname{Im} \left(\mathcal{C}_{32}^{uG} \right) \operatorname{Re} \left(\mathcal{C}_{23}^{uG} \right) \right| < 3.68 \times 10^{-14} \quad (5.31b)$$

$$\left[\left| \operatorname{Re} \left(\mathcal{C}_{31}^{uW} \right) \operatorname{Im} \left(\mathcal{C}_{13}^{uW} \right) \right|, \left| \operatorname{Im} \left(\mathcal{C}_{31}^{uW} \right) \operatorname{Re} \left(\mathcal{C}_{13}^{uW} \right) \right|, \right] < 1.15 \times 10^{-17} \quad (5.31c)$$

$$\left[\left| \operatorname{Re} \left(\mathcal{C}_{32}^{uW} \right) \operatorname{Im} \left(\mathcal{C}_{23}^{uW} \right) \right|, \left| \operatorname{Im} \left(\mathcal{C}_{32}^{uW} \right) \operatorname{Re} \left(\mathcal{C}_{23}^{uW} \right) \right|, \right] < 1.26 \times 10^{-14} \quad (5.31d)$$

$$\left| \operatorname{Re} \left(\mathcal{C}_{31}^{u\phi} \right) \operatorname{Im} \left(\mathcal{C}_{13}^{u\phi} \right) \right|, \left| \operatorname{Im} \left(\mathcal{C}_{31}^{u\phi} \right) \operatorname{Re} \left(\mathcal{C}_{13}^{u\phi} \right) \right| < 1.95 \times 10^{-17} \quad (5.31e)$$

$$\left| \operatorname{Re} \left(\mathcal{C}_{32}^{u\phi} \right) \operatorname{Im} \left(\mathcal{C}_{23}^{u\phi} \right) \right|, \left| \operatorname{Im} \left(\mathcal{C}_{32}^{u\phi} \right) \operatorname{Re} \left(\mathcal{C}_{23}^{u\phi} \right) \right| < 2.14 \times 10^{-14} \quad (5.31f)$$

6 Summary

In this work, we have analysed the constraints on the couplings of the rare top-FCNC effective interaction. We started from a general parametrisation of the top-FCNC couplings in the effective Lagrangian, then we mapped them onto the SMEFT operator basis at μ_t scale and constrained the corresponding effective couplings or the SMEFT WCs using a broad set of observables. Our global analysis incorporates low-energy flavour measurements, electroweak precision observables, Higgs and gauge-boson data and the available input of top EDM and chromomagnetic EDM. The couplings are connected at different scales via RGE, and our framework allows high- and low-energy observables to be combined consistently, thereby strengthening the overall sensitivity to new physics.

In this study, we consider the couplings of the dipole operator to be complex and obtain constraints on the real and imaginary components of the left- and right-handed couplings, separately and combinedly. As a special case, we also explore the scenario in which all couplings are taken to be real. Following our analysis, the bounds obtained on the complex right-handed couplings are relatively tighter than the respective left-handed couplings, which is primarily driven by the radiative and rare B -meson decays. Our bounds on the right-handed couplings are consistent with the current bounds from the collider searches on the top-FCNC rare decay rates. We further translate these results into the SMEFT basis, and we observed that top-gluon and top-photon dipole coefficients are constrained at $\mathcal{O}(10^{-7}) - \mathcal{O}(10^{-8})$ order, and top-Higgs operator remains less restrictive $\mathcal{O}(10^{-6})$. We have also explored the RG evolution of these SMEFT WCs up to multi-TeV energy scales, identifying the characteristic patterns dictated by the gauge structure of the theory.

Using the most strongly constrained WCs, we further predict the branching ratios for a variety of top-FCNC processes for both the two-body decays $t \rightarrow u_j X$ and their three-body extensions, finding values several orders of magnitude above their SM expectations yet comfortably accommodate within current experimental limits. In particular, our predictions for the channels $t \rightarrow u_j \ell^+ \ell^-$ and $t \rightarrow u_j \nu \bar{\nu}$ yield a characteristic target region in the ballpark of 10^{-9} – 10^{-6} , providing well-motivated benchmarks for future LHC searches. For FCNC decays of Z , H -boson, our prediction remains extremely suppressed, indicating any future observation of these modes would never originate primarily from top-FCNC interactions. In addition, we have studied CP asymmetries in radiative top FCNC decays; the complex phase of NP couplings yields substantial enhancements of the CP-violating observables.

Overall, our study demonstrates the power of combining observables from different energy sectors in a model-independent manner. Importantly, our analysis highlights the necessity of treating the effective couplings as complex parameters. Although the inclusion of CP-violating phases enlarges the viable parameter space, it simultaneously gives rise to distinctive phenomenological effects—most importantly, observable CP violation. Future collider experiments, including the HL-LHC and proposed lepton colliders, will be able to probe a significant portion of the parameter space identified in this work. Such measurements will offer valuable insights into the flavour structure of the top quark and the possible CP-violating dynamics associated with its FCNC interactions.

Furthermore, we have analysed neutron-EDM constraints in scenarios where top-FCNC operators contribute at one loop. From these data, we derive bounds on products of left- and right-handed couplings. The resulting limits on the product couplings associated with the $t \rightarrow u$ FCNC operators are significantly tighter than those for $t \rightarrow c$. Combining the stringent bounds on the $t \rightarrow u$ product couplings with the independent limits on the corresponding right-handed couplings from the global fit allows us to infer limits on the left-handed effective couplings and vice versa. They are highly correlated. We can translate these numbers into the products of the associated SMEFT WCs and improve the bounds on them.

Acknowledgments

SK would like to thank Dr. Lipika Kolay and Mr. Utsab Dey for several useful and insightful discussions.

A RGEs: beta functions

In this section, we present the beta functions employed in our analysis, together with the values of the relevant SM input parameters used in the RGE.

$$[\beta^{uG}]_{rs} = -\frac{1}{36} \left(81g_2^2 + 19g_1^2 + 204g_s^2 \right) [\mathcal{C}^{uG}]_{rs} + 6g_2g_s[\mathcal{C}^{uW}]_{rs} + \frac{10}{3}g_1g_s[\mathcal{C}^{uB}]_{rs} \quad (\text{A.1a})$$

$$+ 2[\Gamma_u\Gamma_u^\dagger\mathcal{C}^{uG}]_{rs} - 2[\Gamma_d\Gamma_d^\dagger\mathcal{C}^{uG}]_{rs} + [\mathcal{C}_{uG}\Gamma_u^\dagger\Gamma_u] + \gamma_H^{(Y)}[\mathcal{C}^{uG}]_{rs} + [\gamma_q^{(Y)}\mathcal{C}^{uG}]_{rs} + [\mathcal{C}^{uG}\gamma_u^{(Y)}]_{rs},$$

$$[\beta^{uW}]_{rs} = -\frac{1}{36} (33g_2^2 + 19g_1^2 - 96g_s^2) [\mathcal{C}^{uW}]_{rs} + \gamma_H^{(Y)}[\mathcal{C}^{uW}]_{rs} + [\gamma_q^{(Y)}\mathcal{C}^{uW}]_{rs} + [\mathcal{C}^{uW}\gamma_u^{(Y)}]_{rs}$$

$$+ [\mathcal{C}^{uW}\Gamma_u^\dagger\Gamma_u]_{rs} + 2[\Gamma_d\Gamma_d^\dagger\mathcal{C}^{uW}]_{rs} - \frac{1}{6}g_1g_2[\mathcal{C}^{uB}]_{rs} + \frac{8}{3}g_2g_s[\mathcal{C}^{uG}]_{rs} \quad (\text{A.1b})$$

$$[\beta^{uB}]_{rs} = -\frac{1}{36} (81g_2^2 - 313g_1^2 - 96g_s^2) [\mathcal{C}^{uB}]_{rs} + \gamma_H^{(Y)}[\mathcal{C}^{uB}]_{rs} + [\gamma_q^{(Y)}\mathcal{C}^{uB}]_{rs} + [\mathcal{C}^{uB}\gamma_u^{(Y)}]_{rs}$$

$$- \frac{1}{2}g_1g_2[\mathcal{C}^{uW}]_{rs} - 2[\Gamma_d\Gamma_d^\dagger\mathcal{C}^{uB}]_{rs} + 2[\Gamma_u\Gamma_u^\dagger\mathcal{C}^{uB}]_{rs} + [\mathcal{C}^{uB}\Gamma_u^\dagger\Gamma_u]_{rs} + \frac{40}{9}g_1g_s[\mathcal{C}^{uG}]_{rs} \quad (\text{A.1c})$$

$$[\beta^{\phi q(1)}]_{rs} = \frac{1}{3}g_1^2[\mathcal{C}^{\phi q(1)}]_{rs} + \frac{3}{2} \left([\Gamma_d\Gamma_d^\dagger\mathcal{C}^{\phi q(1)}]_{rs} + [\Gamma_u\Gamma_u^\dagger\mathcal{C}^{\phi q(1)}]_{rs} + [\mathcal{C}^{\phi q(1)}\Gamma_d\Gamma_d^\dagger]_{rs} + [\mathcal{C}^{\phi q(1)}\Gamma_u\Gamma_u^\dagger]_{rs} \right. \\ \left. + 3[\Gamma_d\Gamma_d^\dagger\mathcal{C}^{\phi q(3)}]_{rs} - 3[\Gamma_u\Gamma_u^\dagger\mathcal{C}^{\phi q(3)}]_{rs} + 3[\mathcal{C}^{\phi q(3)}\Gamma_d\Gamma_d^\dagger]_{rs} - 3[\mathcal{C}^{\phi q(3)}\Gamma_u\Gamma_u^\dagger]_{rs} \right) \\ + 2\gamma_H^{(Y)}[\mathcal{C}^{\phi q(1)}]_{rs} + [\gamma_q^{(Y)}\mathcal{C}^{\phi q(1)}]_{rs} + [\mathcal{C}^{\phi q(1)}\gamma_q^{(Y)}]_{rs} \quad (\text{A.1d})$$

$$[\beta^{\phi q(3)}]_{rs} = -\frac{17}{3}g_2^2[\mathcal{C}^{\phi q(3)}]_{rs} + \frac{1}{2} \left(3[\Gamma_d\Gamma_d^\dagger\mathcal{C}^{\phi q(1)}]_{rs} - 3[\Gamma_u\Gamma_u^\dagger\mathcal{C}^{\phi q(1)}]_{rs} + 3[\mathcal{C}^{\phi q(1)}\Gamma_d\Gamma_d^\dagger]_{rs} \right. \\ \left. - 3[\mathcal{C}^{\phi q(1)}\Gamma_u\Gamma_u^\dagger]_{rs} + [\Gamma_d\Gamma_d^\dagger\mathcal{C}^{\phi q(3)}] + [\Gamma_u\Gamma_u^\dagger\mathcal{C}^{\phi q(3)}]_{rs} + [\mathcal{C}^{\phi q(3)}\Gamma_d\Gamma_d^\dagger]_{rs} + [\mathcal{C}^{\phi q(3)}\Gamma_u\Gamma_u^\dagger]_{rs} \right) \\ + 2\gamma_H^{(Y)}[\mathcal{C}^{\phi q(3)}]_{rs} + [\gamma_q^{(Y)}\mathcal{C}^{\phi q(3)}]_{rs} + [\mathcal{C}^{\phi q(3)}\gamma_q^{(Y)}]_{rs} \quad (\text{A.1e})$$

$$[\beta^{u\phi}]_{rs} = - \left(\frac{35}{12}g_1^2 + \frac{27}{4}g_2^2 + 8g_s^2 \right) [\mathcal{C}^{u\phi}]_{rs} - g_1(5g_1^2 - 3g_2^2) [\mathcal{C}^{uB}]_{rs} + g_2(5g_1^2 - 9g_2^2) [\mathcal{C}^{uW}]_{rs} \\ - (3g_2^2 - g_1^2) [\Gamma_u\mathcal{C}^{u\phi}]_{rs} + 4g_1^2[\mathcal{C}^{\phi q(1)}\Gamma_u]_{rs} - 4g_1^2[\mathcal{C}^{\phi q(3)}\Gamma_u]_{rs} - 5g_1[\mathcal{C}^{uB}\Gamma_u^\dagger\Gamma_u + \Gamma_u\Gamma_u^\dagger\mathcal{C}^{uB}]_{rs} \\ - 3g_2[\mathcal{C}^{uW}\Gamma_u^\dagger\Gamma_u - \Gamma_u\Gamma_u^\dagger\mathcal{C}^{uW}]_{rs} - 12g_2[\Gamma_d\Gamma_d^\dagger\mathcal{C}^{uW}]_{rs} - 16g_s[\mathcal{C}^{uG}\Gamma_u^\dagger\Gamma_u + \Gamma_u\Gamma_u^\dagger\mathcal{C}^{uG}]_{rs} \\ + \lambda \left(12[\mathcal{C}^{u\phi}]_{rs} - 2[\mathcal{C}^{\phi q(1)}\Gamma_u]_{rs} + 6[\mathcal{C}^{\phi q(3)}\Gamma_u]_{rs} + 2[\Gamma_u\mathcal{C}^{u\phi}]_{rs} \right) \quad (\text{A.1f}) \\ - 2[\mathcal{C}^{\phi q(1)}\Gamma_u\Gamma_u^\dagger\Gamma_u]_{rs} + 6[\mathcal{C}^{\phi q(3)}\Gamma_d\Gamma_d^\dagger\Gamma_u]_{rs} + 2[\Gamma_u\Gamma_u^\dagger\Gamma_u\mathcal{C}^{u\phi}]_{rs} + 4[\mathcal{C}^{u\phi}\Gamma_u^\dagger\Gamma_u]_{rs} \\ + 5[\Gamma_u\Gamma_u^\dagger\mathcal{C}^{u\phi}]_{rs} - 2[\Gamma_d\Gamma_d^\dagger\mathcal{C}^{u\phi}]_{rs} + 3\gamma_H^{(Y)}[\mathcal{C}^{u\phi}]_{rs} + [\gamma_q^{(Y)}\mathcal{C}^{u\phi}]_{rs} + [\mathcal{C}^{u\phi}\gamma_u^{(Y)}]_{rs}$$

Here, γ^i denote the wavefunction renormalisation constants of the corresponding fields, and Γ_i represent the quark Yukawa matrices. In eq. (A.1) wavefunction renormalisation terms are

$$\begin{aligned}\gamma_H^{(Y)} &= \frac{3}{4}(g_1^2 + 3g_2^2) + \text{Tr} \left(3\Gamma_u \Gamma_u^\dagger + 3\Gamma_d \Gamma_d^\dagger + \Gamma_e \Gamma_e^\dagger \right), \\ [\gamma_q^{(Y)}]_{rs} &= \frac{1}{2}[\Gamma_u \Gamma_u^\dagger]_{rs}, \\ [\gamma_u^{(Y)}]_{rs} &= [\Gamma_u^\dagger \Gamma_u]_{rs}, \\ [\gamma_d^{(Y)}]_{rs} &= [\Gamma_d^\dagger \Gamma_d]_{rs}, \\ [\gamma_e^{(Y)}]_{rs} &= [\Gamma_e^\dagger \Gamma_e]_{rs}.\end{aligned}\tag{A.2}$$

Input Parameters: All SM input parameters at the electroweak scale, used in our analysis, are as follows:

$$\begin{aligned}g_1 &= 0.3576, \quad g_2 = 0.6515, \quad g_s = 1.220, \quad \lambda = 0.2813, \\ m_u &= 1.27 \times 10^{-3}, \quad m_d = 2.7 \times 10^{-3}, \quad m_s = 5.51 \times 10^{-2}, \quad m_c = 0.635, \quad m_b = 2.85,\end{aligned}\tag{A.3}$$

All the light quark masses are given in units of GeV. Different scales used in this works are

$$\mu_{\text{had}} = 2\text{GeV}, \quad \mu_b = 4.18\text{GeV}, \quad \mu_{\text{EW}} = 91.1876 \text{ GeV}, \quad \mu_t = 172.69\text{GeV}, \quad \mu_\Lambda = \mathcal{O}(\text{TeV}).$$

B Loop Contributions

In this section, we present all loop contributions evaluated in our analysis. The loop calculations are cross-verified using the automated MATHEMATICA package **Package-X** [163] and **FeynCalc** [164]. The loop factors are expressed as functions of the renormalisation scale μ . They can subsequently be evolved to other energy scales using the appropriate RGEs, thereby allowing a consistent connection to observables defined at different scales, as discussed earlier. It is worth noting that the loop functions are written in terms of ratios of heavy masses, defined as $x_i \equiv m_i/M_W$, where m_i denotes the mass of the i th particle (quark, gauge boson, or scalar). In some cases, mass ratios of the form $x_{i/j} \equiv m_i/m_j$ are also used.

FCNC Loop Contributions

In this subsection, we present the loop amplitudes associated with the different FCNC processes as discussed in the section 4.1.1, together with their matching expressions, onto the traditional LEFT basis at the scale $\mu = \mu_{\text{EW}}$.

$$\begin{aligned}L_{d_i b}^{d\gamma}(\mu) &= -i \frac{e m_b g_2^2}{16\pi^2 M_W^2} \left[\frac{V_{tb} V_{u_i s}^*(1+x_t) \lambda_R^{u_i t}(\mu) - 2V_{ts}^* V_{u_i b}(1-x_t) \lambda_R^{t u_i *}(\mu)}{8(x_t - 1)} \right. \\ &\quad \left. + \frac{V_{tb} V_{u_i s}^* \lambda_R^{u_i t}(\mu)}{4} \log \left(\frac{\mu^2}{M_W^2} \right) - \frac{V_{tb} V_{u_i s}^* x_t^2 \lambda_R^{u_i t}(\mu)}{4(x_t - 1)^2} \log x_t \right]\end{aligned}\tag{B.1a}$$

$$L_{d_i b}^{dG}(\mu) = -i \frac{g_s m_b g_2^2}{16\pi^2 M_W^2} \left[\frac{V_{tb} V_{u_i s}^* (1+x_t) \xi_R^{u_i t}(\mu) - 2 V_{ts}^* V_{u_i b} (1-x_t) \xi_R^{t u_i *}(\mu)}{8(x_t-1)} \right. \\ \left. + \frac{V_{tb} V_{u_i s}^* \xi_R^{u_i t}(\mu)}{4} \log \left(\frac{\mu^2}{M_W^2} \right) - \frac{V_{tb} V_{u_i s}^* x_t^2 \xi_R^{u_i t}(\mu)}{4(x_t-1)^2} \log x_t \right] \quad (\text{B.1b})$$

$$L_{\mu \mu d_i b}^{V,LL}(\mu) = -\frac{1}{2} \frac{e^2 g_2^2}{16\pi^2 M_W^2} \left[\frac{V_{tb} V_{u_i s}^* \lambda_R^{u_i t}(\mu) - V_{ts}^* V_{u_i b} \lambda_R^{t u_i *}(\mu)}{2(x_t-1)} \log x_t \right] \\ - \frac{g_2^4 g_{Z_L}}{16\pi^2 M_Z^2 \cos^2 \theta_W} \left[\left(V_{tb} V_{u_i s}^* X_L^{u_i t}(\mu) + V_{ts}^* V_{u_i b} X_L^{t u_i *}(\mu) \right) \left\{ \frac{2x_t+3}{16} + \frac{x_t}{8} \log \left(\frac{\mu^2}{m_t^2} \right) \right\} \right] \quad (\text{B.1c})$$

$$L_{\mu \mu d_i b}^{V,LR}(\mu) = -\frac{1}{2} \frac{e^2 g_2^2}{16\pi^2 M_W^2} \left[\frac{V_{tb} V_{u_i s}^* \lambda_R^{u_i t}(\mu) - V_{ts}^* V_{u_i b} \lambda_R^{t u_i *}(\mu)}{2(x_t-1)} \log x_t \right] \\ - \frac{g_2^4 g_{Z_R}}{16\pi^2 M_Z^2 \cos^2 \theta_W} \left[\left(V_{tb} V_{u_i s}^* X_L^{u_i t}(\mu) + V_{ts}^* V_{u_i b} X_L^{t u_i *}(\mu) \right) \left\{ \frac{2x_t+3}{16} + \frac{x_t}{8} \log \left(\frac{\mu^2}{m_t^2} \right) \right\} \right] \quad (\text{B.1d})$$

$$L_{\mu \mu d_i b}^{S,RR}(\mu) = L_{\mu \mu b^2 d_i}^{S,RL*}(\mu) = \frac{1}{2} \frac{m_b m_\mu m_t g_2^2}{16\pi^2 v M_H^2 M_W^2} \left[\frac{V_{tb} V_{u_i s}^* \eta_R^{u_i t}(\mu) + 2 V_{ts}^* V_{u_i b} \eta_R^{t u_i *}(\mu)}{4\sqrt{2}} \log \left(\frac{\mu^2}{m_t^2} \right) \right. \\ \left. + \frac{3 V_{tb} V_{u_i s}^* \eta_R^{u_i t}}{4\sqrt{2}(x_t-1)^2} \log x_t + \frac{V_{tb} V_{u_i s}^* (x_t-7) \eta_R^{u_i t} + 4(x_t-1) V_{ts}^* V_{u_i b} \eta_R^{t u_i *}}{8\sqrt{2}(x_t-1)} \right] \quad (\text{B.1e})$$

$$L_{\nu \nu d_i b}^{V,LL}(\mu) = -\frac{g_2^4 g_{Z_L}}{16\pi^2 M_Z^2 \cos^2 \theta_W} \left[\left(V_{tb} V_{u_i s}^* X_L^{u_i t}(\mu) + V_{ts}^* V_{u_i b} X_L^{t u_i *}(\mu) \right) \left\{ \frac{2x_t+3}{16} + \frac{x_t}{8} \log \left(\frac{\mu^2}{m_t^2} \right) \right\} \right] \quad (\text{B.1f})$$

The couplings of the Z boson with fermions are defined as $g_{Z_L} = (I^3 - Q_f \sin^2 \theta)$ and $g_{Z_R} = -Q_f \sin^2 \theta$, where I^3 and Q_f represent the third component of the isospin and the charge of the fermion, respectively.

FCCC Loop Contributions

In this subsection, we present the loop amplitudes associated with the FCCC processes, as discussed in the section 4.1.2. It is important to note that terms proportional to light quark masses have been neglected, as their contributions are numerically suppressed and can be safely ignored.

$$\begin{aligned}
L_{\nu e b u_i}^{V,LL} = & \frac{g_2^2}{16\sqrt{2}\pi^2 M_W^2 G_F} \left| \frac{V_{tb}}{V_{u_i b}} \right| \left[g_s^2 \left(\frac{5}{6} + \log \frac{\mu^2}{m_t^2} \right) \xi_R^{u_i t} \right. \\
& + e^2 \left(\frac{3}{8(x_t - 1)} \log x_t + \frac{15x_t - 34}{96} + \frac{3x_t - 14}{16} \log \frac{\mu^2}{m_t^2} \right) \lambda_R^{u_i t} \\
& + \frac{3g_2^2}{82\sqrt{2}} \frac{v m_t}{M_W^2} \left(\frac{1}{2} - \frac{\log x_H}{(x_H - 1)(x_t - 1)} - \frac{1}{3} \frac{x_t(x_t - 4)}{(x_H - x_t)(x_t - 1)} \log \frac{x_H}{x_t} + \frac{1}{3} \log \frac{\mu^2}{M_H^2} \right) \eta_R^{u_i t} \\
& + \frac{m_t}{4\sqrt{2}v} \left(1 - \frac{x_H}{(x_H - x_t)} \log \frac{x_H}{x_t} + \log \frac{\mu^2}{m_t^2} \right) \eta_R^{u_i t} \\
& - \frac{g_2^2}{16} \left(2X_L^{u_i t} - 3\kappa_R^{u_i t} \right) \left(\frac{5}{2} + \frac{3 \log x_t}{(x_t - 1)(x_Z - 1)} + \frac{3x_Z^2}{(x_Z - 1)(x_Z - x_t)} \log \frac{x_t}{x_Z} + 3 \log \frac{\mu^2}{m_t^2} \right) \\
& - \frac{(g_1^2 - 3g_2^2)}{16} \left(\frac{3x_Z(x_t X_L^{u_i t} - 2x_Z \kappa_R^{u_i t})}{x_t(x_t - x_Z)} \log \frac{x_t}{x_Z} + \left(\frac{x_t - x_Z}{x_Z} + \frac{x_t - 3x_Z}{x_Z} \log \frac{\mu^2}{m_t^2} \right) X_L^{u_i t} \right. \\
& \left. + 2 \frac{x_t + x_Z}{x_t} \left(1 + 3 \log \frac{\mu^2}{m_t^2} \right) \kappa_R^{u_i t} \right) + \frac{(g_1^2 + 3g_2^2)}{2} \left(-6\kappa_R^{u_i t} + \left(2 \frac{x_t}{x_Z} \left(1 + \log \frac{\mu^2}{m_t^2} \right) + 3 \right) X_L^{u_i t} \right) \left. \right] \quad (B.2a)
\end{aligned}$$

$$\begin{aligned}
L_{\nu e b u_i}^{V,LR} = & \frac{g_2^2}{16\sqrt{2}\pi^2 M_W^2 G_F} \left| \frac{V_{tb}}{V_{u_i b}} \right| \left[\frac{m_b}{m_t} \left(\frac{g_s^2}{12} \left(-1 + 6 \log \frac{\mu^2}{m_t^2} \right) \xi_L^{u_i t} + \frac{e^2}{48} \left(1 - 6 \log \frac{\mu^2}{m_t^2} \right) \lambda_L^{u_i t} \right. \right. \\
& + \frac{g_1^2}{96} \left(\frac{6(x_t X_R^{u_i t} - 2x_Z \kappa_L^{u_i t})}{(x_t - x_Z)} \log \frac{x_t}{x_Z} + \frac{x_t X_R^{u_i t} - 2x_Z \kappa_L^{u_i t}}{x_Z} + \frac{2(x_t X_R^{u_i t} + 6x_Z \kappa_L^{u_i t})}{x_Z} \log \frac{\mu^2}{m_t^2} \right) \left. \right) \\
& + \frac{m_b}{16\sqrt{2}v} \left(\frac{2x_t}{(x_H - x_t)} \log \frac{x_H}{x_t} - \left(1 + 2 \log \frac{\mu^2}{M_H^2} \right) \right) \eta_L^{u_i t} + \frac{g_1^2}{12} \left(\frac{x_t - x_Z}{x_Z} X_R^{u_i t} + 2 \frac{x_t + x_Z}{x_t} \kappa_L^{u_i t} \right. \\
& \left. \left. + 3 \frac{x_Z(x_t X_R^{u_i t} - 2x_Z \kappa_L^{u_i t})}{x_t(x_t - x_Z)} \log \frac{x_t}{x_Z} + \left(\frac{x_t - 3x_Z}{x_Z} X_R^{u_i t} + 6 \frac{x_Z + x_t}{x_t} \kappa_L^{u_i t} \right) \log \frac{\mu^2}{m_t^2} \right) \right] \quad (B.2b)
\end{aligned}$$

Anomalous Wtb coupling

In this subsection, we present the loop amplitudes associated with the anomalous Wtb couplings, as discussed in the section 4.1.2.

$$\begin{aligned}
C_{V_L} = & \frac{V_{u,b}}{8\pi^2} \left[\left(C_F g_s^2 \xi_R^{u_i t} + \frac{e^2}{3} \lambda_R^{u_i t} \right) \left(1 + \frac{3x_t + 1}{4(x_t - 1)} \log \left(-\frac{\mu^2}{m_t^2} \right) - \frac{1}{(x_t - 1)} \log \left(-\frac{\mu^2}{M_W^2} \right) \right) \right. \\
& + \frac{(g_1^2 + 3g_2^2)}{192\pi^2} \left(\left(X_L^{u_i t} + 3\kappa_R^{u_i t} \right) \log \frac{\mu^2}{M_Z^2} - \frac{(x_t + 2)(x_t - x_Z - 1)}{(x_t - 1)^2} X_L^{u_i t} - \frac{4x_t^2 - x_t(3x_Z + 4) - x_Z}{x_t(x_t - 1)} \kappa_R^{u_i t} \right. \\
& \left. \left. \left(+ \frac{(2x_t^2 - 4x_t x_Z - 2x_Z + x_t - 3)}{(x_t - 1)^3} X_L^{u_i t} + 4 \frac{x_t - 2x_Z - 1}{(x_t - 1)^2} \kappa_R^{u_i t} \right) \log(-x_Z) \right) \right. \\
& + e^2 \left(\frac{3x_t + 5}{8(x_t - 1)} - \frac{x_t^2 + 6x_t + 1}{4(x_t - 1)^2} \log(-x_t) \right) \lambda_R^{u_i t} + \frac{g_2^2}{4\sqrt{2} M_W^2} \left(\frac{1}{x_t - 1} + \frac{x_t - x_H + 1}{(x_t - 1)^2} \log x_H \right. \\
& \left. + \frac{M_W^2}{m_t} \frac{(x_t - x_H)(x_t - 1)}{(x_t - 1)^2} \log \frac{x_H}{x_H - x_t} \right) \eta_R^{u_i t} + \frac{g_2^2}{8} \left(\frac{(2x_t^2 X_L^{u_i t} + (3x_t^2 + x_t(5 - 6x_Z) + 2x_Z) \kappa_R^{u_i t}}{x_t(x_t - 1)} \right. \\
& \left. - 2 \frac{(x_t^2 - x_t - x_Z + 2) X_L^{u_i t} + (1 + x_t^2 + x_t(6 - 4x_Z) - 4x_Z + 2x_Z^2) \kappa_R^{u_i t}}{(x_t - 1)^2} \log x_Z \right. \\
& \left. + \frac{2(x_t - x_Z)(X_L^{u_i t} x_t(2 - x_t + x_t^2) + (x_t + x_t^3 - 3x_t^2(x_Z - 2) - x_Z) \kappa_R^{u_i t}}{x_t^2(x_t - 1)^2} \log \frac{x_Z}{x_Z - x_t} \right) \left. \right]
\end{aligned} \tag{B.3}$$

C_{V_R} is light quark mass dependent and gives a small contribution.

Loop contributions to Electroweak Precision Observables

In this subsection, we present the loop amplitudes associated with the different EWPOs as discussed in the section 4.2.

Gauge-boson wavefunction renormalisation The self-energy corrections of the gauge bosons are modified under the NP couplings as

$$\Sigma_{\gamma\gamma}^T(q^2) = -\frac{e^2}{8\pi^2} \left(|\lambda_L^{u_i t}|^2 + |\lambda_R^{u_i t}|^2 \right) q^2 \tag{B.4a}$$

$$\begin{aligned}
\Sigma_{\gamma Z}^T(q^2) = & -\frac{eg_2}{64\pi^2 c_W} \left[\left(X_L^{tu_i *} \lambda_L^{u_i t} + X_R^{tu_i *} \lambda_R^{u_i t} + X_R^{u_i t} \lambda_L^{tu_i *} + X_L^{u_i t} \lambda_R^{tu_i *} \right) \left(1 + 2 \log \frac{\mu^2}{m_t^2} \right) \right. \\
& \left. + 8 \text{Re} \left(\kappa_L^{tu_i *} \lambda_L^{u_i t} + \kappa_R^{tu_i *} \lambda_R^{u_i t} \right) \right] q^2 \tag{B.4b}
\end{aligned}$$

$$\begin{aligned}
\Sigma_{ZZ}^T(q^2) = & -\frac{g_2^2 m_t^2}{64\pi^2 c_W^2} \left(|X_L^{u_i t}|^2 + |X_R^{u_i t}|^2 \right) \left(1 + 2 \log \frac{\mu^2}{m_t^2} \right) \\
& + \frac{g_2^2}{576\pi^2 c_W^2} \left[4 \left(|X_L^{u_i t}|^2 + |X_R^{u_i t}|^2 \right) \left(1 + 3 \log \frac{\mu^2}{m_t^2} \right) - 72 \left(|\kappa_L^{u_i t}|^2 + |\kappa_R^{u_i t}|^2 \right) \right. \\
& \left. - 18 \operatorname{Re} \left(X_L^{tu_i *} \kappa_L^{u_i t} + X_R^{tu_i *} \kappa_L^{u_i t} + X_L^{tu_i *} \kappa_R^{u_i t} + X_R^{tu_i *} \kappa_R^{u_i t} \right) \left(1 + 2 \log \frac{\mu^2}{m_t^2} \right) \right] q^2 \quad (\text{B.4c})
\end{aligned}$$

Z boson modified coupling The modified $Zb\bar{b}$ couplings in the presence of NP can be written as

$$\begin{aligned}
\delta g_{Z,v}^{b,\text{NP}} = -\delta g_{Z,a}^{b,\text{NP}} = & \frac{g_2^2}{32\pi^2} \sum_{u_i=u,c} V_{tb} V_{u_i b}^* \left\{ \operatorname{Re} \left(X_L^{u_i t} \right) \left[\frac{2(5x_Z + 2 - x_t(1 - x_Z))}{x_Z} \right. \right. \\
& + 2x_t \log \frac{\mu^2}{m_t^2} + \frac{2(2 + 3x_Z - 2x_t(1 + x_Z))}{(x_t - 1)x_Z} \log x_t + \frac{2(x_t - x_Z)(x_t - 3x_Z - 2)}{x_Z^2} \log \left(\frac{x_t}{x_t - x_z} \right) \left. \right] \\
& \left. - 8i \operatorname{Im} \left(\kappa_R^{u_i t} \right) \left[1 - \log x_t - \frac{x_t - x_Z}{x_Z} \log \left(\frac{x_t}{x_t - x_Z} \right) \right] \right\} \quad (\text{B.5})
\end{aligned}$$

The expression for $\delta g_Z^{s,\text{NP}}$ will be same $\delta g_Z^{b,\text{NP}}$ with the replacement in the CKM, $V_{tb} V_{u_i b}^* \Leftrightarrow V_{ts} V_{u_i s}^*$.

Loop contributions to Higgs observables

In the section 4.3.1, we discussed various Higgs-related processes that are modified in the presence of top FCNC NP couplings. In this subsection, we present the analytic expressions for the Higgs couplings that receive loop-level corrections induced by these NP interactions.

$$\begin{aligned}
C_L^{H,\text{NP}} = & \sum_{u_i=u,c} \frac{g_2^2 m_b m_t}{128\sqrt{2}\pi^2 M_H^2} V_{tb} V_{u_i b}^* \left(-8(x_H + 1)\eta_R^{u_i t} + \frac{8 - x_H(x_t - 3) - 8x_t\eta_R^{tu_i *}}{x_t - 1} \right. \\
& - 2x_H(2\eta_R^{u_i t} + \eta_R^{tu_i *}) \log \frac{\mu^2}{m_t^2} + 2 \left(4\eta_R^{u_i t} - \frac{4x_t + x_H - 4}{(x_t - 1)^2} \eta_R^{tu_i *} \right) \log x_t \quad (\text{B.6a}) \\
& \left. - \frac{4(x_H + x_t)((2 + x_H)\eta_R^{u_i t} + 2\eta_R^{tu_i *})}{x_H} \log \frac{x_t}{x_t + x_H} \right)
\end{aligned}$$

$$\begin{aligned}
C_R^{H,\text{NP}} = & \sum_{u_i=u,c} \frac{g_2^2 m_b m_t}{128\sqrt{2}\pi^2 M_H^2} V_{tb} V_{u_i b}^* \left(\left(8 + x_H \frac{x_t - 3}{x_t - 1} \right) \eta_R^{u_i t} + 8(1 + x_H)\eta_R^{tu_i *} \right. \\
& + 2x_H(\eta_R^{u_i t} + 2\eta_R^{tu_i *}) \log \frac{\mu^2}{m_t^2} - 2 \left(4\eta_R^{tu_i *} - \frac{4x_t + x_H - 4}{(x_t - 1)^2} \eta_R^{u_i t} \right) \log x_t \quad (\text{B.6b}) \\
& \left. + \frac{4(x_H + x_t)((2 + x_H)\eta_R^{tu_i *} + 2\eta_R^{u_i t})}{x_H} \log \frac{x_t}{x_t + x_H} \right)
\end{aligned}$$

$$\delta_{\gamma\gamma} = \frac{1}{12\sqrt{2}\pi^2 m_t v} \left(2i \operatorname{Im} \left(\eta_L^{tu_i*} \lambda_L^{u_i t} + \eta_R^{tu_i*} \lambda_R^{u_i t} \right) \left(\log \frac{\mu^2}{m_t^2} + \log \frac{m_t^2}{m_t^2 - M_H^2} \right) \right. \\ \left. - 2i \operatorname{Im} \left(\eta_L^{u_i t} \lambda_L^{tu_i*} + \eta_R^{u_i t} \lambda_R^{tu_i*} \right) + \frac{3\sqrt{2}m_t}{v} \left(|\lambda_L^{u_i t}|^2 + |\lambda_R^{u_i t}|^2 \right) \right) \quad (\text{B.6c})$$

$$\delta_{\gamma Z} = \frac{1}{192\pi^2 v^2 m_t} \left[\left(-2\sqrt{2} iv \frac{5g_1^2 - 3g_2^2}{g_1 g_2} \operatorname{Im} \left(\eta_L^{tu_i*} \lambda_L^{u_i t} + \eta_R^{tu_i*} \lambda_R^{u_i t} \right) + 6i \frac{m_t}{g_1 g_2} \operatorname{Im} \left(X_R^{tu_i*} \lambda_L^{u_i t} + X_L^{tu_i*} \lambda_R^{u_i t} \right) \right. \right. \\ \left. \left. + 4\sqrt{2}e^2 g_1 g_2 \left(2i \operatorname{Im} \left(\eta_L^{tu_i*} \kappa_L^{u_i t} + \eta_R^{tu_i*} \kappa_R^{u_i t} \right) - \left(\eta_L^{u_i t} \kappa_L^{tu_i*} + \eta_R^{u_i t} \kappa_R^{tu_i*} \right) \right) \right) \left(1 + \log \frac{\mu^2}{m_t^2} \right) \right. \\ \left. + \frac{24m_t}{g_1 g_2} \operatorname{Re} \left(\kappa_L^{tu_i*} \lambda_L^{u_i t} + \kappa_R^{tu_i*} \lambda_R^{u_i t} \right) + \left(2\sqrt{2}i v \frac{(5g_1^2 - 3g_2^2)}{g_1 g_2} \operatorname{Im} \left(\eta_L^{tu_i*} \lambda_L^{u_i t} + \eta_R^{tu_i*} \lambda_R^{u_i t} \right) \right. \right. \\ \left. \left. - 4\sqrt{2}e^2 g_1 g_2 \left(2i \operatorname{Im} \left(\eta_L^{tu_i*} \kappa_L^{u_i t} + \eta_R^{tu_i*} \kappa_R^{u_i t} \right) - \left(\eta_L^{u_i t} \kappa_L^{tu_i*} + \eta_R^{u_i t} \kappa_R^{tu_i*} \right) \right) \right) \log \frac{m_t^2}{m_t^2 - M_H^2} \right] \quad (\text{B.6d})$$

$$\delta_{gg} = \frac{1}{8\sqrt{2}\pi^2 m_t v} \left(i \operatorname{Im} \left(\eta_L^{tu_i*} \xi_L^{u_i t} + \eta_R^{tu_i*} \xi_R^{u_i t} \right) \left(\log \frac{\mu^2}{m_t^2} + \log \frac{m_t^2}{m_t^2 - M_H^2} \right) \right. \\ \left. - i \operatorname{Im} \left(\eta_L^{u_i t} \xi_L^{tu_i*} + \eta_R^{u_i t} \xi_R^{tu_i*} \right) + \frac{\sqrt{2}m_t}{v} \left(|\xi_L^{u_i t}|^2 + |\xi_R^{u_i t}|^2 \right) \right) \quad (\text{B.6e})$$

C EDM and CEDM Contributions

In this section, we present the loop contributions to the EDMs and CEDMs of both light and heavy quarks. As discussed in the main text, these loop calculations are performed at the electroweak scale, μ_{EW} , and subsequently evolved down to the hadronic scale, μ_{had} , using the appropriate RGEs.

$$\begin{aligned}
\frac{d_{u_i}}{e}(\mu) = & \sum_j \frac{g_2^2 V_{td_j} V_{u_i d_j}^*}{32\pi^2} \frac{m_{u_i}}{m_t^2} \left[\frac{5x_{d_j}^2 - 5x_{d_j} - 6}{2(x_{d_j} - 1)} + 3x_{d_j} \log \left(\frac{\mu^2}{m_{d_j}^2} \right) + 3 \frac{x_{d_j} \log(x_{d_j})}{(x_{d_j} - 1)^2} \right] \text{Re} \left(\lambda_R^{u_i t} \right) , \\
& + \frac{q_{u_i}}{16\pi^2 m_t} \left\{ C_F g_s^2(\mu) \text{Im} \left(\xi_L^{u_i t} \xi_R^{tu_i *} \right) \log \left(\frac{\mu^2}{m_t^2} \right) + e^2 \text{Im} \left(\lambda_L^{u_i t} \lambda_R^{tu_i *} \right) \log \left(\frac{\mu^2}{m_t^2} \right) \right\} , \quad (\text{C.1a}) \\
& + \frac{q_{u_i}}{32\pi^2 M_H^2} \left\{ \frac{(x_{t/H} - 3)}{2(x_{t/H} - 1)^2} + \frac{\log x_{t/H}}{(x_{t/H} - 1)^3} \right\} \text{Im} \left(\eta_L^{u_i t} \eta_R^{tu_i *} \right) , \\
& + \frac{g_2^2}{16\pi^2 c_W^2} \frac{q_{u_i}}{m_t} \left[\text{Im} \left(\kappa_L^{u_i t} X_L^{tu_i *} + X_R^{u_i t} \kappa_R^{tu_i *} + \kappa_L^{u_i t} \kappa_R^{tu_i *} \right) \log \left(\frac{\mu^2}{m_t^2} \right) , \right. \\
& + \frac{\log x_t}{4(x_{t/Z} - 1)^2} \left\{ x_{t/Z}^2 \text{Im} \left(2X_L^{tu_i *} X_R^{u_i t} + X_L^{u_i t} \kappa_L^{tu_i *} + X_R^{tu_i *} \kappa_R^{u_i t} \right) , \right. \\
& + 2 \text{Im} \left(X_L^{u_i t} \kappa_L^{tu_i *} + X_R^{tu_i *} \kappa_R^{u_i t} + \kappa_L^{u_i t} \kappa_R^{tu_i *} \right) \\
& + x_{t/Z} \text{Im} \left(2X_L^{tu_i *} X_R^{u_i t} + 9(X_L^{tu_i *} \kappa_L^{u_i t} + X_R^{u_i t} \kappa_R^{tu_i *}) + 10\kappa_L^{u_i t} \kappa_R^{tu_i *} \right) \left. \right\} , \\
& + \frac{\log x_{t/Z}}{2(x_{t/Z} - 1)^3} \left\{ 2x_{t/Z}^2 \text{Im} \left(X_L^{tu_i *} X_R^{u_i t} \right) + x_{t/Z} \text{Im} \left(5(X_L^{tu_i *} \kappa_L^{tu_i *} + X_R^{tu_i *} \kappa_R^{u_i t}) + 8\kappa_L^{u_i t} \kappa_R^{tu_i *} \right) , \right. \\
& \left. \left. + 2 \text{Im} \left(X_L^{u_i t} \kappa_L^{tu_i *} + X_R^{tu_i *} \kappa_R^{u_i t} + \kappa_L^{tu_i *} \kappa_R^{u_i t} \right) \right\} \right] \\
w(\mu) = & \frac{g_s^3(\mu)}{(32\pi^2)^2 M_H^2} \left\{ -\frac{x_{t/H}^2 - 5x_{t/H} - 2}{3(x_{t/H} - 1)^2} - \frac{2x_{t/H}}{(x_{t/H} - 1)^4} \log x_{t/H} \right\} \text{Im} \left(\eta_L^{ct} \eta_R^{tc *} \right) \quad (\text{C.1b})
\end{aligned}$$

Here, d_j represents the down-type quarks of the three generations, and the factors x_i are defined as $x_{d_j} = m_{d_j}^2/M_W^2$, $x_{t/Z} = m_t^2/M_Z^2$, and $x_{t/H} = m_t^2/M_H^2$, respectively. The loop contribution of the Weinberg operator in eq. (C.1b) is only relevant for the charm-quark CEDM. The expression for the CEDM, \tilde{d}_{u_i} , of up- and charm-type quarks is structurally analogous to that of the EDM, (d_{u_i}/e) , apart from a few key modifications. Specifically, for the topologies shown in fig. 14d–14f, corresponding to two insertions of the NP couplings, the electric charge of the up quark ($q_{u_i} = 2/3$) does not contribute. In the case of fig. 14d, the color factor $C_F = 4/3$ in the EDM expression is replaced by $-1/(2N)$ for the CEDM. Moreover, for the single-insertion diagrams depicted in fig. 14a–14b, the factor $\text{Re} \left(\lambda_R^{u_i t} \right)$ appearing in the EDM expression must be replaced by $\text{Re} \left(\xi_R^{u_i t} \right)$ in the CEDM case.

$$\frac{d_{d_i}}{e}(\mu) = \frac{g_2^2 m_{d_i}}{32\pi^2 M_W^2} V_{td_i} \left(V_{cd_i}^* \text{Re} \left(\lambda_R^{ct} \right) + V_{ud_i}^* \text{Re} \left(\lambda_R^{ut} \right) \right) \left\{ \frac{1}{(x_t - 1)} + \frac{x_t}{(x_t - 1)^2} \log x_t \right\} \quad (\text{C.2a})$$

$$\frac{\tilde{d}_{d_i}}{g_s}(\mu) = \frac{g_2^2 m_{d_i}}{32\pi^2 M_W^2} V_{td_i} \left(V_{cd_i}^* \text{Re} \left(\xi_R^{ct} \right) + V_{ud_i}^* \text{Re} \left(\xi_R^{ut} \right) \right) \left\{ \frac{1}{(x_t - 1)} + \frac{x_t}{(x_t - 1)^2} \log x_t \right\} \quad (\text{C.2b})$$

In the above equation, the loop calculations for the down and strange quarks have been performed at the electroweak scale, μ_{EW} .

Top quark CMDM Top quark CMDM in the presence of NP modified as,

$$\begin{aligned} \hat{\mu}_t^{\text{NP}} = & \sum_{i,j} \frac{g_2^2 m_t}{64\pi^2 M_W^2} V_{td_j} V_{u_i d_j} \left(-m_{u_i} \text{Im}(\xi_L^{u_i t}) + m_t \text{Im}(\xi_R^{u_i t}) \right) \left(\frac{2x_t^2 - x_t - 2}{x_t^2} + \log \frac{\mu^2}{M_W^2} \right. \\ & \left. + \frac{(x_t - 1)^2(x_t + 2)}{x_t^3} \log \frac{M_W^2}{M_W^2 - m_t^2} \right) \end{aligned} \quad (\text{C.3a})$$

$$\begin{aligned} \hat{d}_t^{\text{NP}} = & \sum_{i,j} \frac{g_2^2 m_t}{64\pi^2 M_W^2} V_{td_j} V_{u_i d_j} \left(m_{u_i} \text{Re}(\xi_L^{u_i t}) + m_t \text{Re}(\xi_R^{u_i t}) \right) \left(\frac{2x_t^2 - x_t - 2}{x_t^2} + \log \frac{\mu^2}{M_W^2} \right. \\ & \left. + \frac{(x_t - 1)^2(x_t + 2)}{x_t^3} \log \frac{M_W^2}{M_W^2 - m_t^2} \right) \end{aligned} \quad (\text{C.3b})$$

Here, d_j represents the down-type quarks of the three generations and u_i corresponds to up and charm quark respectively.

D Correlation Matrices

In this section, we present the correlation matrices among the various top FCNC couplings obtained from the global fit, which is presented in the section 5.

Coupling	Re(ξ_L^{ct})	Im(ξ_L^{ct})	Re(ξ_R^{ct})	Im(ξ_R^{ct})	Coupling	Re(ξ_L^{ut})	Im(ξ_L^{ut})	Re(ξ_R^{ut})	Im(ξ_R^{ut})
Re(ξ_L^{ct})	1.0	0.511	-0.051	0.006	Re(ξ_L^{ut})	1.0	-0.702	-0.745	0.142
Im(ξ_L^{ct})		1.0	-0.026	0.003	Im(ξ_L^{ut})		1.0	0.511	-0.103
Re(ξ_R^{ct})			1.0	-0.112	Re(ξ_R^{ut})			1.0	-0.240
Im(ξ_R^{ct})				1.0	Im(ξ_R^{ut})				1.0

Table 15. Correlation matrices of the complex top–gluon FCNC dipole couplings at the scale μ_{EW} .

Coupling	Re(λ_L^{ct})	Im(λ_L^{ct})	Re(λ_R^{ct})	Im(λ_R^{ct})	Coupling	Re(λ_L^{ut})	Im(λ_L^{ut})	Re(λ_R^{ut})	Im(λ_R^{ut})
Re(λ_L^{ct})	1.0	-0.137	0.0	0.0	Re(λ_L^{ut})	1.0	0.004	0.004	0.0
Im(λ_L^{ct})		1.0	-0.0	-0.0	Im(λ_L^{ut})		1.0	0.0	0.0
Re(λ_R^{ct})			1.0	0.036	Re(λ_R^{ut})			1.0	0.108
Im(λ_R^{ct})				1.0	Im(λ_R^{ut})				1.0

Table 16. Correlation matrices of the complex top–photon FCNC dipole couplings $\lambda_{L,R}^{ct}$ and $\lambda_{L,R}^{ut}$ at the scale μ_{EW} .

Coupling	Re(κ_L^{ct})	Im(κ_L^{ct})	Re(κ_R^{ct})	Im(κ_R^{ct})	Coupling	Re(κ_L^{ut})	Im(κ_L^{ut})	Re(κ_R^{ut})	Im(κ_R^{ut})
Re(κ_L^{ct})	1.0	0.268	0.023	-0.062	Re(κ_L^{ut})	1.0	0.110	0.687	0.063
Im(κ_L^{ct})		1.0	-0.022	0.060	Im(κ_L^{ut})		1.0	0.067	0.896
Re(κ_R^{ct})			1.0	0.762	Re(κ_R^{ut})			1.0	-0.141
Im(κ_R^{ct})				1.0	Im(κ_R^{ut})				1.0

Table 17. Correlation matrices of the complex top– Z boson FCNC dipole couplings $\kappa_{L,R}^{ct}$ and $\kappa_{L,R}^{ut}$ at the scale μ_{EW} .

Coupling	Re(η_L^{ut})	Im(η_L^{ut})	Re(ξ_L^{ut})	Im(ξ_L^{ut})	Coupling	Re(η_R^{ut})	Im(η_R^{ut})	Re(ξ_R^{ut})	Im(ξ_R^{ut})
Re(η_L^{ut})	1.0	-0.632	-0.120	-0.366	Re(η_R^{ut})	1.0	0.520	-0.726	0.140
Im(η_L^{ut})		1.0	0.668	0.367	Im(η_R^{ut})		1.0	0.185	-0.058
Re(ξ_L^{ut})			1.0	0.469	Re(ξ_R^{ut})			1.0	-0.031
Im(ξ_L^{ut})				1.0	Im(ξ_R^{ut})				1.0

Table 18. Correlation matrices of the top–Higgs (η^{ut}) and top–gluon (ξ^{ut}) FCNC couplings at the scale μ_{EW} .

Coupling	Re(η_L^{ct})	Im(η_L^{ct})	Re(ξ_L^{ct})	Im(ξ_L^{ct})	Coupling	Re(η_R^{ct})	Im(η_R^{ct})	Re(ξ_R^{ct})	Im(ξ_R^{ct})
Re(η_L^{ct})	1.0	-0.345	0.631	0.441	Re(η_R^{ct})	1.0	0.993	-0.025	-0.002
Im(η_L^{ct})		1.0	-0.492	0.295	Im(η_R^{ct})		1.0	-0.001	-0.005
Re(ξ_L^{ct})			1.0	0.658	Re(ξ_R^{ct})			1.0	0.515
Im(ξ_L^{ct})				1.0	Im(ξ_R^{ct})				1.0

Table 19. Correlation matrices of the top–Higgs (η^{ct}) and top–gluon (ξ^{ct}) FCNC couplings at the scale μ_{EW} .

E SMEFT Couplings

In this section, we present the fitted values of the SMEFT couplings \mathcal{C}_{3i} , which correspond to the left-chiral components of the top–FCNC effective interactions.

Real SMEFT Couplings (μ_{EW})			
Coupling	Value (GeV $^{-2}$)	Coupling	Value (GeV $^{-2}$)
$\mathcal{C}_{32}^{uG} \times 10^6$	(2.68 ± 3.43)	$\mathcal{C}_{31}^{uG} \times 10^6$	(-1.75 ± 4.78)
$\mathcal{C}_{32}^{uB} \times 10^6$	(-3.28 ± 3.6)	$\mathcal{C}_{31}^{uB} \times 10^6$	(-2.37 ± 2.37)
$\mathcal{C}_{32}^{uW} \times 10^6$	(-3.5 ± 3.0)	$\mathcal{C}_{31}^{uW} \times 10^6$	(-1.5 ± 1.5)
$\mathcal{C}_{32}^{u\phi} \times 10^5$	(-1.16 ± 14.3)	$\mathcal{C}_{31}^{u\phi} \times 10^5$	(1.64 ± 5.81)

Table 20. Fit result for the top FCNC SMEFT WCs in the real scenario.

References

- [1] TOP QUARK WORKING GROUP collaboration, *Working Group Report: Top Quark*, in *Snowmass 2013: Snowmass on the Mississippi*, 11, 2013 [[1311.2028](#)].
- [2] ATLAS collaboration, *Climbing to the Top of the ATLAS 13 TeV data*, *Phys. Rept.* **1116** (2025) 127 [[2404.10674](#)].
- [3] J.A. Aguilar-Saavedra, *A Minimal set of top anomalous couplings*, *Nucl. Phys. B* **812** (2009) 181 [[0811.3842](#)].
- [4] S. Bißmann, J. Erdmann, C. Grunwald, G. Hiller and K. Kröninger, *Constraining top-quark couplings combining top-quark and B decay observables*, *Eur. Phys. J. C* **80** (2020) 136 [[1909.13632](#)].
- [5] J.A. Aguilar-Saavedra and B.M. Nobre, *Rare top decays $t \rightarrow c$ gamma, $t \rightarrow cg$ and CKM unitarity*, *Phys. Lett. B* **553** (2003) 251 [[hep-ph/0210360](#)].
- [6] A. Cordero-Cid, M.A. Perez, G. Tavares-Velasco and J.J. Toscano, *Effective Lagrangian approach to Higgs-mediated FCNC top quark decays*, *Phys. Rev. D* **70** (2004) 074003 [[hep-ph/0407127](#)].
- [7] L. Allwicher, C. Cornella, G. Isidori and B.A. Stefanek, *New physics in the third generation. A comprehensive SMEFT analysis and future prospects*, *JHEP* **03** (2024) 049 [[2311.00020](#)].
- [8] F. Garosi, D. Marzocca, A.R. Sánchez and A. Stanzione, *Indirect constraints on top quark operators from a global SMEFT analysis*, *JHEP* **12** (2023) 129 [[2310.00047](#)].
- [9] J. Drobniak, S. Fajfer and J.F. Kamenik, *Signatures of NP models in top FCNC decay $t \rightarrow c(u) l+ l-$* , *JHEP* **03** (2009) 077 [[0812.0294](#)].
- [10] M. Forslund and N. Kidonakis, *Associated production of a top quark with a photon via anomalous couplings*, *Phys. Rev. D* **98** (2018) 074017 [[1808.09014](#)].
- [11] M. Chala, J. Santiago and M. Spannowsky, *Constraining four-fermion operators using rare top decays*, *JHEP* **04** (2019) 014 [[1809.09624](#)].
- [12] S. Bißmann, C. Grunwald, G. Hiller and K. Kröninger, *Top and Beauty synergies in SMEFT-fits at present and future colliders*, *JHEP* **06** (2021) 010 [[2012.10456](#)].
- [13] S. Bhattacharya, S. Jahedi, S. Nandi and A. Sarkar, *Probing flavor constrained SMEFT operators through tc production at the muon collider*, *JHEP* **07** (2024) 061 [[2312.14872](#)].

- [14] W. Altmannshofer, S. Gori, B.V. Lehmann and J. Zuo, *UV physics from IR features: New prospects from top flavor violation*, *Phys. Rev. D* **107** (2023) 095025 [[2303.00781](#)].
- [15] S. Kala, L. Kolay, L. Mukherjee and S. Nandi, *Constraining anomalous Wtb and related SMEFT couplings using low-energy and electroweak precision observables*, [2505.07926](#).
- [16] J.J. Cao, G. Eilam, M. Frank, K. Hikasa, G.L. Liu, I. Turan et al., *SUSY-induced FCNC top-quark processes at the large hadron collider*, *Phys. Rev. D* **75** (2007) 075021 [[hep-ph/0702264](#)].
- [17] J. Guasch and J. Sola, *FCNC top quark decays: A Door to SUSY physics in high luminosity colliders?*, *Nucl. Phys. B* **562** (1999) 3 [[hep-ph/9906268](#)].
- [18] M. Frank, B. Fuks, S.K. Garg and P. Poulose, *Flavour-changing top quark decays in the alternative left-right model*, *Phys. Lett. B* **850** (2024) 138548 [[2312.12523](#)].
- [19] F.-M. Cai, S. Funatsu, X.-Q. Li and Y.-D. Yang, *Rare top-quark decays $t \rightarrow cg(g)$ in the aligned two-Higgs-doublet model*, *Eur. Phys. J. C* **82** (2022) 881 [[2202.08091](#)].
- [20] K. Fuyuto, W.-S. Hou and M. Kohda, *Z' -induced FCNC decays of top, beauty, and strange quarks*, *Phys. Rev. D* **93** (2016) 054021 [[1512.09026](#)].
- [21] S. Cho, P. Ko, J. Lee, Y. Omura and C. Yu, *Top FCNC induced by a Z' boson*, *Phys. Rev. D* **101** (2020) 055015 [[1910.05925](#)].
- [22] P.Q. Hung, Y.-X. Lin, C.S. Nugroho and T.-C. Yuan, *Top Quark Rare Decays via Loop-Induced FCNC Interactions in Extended Mirror Fermion Model*, *Nucl. Phys. B* **927** (2018) 166 [[1709.01690](#)].
- [23] A. Jueid and S. Kanemura, *Dark matter as the trigger of flavor changing neutral current decays of the top quark*, *Phys. Rev. D* **110** (2024) 095009 [[2402.08652](#)].
- [24] S. Bhattacharya, L. Kolay, D. Pradhan and A. Sarkar, *Up-type FCNC in presence of Dark Matter*, [2504.20045](#).
- [25] Y. Liu, B. Yan and R. Zhang, *Loop induced top quark FCNC through top quark and dark matter interactions*, *Phys. Lett. B* **827** (2022) 136964 [[2103.07859](#)].
- [26] C.-H. Chen and T. Nomura, *Scotogenic top-quark FCNC decays*, *Phys. Rev. D* **106** (2022) 095005 [[2204.01214](#)].
- [27] C.-H. Chen, C.-W. Chiang and C.-W. Su, *Top-quark FCNC decays, LFVs, lepton $g - 2$, and W mass anomaly with inert charged Higgses*, *J. Phys. G* **51** (2024) 085001 [[2301.07070](#)].
- [28] ATLAS collaboration, *Search for flavor-changing neutral-current couplings between the top quark and the Z boson with proton-proton collisions at $s=13$ TeV with the ATLAS detector*, *Phys. Rev. D* **108** (2023) 032019 [[2301.11605](#)].
- [29] ATLAS collaboration, *Search for flavour-changing neutral-current couplings between the top quark and the photon with the ATLAS detector at $s=13$ TeV*, *Phys. Lett. B* **842** (2023) 137379 [[2205.02537](#)].
- [30] ATLAS collaboration, *Search for flavour-changing neutral-current couplings between the top quark and the Higgs boson in multi-lepton final states in 13 TeV pp collisions with the ATLAS detector*, *Eur. Phys. J. C* **84** (2024) 757 [[2404.02123](#)].
- [31] ATLAS collaboration, *Search for flavour-changing neutral-current interactions of a top quark and a gluon in pp collisions at $\sqrt{s} = 13$ TeV with the ATLAS detector*, *Eur. Phys. J. C* **82** (2022) 334 [[2112.01302](#)].

[32] CMS collaboration, *Search for flavor changing neutral current interactions of the top quark in final states with a photon and additional jets in proton-proton collisions at $s=13$ TeV*, *Phys. Rev. D* **109** (2024) 072004 [[2312.08229](#)].

[33] CMS collaboration, *Search for associated production of a Z boson with a single top quark and for tZ flavour-changing interactions in pp collisions at $\sqrt{s} = 8$ TeV*, *JHEP* **07** (2017) 003 [[1702.01404](#)].

[34] M. Malekhosseini, M. Ghominejad, H. Khanpour and M. Mohammadi Najafabadi, *Constraining top quark flavor violation and dipole moments through three and four-top quark productions at the LHC*, *Phys. Rev. D* **98** (2018) 095001 [[1804.05598](#)].

[35] D. Atwood, L. Reina and A. Soni, *Phenomenology of two Higgs doublet models with flavor changing neutral currents*, *Phys. Rev. D* **55** (1997) 3156 [[hep-ph/9609279](#)].

[36] O. Cakir, I.T. Cakir, A. Senol and A.T. Tasci, *Search for Top Quark FCNC Couplings in Z' Models at the LHC and CLIC*, *Eur. Phys. J. C* **70** (2010) 295 [[1003.3156](#)].

[37] B. Grzadkowski, M. Iskrzynski, M. Misiak and J. Rosiek, *Dimension-Six Terms in the Standard Model Lagrangian*, *JHEP* **10** (2010) 085 [[1008.4884](#)].

[38] S. Banerjee, M. Chala and M. Spannowsky, *Top quark FCNCs in extended Higgs sectors*, *Eur. Phys. J. C* **78** (2018) 683 [[1806.02836](#)].

[39] G. Cacciapaglia, G. Ferretti, T. Flacke and H. Serôdio, *Light scalars in composite Higgs models*, *Front. in Phys.* **7** (2019) 22 [[1902.06890](#)].

[40] B.-F. Hou, X.-Q. Li, Y.-D. Yang, X.-B. Yuan and M.-W. Zhang, *Phenomenological anatomy of top-quark FCNCs induced by a light scalar singlet*, *JHEP* **07** (2025) 208 [[2501.07341](#)].

[41] R. Alonso, E.E. Jenkins, A.V. Manohar and M. Trott, *Renormalization Group Evolution of the Standard Model Dimension Six Operators III: Gauge Coupling Dependence and Phenomenology*, *JHEP* **04** (2014) 159 [[1312.2014](#)].

[42] E.E. Jenkins, A.V. Manohar and M. Trott, *Renormalization Group Evolution of the Standard Model Dimension Six Operators II: Yukawa Dependence*, *JHEP* **01** (2014) 035 [[1310.4838](#)].

[43] E.E. Jenkins, A.V. Manohar and P. Stoffer, *Low-Energy Effective Field Theory below the Electroweak Scale: Operators and Matching*, *JHEP* **03** (2018) 016 [[1709.04486](#)].

[44] W. Dekens and P. Stoffer, *Low-energy effective field theory below the electroweak scale: matching at one loop*, *JHEP* **10** (2019) 197 [[1908.05295](#)].

[45] E.E. Jenkins, A.V. Manohar and M. Trott, *Renormalization Group Evolution of the Standard Model Dimension Six Operators I: Formalism and lambda Dependence*, *JHEP* **10** (2013) 087 [[1308.2627](#)].

[46] J. Aebischer, M. Fael, C. Greub and J. Virto, *B physics Beyond the Standard Model at One Loop: Complete Renormalization Group Evolution below the Electroweak Scale*, *JHEP* **09** (2017) 158 [[1704.06639](#)].

[47] K.G. Chetyrkin, M. Misiak and M. Munz, *Weak radiative B meson decay beyond leading logarithms*, *Phys. Lett. B* **400** (1997) 206 [[hep-ph/9612313](#)].

[48] A.J. Buras, *Weak Hamiltonian, CP violation and rare decays*, in *Les Houches Summer School in Theoretical Physics, Session 68: Probing the Standard Model of Particle Interactions*, pp. 281–539, 6, 1998 [[hep-ph/9806471](#)].

[49] M. González-Alonso, J. Martin Camalich and K. Mimouni, *Renormalization-group evolution of new physics contributions to (semi)leptonic meson decays*, *Phys. Lett. B* **772** (2017) 777 [[1706.00410](#)].

[50] F. Mahmoudi and Y. Monceaux, *Overview of $B \rightarrow K^{(*)}\ell\ell$ Theoretical Calculations and Uncertainties*, *Symmetry* **16** (2024) 1006 [[2408.03235](#)].

[51] BELLE collaboration, *Evidence for Isospin Violation and Measurement of CP Asymmetries in $B \rightarrow K^*(892)\gamma$* , *Phys. Rev. Lett.* **119** (2017) 191802 [[1707.00394](#)].

[52] BELLE-II collaboration, *Measurement of branching fractions, CP asymmetry, and isospin asymmetry for $B \rightarrow \rho\gamma$ decays using Belle and Belle II data*, [2407.08984](#).

[53] BELLE collaboration, *Search for $B_s^0 \rightarrow \gamma\gamma$ and a measurement of the branching fraction for $B_s^0 \rightarrow \phi\gamma$* , *Phys. Rev. D* **91** (2015) 011101 [[1411.7771](#)].

[54] HEAVY FLAVOR AVERAGING GROUP (HFLAV) collaboration, *Averages of b -hadron, c -hadron, and τ -lepton properties as of 2023*, [2411.18639](#).

[55] M. Misiak, A. Rehman and M. Steinhauser, *Towards $\bar{B} \rightarrow X_s\gamma$ at the NNLO in QCD without interpolation in m_c* , *JHEP* **06** (2020) 175 [[2002.01548](#)].

[56] A. Paul and D.M. Straub, *Constraints on new physics from radiative B decays*, *JHEP* **04** (2017) 027 [[1608.02556](#)].

[57] M. Beneke, T. Feldmann and D. Seidel, *Systematic approach to exclusive $B \rightarrow Vl^+l^-$, $V\gamma$ decays*, *Nucl. Phys. B* **612** (2001) 25 [[hep-ph/0106067](#)].

[58] A. Bharucha, D.M. Straub and R. Zwicky, *$B \rightarrow Vl^+l^-$ in the Standard Model from light-cone sum rules*, *JHEP* **08** (2016) 098 [[1503.05534](#)].

[59] D. Becirevic, N. Kosnik, F. Mescia and E. Schneider, *Complementarity of the constraints on New Physics from $B_s \rightarrow \mu^+\mu^-$ and from $B \rightarrow Kl^+l^-$ decays*, *Phys. Rev. D* **86** (2012) 034034 [[1205.5811](#)].

[60] C. Bobeth, M. Misiak and J. Urban, *Photonic penguins at two loops and m_t dependence of $BR[B \rightarrow X_s l^+l^-]$* , *Nucl. Phys. B* **574** (2000) 291 [[hep-ph/9910220](#)].

[61] W. Altmannshofer, P. Ball, A. Bharucha, A.J. Buras, D.M. Straub and M. Wick, *Symmetries and Asymmetries of $B \rightarrow K^*\mu^+\mu^-$ Decays in the Standard Model and Beyond*, *JHEP* **01** (2009) 019 [[0811.1214](#)].

[62] J. Aebischer, A. Crivellin, M. Fael and C. Greub, *Matching of gauge invariant dimension-six operators for $b \rightarrow s$ and $b \rightarrow c$ transitions*, *JHEP* **05** (2016) 037 [[1512.02830](#)].

[63] LHCb collaboration, *Measurement of the CP asymmetry in $B^+ \rightarrow K^+\mu^+\mu^-$ decays*, *Phys. Rev. Lett.* **111** (2013) 151801 [[1308.1340](#)].

[64] LHCb collaboration, *Differential branching fractions and isospin asymmetries of $B \rightarrow K^{(*)}\mu^+\mu^-$ decays*, *JHEP* **06** (2014) 133 [[1403.8044](#)].

[65] LHCb collaboration, *Test of lepton universality using $B^+ \rightarrow K^+\ell^+\ell^-$ decays*, *Phys. Rev. Lett.* **113** (2014) 151601 [[1406.6482](#)].

[66] LHCb collaboration, *Angular analysis of the $B^0 \rightarrow K^{*0}\mu^+\mu^-$ decay using 3 fb^{-1} of integrated luminosity*, *JHEP* **02** (2016) 104 [[1512.04442](#)].

[67] LHCb collaboration, *Angular Analysis of the $B^+ \rightarrow K^{*+}\mu^+\mu^-$ Decay*, *Phys. Rev. Lett.* **126** (2021) 161802 [[2012.13241](#)].

[68] LHCb collaboration, *Branching Fraction Measurements of the Rare $B_s^0 \rightarrow \phi \mu^+ \mu^-$ and $B_s^0 \rightarrow f_2'(1525) \mu^+ \mu^-$ Decays*, *Phys. Rev. Lett.* **127** (2021) 151801 [[2105.14007](#)].

[69] LHCb collaboration, *Test of lepton universality in $b \rightarrow s \ell^+ \ell^-$ decays*, *Phys. Rev. Lett.* **131** (2023) 051803 [[2212.09152](#)].

[70] Belle collaboration, *Lepton-Flavor-Dependent Angular Analysis of $B \rightarrow K^* \ell^+ \ell^-$* , *Phys. Rev. Lett.* **118** (2017) 111801 [[1612.05014](#)].

[71] CDF collaboration, *Measurements of the Angular Distributions in the Decays $B \rightarrow K^{(*)} \mu^+ \mu^-$ at CDF*, *Phys. Rev. Lett.* **108** (2012) 081807 [[1108.0695](#)].

[72] ATLAS collaboration, *Angular analysis of $B_d^0 \rightarrow K^* \mu^+ \mu^-$ decays in pp collisions at $\sqrt{s} = 8$ TeV with the ATLAS detector*, *JHEP* **10** (2018) 047 [[1805.04000](#)].

[73] CMS collaboration, *Measurement of angular parameters from the decay $B^0 \rightarrow K^{*0} \mu^+ \mu^-$ in proton-proton collisions at $\sqrt{s} = 8$ TeV*, *Phys. Lett. B* **781** (2018) 517 [[1710.02846](#)].

[74] A. Biswas, S. Nandi, S.K. Patra and I. Ray, *New physics in $b \rightarrow s \ell \ell$ decays with complex Wilson coefficients*, *Nucl. Phys. B* **969** (2021) 115479 [[2004.14687](#)].

[75] FLAVOUR LATTICE AVERAGING GROUP (FLAG) collaboration, *FLAG Review 2024*, [2411.04268](#).

[76] PARTICLE DATA GROUP collaboration, *Review of particle physics*, *Phys. Rev. D* **110** (2024) 030001.

[77] CMS collaboration, *Measurement of the $B_s^0 \rightarrow \mu^+ \mu^-$ decay properties and search for the $B^0 \rightarrow \mu^+ \mu^-$ decay in proton-proton collisions at $\sqrt{s} = 13$ TeV*, *Phys. Lett. B* **842** (2023) 137955 [[2212.10311](#)].

[78] LHCb collaboration, *Analysis of Neutral B-Meson Decays into Two Muons*, *Phys. Rev. Lett.* **128** (2022) 041801 [[2108.09284](#)].

[79] M. Beneke, C. Bobeth and R. Szafron, *Power-enhanced leading-logarithmic QED corrections to $B_q \rightarrow \mu^+ \mu^-$* , *JHEP* **10** (2019) 232 [[1908.07011](#)].

[80] G. D'Ambrosio, G. Isidori and J. Portoles, *Can we extract short distance information from $B(K(L) \rightarrow mu+ mu-)$?*, *Phys. Lett. B* **423** (1998) 385 [[hep-ph/9708326](#)].

[81] G. Isidori and R. Unterdorfer, *On the short distance constraints from $K(L, S) \rightarrow mu+ mu-$* , *JHEP* **01** (2004) 009 [[hep-ph/0311084](#)].

[82] A.J. Buras, F. De Fazio, J. Girrbach, R. Knegjens and M. Nagai, *The Anatomy of Neutral Scalars with FCNCs in the Flavour Precision Era*, *JHEP* **06** (2013) 111 [[1303.3723](#)].

[83] BELLE-II collaboration, *Evidence for $B \rightarrow K + \nu \nu^-$ decays*, *Phys. Rev. D* **109** (2024) 112006 [[2311.14647](#)].

[84] D. Bećirević, G. Piazza and O. Sumensari, *Revisiting $B \rightarrow K^{(*)} \nu \bar{\nu}$ decays in the Standard Model and beyond*, *Eur. Phys. J. C* **83** (2023) 252 [[2301.06990](#)].

[85] BABAR collaboration, *Search for $B \rightarrow K^{(*)} \nu \bar{\nu}$ and invisible quarkonium decays*, *Phys. Rev. D* **87** (2013) 112005 [[1303.7465](#)].

[86] BELLE collaboration, *Search for $B \rightarrow h \nu \bar{\nu}$ decays with semileptonic tagging at Belle*, *Phys. Rev. D* **96** (2017) 091101 [[1702.03224](#)].

[87] A.J. Buras, J. Harz and M.A. Mojahed, *Disentangling new physics in $K \rightarrow \pi \nu \bar{\nu}$ and $B \rightarrow K (K^*) \nu \bar{\nu}$ observables*, *JHEP* **10** (2024) 087 [[2405.06742](#)].

[88] NA62 collaboration, *Measurement of the very rare $K^+ \rightarrow \pi^+ \nu \bar{\nu}$ decay*, *JHEP* **06** (2021) 093 [[2103.15389](#)].

[89] F.-Z. Chen, Q. Wen and F. Xu, *Correlating $B \rightarrow K^{(*)} \nu \bar{\nu}$ and flavor anomalies in SMEFT*, *Eur. Phys. J. C* **84** (2024) 1012 [[2401.11552](#)].

[90] (HPQCD COLLABORATION)§, HPQCD collaboration, *$B \rightarrow K$ and $D \rightarrow K$ form factors from fully relativistic lattice QCD*, *Phys. Rev. D* **107** (2023) 014510 [[2207.12468](#)].

[91] J.A. Bailey et al., *$B \rightarrow Kl^+ l^-$ Decay Form Factors from Three-Flavor Lattice QCD*, *Phys. Rev. D* **93** (2016) 025026 [[1509.06235](#)].

[92] T. Li, X.-D. Ma and M.A. Schmidt, *Implication of $K \rightarrow \pi \nu \bar{\nu}$ for generic neutrino interactions in effective field theories*, *Phys. Rev. D* **101** (2020) 055019 [[1912.10433](#)].

[93] Y. Sakaki, M. Tanaka, A. Tayduganov and R. Watanabe, *Testing leptoquark models in $\bar{B} \rightarrow D^{(*)} \tau \bar{\nu}$* , *Phys. Rev. D* **88** (2013) 094012 [[1309.0301](#)].

[94] A. Biswas, L. Mukherjee, S. Nandi and S.K. Patra, *Constraining new physics with possible dark matter signatures from a global CKM fit*, *Phys. Rev. D* **107** (2023) 055041 [[2111.01176](#)].

[95] L. Kolay and S. Nandi, *Exploring constraints on Simplified Dark Matter model through flavour and electroweak observables*, *JHEP* **10** (2024) 008 [[2403.20303](#)].

[96] L. Kolay and S. Nandi, *Flavour and Electroweak Precision Constraints on a Simplified Dark Matter Model with a Light Spin-0 Mediator*, [2503.15609](#).

[97] BELLE-II collaboration, *Test of lepton flavor universality with measurements of $R(D^+)$ and $R(D^{*+})$ using semileptonic B tagging at the Belle II experiment*, [2504.11220](#).

[98] ATLAS collaboration, *Measurement of t -channel production of single top quarks and antiquarks in pp collisions at 13 TeV using the full ATLAS Run 2 data sample*, *JHEP* **05** (2024) 305 [[2403.02126](#)].

[99] ATLAS collaboration, *Measurement of single top-quark production in association with a W boson in pp collisions at $s=13$ TeV with the ATLAS detector*, *Phys. Rev. D* **110** (2024) 072010 [[2407.15594](#)].

[100] ATLAS collaboration, *Measurement of t -channel single-top-quark production in pp collisions at $s=5.02$ TeV with the ATLAS detector*, *Phys. Lett. B* **854** (2024) 138726 [[2310.01518](#)].

[101] CMS, ATLAS collaboration, *Combination of the W boson polarization measurements in top quark decays using ATLAS and CMS data at $\sqrt{s} = 8$ TeV*, *JHEP* **08** (2020) 051 [[2005.03799](#)].

[102] M.E. Peskin and T. Takeuchi, *Estimation of oblique electroweak corrections*, *Phys. Rev. D* **46** (1992) 381.

[103] M.E. Peskin and T. Takeuchi, *A New constraint on a strongly interacting Higgs sector*, *Phys. Rev. Lett.* **65** (1990) 964.

[104] I. Maksymyk, C.P. Burgess and D. London, *Beyond S , T and U* , *Phys. Rev. D* **50** (1994) 529 [[hep-ph/9306267](#)].

[105] GFITTER GROUP collaboration, *The global electroweak fit at NNLO and prospects for the LHC and ILC*, *Eur. Phys. J. C* **74** (2014) 3046 [[1407.3792](#)].

[106] P. Asadi, C. Cesarotti, K. Fraser, S. Homiller and A. Parikh, *Oblique lessons from the W -mass measurement at CDF II*, *Phys. Rev. D* **108** (2023) 055026 [[2204.05283](#)].

[107] E. Bagnaschi, J. Ellis, M. Madigan, K. Mimasu, V. Sanz and T. You, *SMEFT analysis of m_W* , *JHEP* **08** (2022) 308 [[2204.05260](#)].

[108] ALEPH, DELPHI, L3, OPAL, LEP ELECTROWEAK collaboration, *Electroweak Measurements in Electron-Positron Collisions at W -Boson-Pair Energies at LEP*, *Phys. Rept.* **532** (2013) 119 [[1302.3415](#)].

[109] J. Altmann et al., *ECFA Higgs, electroweak, and top Factory Study*, vol. 5/2025 of *CERN Yellow Reports: Monographs* (6, 2025), [10.23731/CYRM-2025-005](#), [[2506.15390](#)].

[110] A. Soni, A.K. Alok, A. Giri, R. Mohanta and S. Nandi, *SM with four generations: Selected implications for rare B and K decays*, *Phys. Rev. D* **82** (2010) 033009 [[1002.0595](#)].

[111] J. Bernabeu, A. Pich and A. Santamaria, *Top quark mass from radiative corrections to the $Z \rightarrow b$ anti- b decay*, *Nucl. Phys. B* **363** (1991) 326.

[112] ALEPH, DELPHI, L3, OPAL, SLD, LEP ELECTROWEAK WORKING GROUP, SLD ELECTROWEAK GROUP, SLD HEAVY FLAVOUR GROUP collaboration, *Precision electroweak measurements on the Z resonance*, *Phys. Rept.* **427** (2006) 257 [[hep-ex/0509008](#)].

[113] P. Janot and S. Jadach, *Improved Bhabha cross section at LEP and the number of light neutrino species*, *Phys. Lett. B* **803** (2020) 135319 [[1912.02067](#)].

[114] D. d'Enterria and C. Yan, *Revised QCD effects on the $Z \rightarrow b\bar{b}$ forward-backward asymmetry*, [2011.00530](#).

[115] SLD collaboration, *First direct measurement of the parity violating coupling of the $Z0$ to the s quark*, *Phys. Rev. Lett.* **85** (2000) 5059 [[hep-ex/0006019](#)].

[116] ATLAS collaboration, *A detailed map of Higgs boson interactions by the ATLAS experiment ten years after the discovery*, *Nature* **607** (2022) 52 [[2207.00092](#)].

[117] ATLAS collaboration, *Evidence of off-shell Higgs boson production from ZZ leptonic decay channels and constraints on its total width with the ATLAS detector*, *Phys. Lett. B* **846** (2023) 138223 [[2304.01532](#)].

[118] CMS collaboration, *Measurement of the Higgs boson width and evidence of its off-shell contributions to ZZ production*, *Nature Phys.* **18** (2022) 1329 [[2202.06923](#)].

[119] CMS collaboration, *Measurement of simplified template cross sections of the Higgs boson produced in association with W or Z bosons in the $H \rightarrow b\bar{b}$ decay channel in proton-proton collisions at $s=13$ TeV*, *Phys. Rev. D* **109** (2024) 092011 [[2312.07562](#)].

[120] A.V. Manohar and M.B. Wise, *Modifications to the properties of the Higgs boson*, *Phys. Lett. B* **636** (2006) 107 [[hep-ph/0601212](#)].

[121] L. Bergstrom and G. Hulth, *Induced Higgs Couplings to Neutral Bosons in e^+e^- Collisions*, *Nucl. Phys. B* **259** (1985) 137.

[122] ATLAS collaboration, *Measurement of the properties of Higgs boson production at $\sqrt{s} = 13$ TeV in the $H \rightarrow \gamma\gamma$ channel using 139 fb^{-1} of pp collision data with the ATLAS experiment*, *JHEP* **07** (2023) 088 [[2207.00348](#)].

[123] E.N. Argyres, G. Katsilieris, A.B. Lahanas, C.G. Papadopoulos and V.C. Spanos, *One loop*

corrections to three vector boson vertices in the Standard Model, *Nucl. Phys. B* **391** (1993) 23.

- [124] K. Hagiwara, R.D. Peccei, D. Zeppenfeld and K. Hikasa, *Probing the Weak Boson Sector in $e+ e- \rightarrow W+ W-$* , *Nucl. Phys. B* **282** (1987) 253.
- [125] G. Gounaris et al., *Triple gauge boson couplings*, in *AGS / RHIC Users Annual Meeting*, 1, 1996 [[hep-ph/9601233](#)].
- [126] ATLAS collaboration, *Measurement of $WW/WZ \rightarrow \ell\nu qq'$ production with the hadronically decaying boson reconstructed as one or two jets in pp collisions at $\sqrt{s} = 8$ TeV with ATLAS, and constraints on anomalous gauge couplings*, *Eur. Phys. J. C* **77** (2017) 563 [[1706.01702](#)].
- [127] ATLAS collaboration, *Measurement of the $WW + WZ$ cross section and limits on anomalous triple gauge couplings using final states with one lepton, missing transverse momentum, and two jets with the ATLAS detector at $\sqrt{s} = 7$ TeV*, *JHEP* **01** (2015) 049 [[1410.7238](#)].
- [128] ATLAS collaboration, *Measurements of $W\gamma$ and $Z\gamma$ production in pp collisions at $\sqrt{s} = 7$ TeV with the ATLAS detector at the LHC*, *Phys. Rev. D* **87** (2013) 112003 [[1302.1283](#)].
- [129] ATLAS collaboration, *Measurement of total and differential W^+W^- production cross sections in proton-proton collisions at $\sqrt{s} = 8$ TeV with the ATLAS detector and limits on anomalous triple-gauge-boson couplings*, *JHEP* **09** (2016) 029 [[1603.01702](#)].
- [130] ATLAS collaboration, *Measurement of W^+W^- production in pp collisions at $\sqrt{s} = 7$ TeV with the ATLAS detector and limits on anomalous WWZ and $WW\gamma$ couplings*, *Phys. Rev. D* **87** (2013) 112001 [[1210.2979](#)].
- [131] CMS collaboration, *Measurement of the W^+W^- cross section in pp collisions at $\sqrt{s} = 8$ TeV and limits on anomalous gauge couplings*, *Eur. Phys. J. C* **76** (2016) 401 [[1507.03268](#)].
- [132] CMS collaboration, *Measurement of the $W\gamma$ and $Z\gamma$ Inclusive Cross Sections in pp Collisions at $\sqrt{s} = 7$ TeV and Limits on Anomalous Triple Gauge Boson Couplings*, *Phys. Rev. D* **89** (2014) 092005 [[1308.6832](#)].
- [133] CMS collaboration, *Measurement of the WZ production cross section in pp collisions at $\sqrt{s} = 7$ and 8 TeV and search for anomalous triple gauge couplings at $\sqrt{s} = 8$ TeV*, *Eur. Phys. J. C* **77** (2017) 236 [[1609.05721](#)].
- [134] CMS collaboration, *Measurement of the W^+W^- Cross Section in pp Collisions at $\sqrt{s} = 7$ TeV and Limits on Anomalous $WW\gamma$ and WWZ Couplings*, *Eur. Phys. J. C* **73** (2013) 2610 [[1306.1126](#)].
- [135] J.I. Aranda, T. Cisneros-Pérez, J. Montaño, B. Quezadas-Vivian, F. Ramírez-Zavaleta and E.S. Tututi, *Revisiting the top quark chromomagnetic dipole moment in the SM*, *Eur. Phys. J. Plus* **136** (2021) 164 [[2009.05195](#)].
- [136] J. Montano-Dominguez, F. Ramírez-Zavaleta, E.S. Tututi and E. Urquiza-Trejo, *The top quark chromomagnetic dipole moment in the SM from the 4-body vertex function*, *J. Phys. G* **50** (2023) 115004 [[2110.14125](#)].
- [137] CMS collaboration, *Measurement of the top quark forward-backward production asymmetry and the anomalous chromoelectric and chromomagnetic moments in pp collisions at $\sqrt{s} = 13$ TeV*, *JHEP* **06** (2020) 146 [[1912.09540](#)].

[138] M. Frank and I. Turan, *Rare decay of the top $t \rightarrow c l$ anti- l and single top production at ILC*, *Phys. Rev. D* **74** (2006) 073014 [[hep-ph/0609069](#)].

[139] J. Bernabéu, A. Santamaría and M.B. Gavela, *CP nonconservation at the Z^0 peak*, *Phys. Rev. Lett.* **57** (1986) 1514.

[140] J.I. Aranda, G. González-Estrada, J. Montaño, F. Ramírez-Zavaleta and E.S. Tututi, *Revisiting the rare $H \rightarrow q_i q_j$ decays in the standard model*, *J. Phys. G* **47** (2020) 125001 [[2009.07166](#)].

[141] S. Balaji, *CP asymmetries in the rare top decays $t \rightarrow c\gamma$ and $t \rightarrow cg$* , *Phys. Rev. D* **102** (2020) 113010 [[2009.03315](#)].

[142] S. Balaji, M. Ramirez-Quezada and Y.-L. Zhou, *CP violation and circular polarisation in neutrino radiative decay*, *JHEP* **04** (2020) 178 [[1910.08558](#)].

[143] C. Abel et al., *Measurement of the Permanent Electric Dipole Moment of the Neutron*, *Phys. Rev. Lett.* **124** (2020) 081803 [[2001.11966](#)].

[144] A.G. Grozin, I.B. Khriplovich and A.S. Rudenko, *Electric dipole moments, from e to tau*, *Phys. Atom. Nucl.* **72** (2009) 1203 [[0811.1641](#)].

[145] B. Graner, Y. Chen, E.G. Lindahl and B.R. Heckel, *Reduced limit on the permanent electric dipole moment of ^{199}Hg* , *Phys. Rev. Lett.* **116** (2016) 161601.

[146] Y. Ema, T. Gao and M. Pospelov, *Improved Indirect Limits on Muon Electric Dipole Moment*, *Phys. Rev. Lett.* **128** (2022) 131803 [[2108.05398](#)].

[147] M. Pospelov and A. Ritz, *Electric dipole moments as probes of new physics*, *Annals Phys.* **318** (2005) 119 [[hep-ph/0504231](#)].

[148] T. Liu, Z. Zhao and H. Gao, *Experimental constraint on quark electric dipole moments*, *Phys. Rev. D* **97** (2018) 074018 [[1704.00113](#)].

[149] J. de Vries, E. Mereghetti, R.G.E. Timmermans and U. van Kolck, *The Effective Chiral Lagrangian From Dimension-Six Parity and Time-Reversal Violation*, *Annals Phys.* **338** (2013) 50 [[1212.0990](#)].

[150] H. Gisbert and J. Ruiz Vidal, *Improved bounds on heavy quark electric dipole moments*, *Phys. Rev. D* **101** (2020) 115010 [[1905.02513](#)].

[151] J. Kumar and E. Mereghetti, *Electric dipole moments in 5+3 flavor weak effective theory*, *JHEP* **09** (2024) 028 [[2404.00516](#)].

[152] M. Jung and A. Pich, *Electric Dipole Moments in Two-Higgs-Doublet Models*, *JHEP* **04** (2014) 076 [[1308.6283](#)].

[153] W. Altmannshofer, S. Gori, H.H. Patel, S. Profumo and D. Tuckler, *Electric dipole moments in a leptoquark scenario for the B-physics anomalies*, *JHEP* **05** (2020) 069 [[2002.01400](#)].

[154] T. Chupp, P. Fierlinger, M. Ramsey-Musolf and J. Singh, *Electric dipole moments of atoms, molecules, nuclei, and particles*, *Rev. Mod. Phys.* **91** (2019) 015001 [[1710.02504](#)].

[155] J. Engel, M.J. Ramsey-Musolf and U. van Kolck, *Electric Dipole Moments of Nucleons, Nuclei, and Atoms: The Standard Model and Beyond*, *Prog. Part. Nucl. Phys.* **71** (2013) 21 [[1303.2371](#)].

[156] M. Gorbahn and U. Haisch, *Searching for $t \rightarrow c(u)h$ with dipole moments*, *JHEP* **06** (2014) 033 [[1404.4873](#)].

- [157] R. Gupta, B. Yoon, T. Bhattacharya, V. Cirigliano, Y.-C. Jang and H.-W. Lin, *Flavor diagonal tensor charges of the nucleon from (2+1+1)-flavor lattice QCD*, *Phys. Rev. D* **98** (2018) 091501 [[1808.07597](#)].
- [158] E.E. Jenkins, A.V. Manohar and P. Stoffer, *Low-Energy Effective Field Theory below the Electroweak Scale: Anomalous Dimensions*, *JHEP* **01** (2018) 084 [[1711.05270](#)].
- [159] Y. Ema, T. Gao and M. Pospelov, *Improved indirect limits on charm and bottom quark EDMs*, *JHEP* **07** (2022) 106 [[2205.11532](#)].
- [160] J. Brod, Z. Polonsky and E. Stamou, *A precise electron EDM constraint on CP-odd heavy-quark Yukawas*, *JHEP* **06** (2024) 091 [[2306.12478](#)].
- [161] C. Alexandrou, S. Bacchio, M. Constantinou, J. Finkenrath, K. Hadjyiannakou, K. Jansen et al., *Nucleon axial, tensor, and scalar charges and σ -terms in lattice QCD*, *Phys. Rev. D* **102** (2020) 054517 [[1909.00485](#)].
- [162] F. Sala, *A bound on the charm chromo-EDM and its implications*, *JHEP* **03** (2014) 061 [[1312.2589](#)].
- [163] H.H. Patel, *Package-X 2.0: A Mathematica package for the analytic calculation of one-loop integrals*, *Comput. Phys. Commun.* **218** (2017) 66 [[1612.00009](#)].
- [164] R. Mertig, M. Bohm and A. Denner, *FEYN CALC: Computer algebraic calculation of Feynman amplitudes*, *Comput. Phys. Commun.* **64** (1991) 345.